NASA/TM-2006-214522

Mars Aerocapture Systems Study

Henry S. Wright
Langley Research Center, Hampton, Virginia

David Y. Oh
Jet Propulsion Laboratory, Pasadena, California

Carlos H. Westhelle
Johnson Space Center, Houston, Texas

Jody L. Fisher
National Institute of Aerospace, Hampton, Virginia

R. Eric Dyke
Swales Aerospace, Hampton, Virginia

Karl T. Edquist
Langley Research Center, Hampton, Virginia

James L. Brown
Ames Research Center, Hampton, Virginia

Hilary L. Justh
Marshall Space Flight Center, Huntsville, Alabama

Michelle M. Munk
Marshall Space Flight Center, Huntsville, Alabama

November 2006

Since its founding, NASA has been dedicated to the advancement of aeronautics and space science. The NASA Scientific and Technical Information (STI) Program Office plays a key part in helping NASA maintain this important role.

The NASA STI Program Office is operated by Langley Research Center, the lead center for NASA's scientific and technical information. The NASA STI Program Office provides access to the NASA STI Database, the largest collection of aeronautical and space science STI in the world. The Program Office is also NASA's institutional mechanism for disseminating the results of its research and development activities. These results are published by NASA in the NASA STI Report Series, which includes the following report types:

- TECHNICAL PUBLICATION. Reports of completed research or a major significant phase of research that present the results of NASA programs and include extensive data or theoretical analysis. Includes compilations of significant scientific and technical data and information deemed to be of continuing reference value. NASA counterpart of peer-reviewed formal professional papers, but having less stringent limitations on manuscript length and extent of graphic presentations.

- TECHNICAL MEMORANDUM. Scientific and technical findings that are preliminary or of specialized interest, e.g., quick release reports, working papers, and bibliographies that contain minimal annotation. Does not contain extensive analysis.

- CONTRACTOR REPORT. Scientific and technical findings by NASA-sponsored contractors and grantees.

- CONFERENCE PUBLICATION. Collected papers from scientific and technical conferences, symposia, seminars, or other meetings sponsored or co-sponsored by NASA.

- SPECIAL PUBLICATION. Scientific, technical, or historical information from NASA programs, projects, and missions, often concerned with subjects having substantial public interest.

- TECHNICAL TRANSLATION. English-language translations of foreign scientific and technical material pertinent to NASA's mission.

Specialized services that complement the STI Program Office's diverse offerings include creating custom thesauri, building customized databases, organizing and publishing research results ... even providing videos.

For more information about the NASA STI Program Office, see the following:

- Access the NASA STI Program Home Page at *http://www.sti.nasa.gov*

- E-mail your question via the Internet to help@sti.nasa.gov

- Fax your question to the NASA STI Help Desk at (301) 621-0134

- Phone the NASA STI Help Desk at (301) 621-0390

- Write to:
  NASA STI Help Desk
  NASA Center for AeroSpace Information
  7121 Standard Drive
  Hanover, MD 21076-1320

Mars Aerocapture Systems Study

Henry S. Wright
Langley Research Center, Hampton, Virginia

David Y. Oh
Jet Propulsion Laboratory, Pasadena, California

Carlos H. Westhelle
Johnson Space Center, Houston, Texas

Jody L. Fisher
National Institute of Aerospace, Hampton, Virginia

R. Eric Dyke
Swales Aerospace, Hampton, Virginia

Karl T. Edquist
Langley Research Center, Hampton, Virginia

James L. Brown
Ames Research Center, Hampton, Virginia

Hilary L. Justh
Marshall Space Flight Center, Huntsville, Alabama

Michelle M. Munk
Marshall Space Flight Center, Huntsville, Alabama

November 2006

Available from:

Contents

List of Tables

List of Figures

Abstract

A detailed study of the application of aerocapture to a large Mars robotic orbiter has been completed, to identify any technology gaps for such an implementation. Specifically, this study addressed an Opposition-class Mars Sample Return mission which returns samples to Earth a year earlier than Conjunction-class scenarios. Numerous mission architecture constraints derived from the early sample return need have been incorporated. Investigation of the mission opportunities for an early sample return has been conducted leading to only the 2013 mission opportunity as having a viable mission design solution. Use of aerocapture enables this class of mission with a total launch mass being 3 to 4 times less than that of an all-propulsive orbital insertion. The study focused on maximizing the delivered mass to Mars via aerocapture. Guidance and trajectory analyses illustrate high confidence in the ability of the HYPAS control algorithm coupled with a simple roll control thruster system to easily achieve the required 500 km circular orbit altitude with less than ±25 km of altitude uncertainty. Results of aerodynamic analyses indicate a lift to drag ratio of 0.24 is feasible with a trimmed angle of attack of 16° using a traditional 70° sphere cone forebody. Aerothermodynamic analyses indicate a fully turbulent flow field exists with the resulting high heating rates. Radiative heating analyses indicate an inconsequential heating rate so that convective heating dominates the solution. Use of various TPS solutions with the aeroshell were included with the results indicating PICA and SRAM-20 as the leading forebody TPS candidates for this class of mission. A detailed packaging assessment addressed the critical aeroshell packaging constraint leading to the conclusion that the system could be accommodated within a 4.65 m diameter aeroshell with a biconic backshell, while meeting the launch and aeropass loads. Technologies which either enhanced or enabled the mission were identified. Final rough order of magnitude costs were developed. The general conclusion of the study is that while aerocapture is a significant enabler, this mission represents the upper limit on capability due primarily to the limitations in launch vehicle capability. Modest reductions in the overall delivered mass such as what could be considered for a large orbiter would result in aerocapture enabling a new class of missions.

Introduction

Aerocapture is a low-mass strategy for achieving planetary orbit from an interplanetary trajectory. With only a single aeropass, to remove the vehicle excess energy, aerocapture provides the time savings inherent in an all-propulsive orbit insertion (but without large mass) with the low mass approach of aerobraking (but without the months long duration). Aerocapture trades the large thrusters and propellant of an all-propulsive insertion for an aeroshell and thermal protection system (TPS). As with all orbital insertion strategies, a guidance, navigation, and control (GNC) subsystem is used.

Since 2002, NASA's Science Mission Directorate (SMD) In-Space Propulsion Technology (ISPT) Program has invested in advancing Aerocapture technology with the intent of reducing the time to mission infusion, and lowering risk to the first-use customers. The ISPT Program conducts detailed studies of Aerocapture at destinations of interest, to identify any technology gaps and direct future investments to fill these gaps. Studies of missions to Titan, Neptune, and Venus have been conducted in recent years (refs. 1-3), and this study of a large Mars orbiter completes the survey of technology needs for the possible aerocapture missions of the foreseeable future.

Recent design studies for aerocapture have focused on planets where the substantial ΔV required for orbital insertion negates the use of propulsion alone. For relatively small orbiters at Mars, aerocapture does not provide a significant mass advantage. Low arrival speeds and small spacecraft result in modest oribit insertion propellant masses, on the same order as the mass of a protective aeroshell. The Mars Surveyor Program (MSP) orbiter for 2001 (now known as Odyssey), began its life with aerocapture demonstration as a project goal. For the MSP-2001 orbiter, the aerocapture element was successfully developed and completed through Phase B (Preliminary Design Review) when it was removed. The primary reasons for deleting aerocapture were the reduced programmatic risk posture for the Mars Program after the two failures of the 1999 missions (Mars Climate Orbiter and Mars Polar Lander), the perceived risk in hypersonic aeromaneuvering with the associated autonomous maneuvering for orbit circularization, and the concept that the Mars Sample Return (MSR) mission would use aerobraking for its architecture thus reducing the feed-forward technology need for the MSP-2001 orbiter.

MSR has undergone many different variations since the time of the MSP-2001 orbiter aerocapture design period. One recent mission scenario for MSR (in 2004-2005) was based on a launch in 2013. In support of that mission architecture, an assessment of the benefits of aerocapture for the sample return MSR mission component has been performed. The integrated design study include mission needs definition, mission design, vehicle and configuration definition, GNC, trajectory, aerothermodynamics, TPS, and cost. All aspects of the mission assessed are discussed in this report.

The driving requirement for the study was the "Fast-Return" (Opposition-class) mission architecture. Use of multiple launches for the MSR mission is assumed as a strategy for reducing the overall complexity and risk. The landers, with the sample acquisition and Mars Ascent Vehicles (MAV), are launched while the sample return system (this study) is launched on a separate launch vehicle. Numerous mission design constraints have been included as part of the basis for the Fast-Return option. The hallmark of the Fast-Return is that the sample is returned to Earth at least 12 months prior to what it would be with a more traditional, Conjunction return. The primary focus of this study was on the Earth Return Vehicle (ERV) element and all of the associated subsystems needed for the ERV. The ERV is the only MSR mission element to use aerocapture since once the ERV achieves orbit about Mars, it does not include any Mars surface interactions. The Earth return segment of the study also included multiple options (Venus Gravity Assist versus a Deep-Space Maneuver). Due to the fluidity of the MSR mission period, the study also included an assessment of later mission opportunities to identify candidate mission opportunities where the Fast-Return option could be employed. A final study constraint was to consider only existing expendable launch vehicles.

Symbols and Abbreviations

AFE	Aeroassist Flight Experiment
ARA	Applied Research Associates
BC	Ballistic Coefficient

CBAero	Configuration Based Aerodynamics
CBE	Current Best Estimate
CER	Cost Estimating Relationship
CFD	Computational Fluid Dynamics
CG	Center of Gravity
D-DOR	Delta-Differential One-way Ranging
DOF	Degree of Freedom
DPLR	Data Parallel Line Relaxation code
EEV	Earth Entry Vehicle
EELV	Evolved Expendable Launch Vehicle
ERV	Earth Return Vehicle
FEM	Finite Element Model
FIAT	Fully Implicit Ablation and Thermal code
FPA	Flight Path Angle
FY	Fiscal Year
GCM	General Circulation Model
GNC	Guidance, Navigation, and Control
HL	Heat Load
HR	Heat Rate
HYPAS	Hybrid Predictor-corrector Aerocapture Scheme
ISPT	In-Space Propulsion Technology
LAURA	Langley Aerothermodynamic Upwind Relaxation Algorithm
L/D	Lift to Drag ratio
L_s	Solar Longitude
MASS	Mars Aerocapture Systems Study
MAV	Mars Ascent Vehicle
MEL	Master Equipment List
MER	Mars Exploration Rovers
MGCM	Mars General Circulation Model
MPF	Mars Pathfinder
MTGCM	Mars Thermospheric General Circulation Model
MSL	Mars Science Laboratory
MSP	Mars Surveyor Program
MSR	Mars Sample Return
N	North
NAFCOM	NASA/Air Force Cost Model
NEQAIR	Nonequilibrium Air Radiation Program
OS	Orbiting Sample
OSCAR	Orbit Sample Capture and Return System
PICA	Phenolic Impregnated Carbonaceous Ablator

POST	Program to Optimize Simulated Trajectories
RCS	Reaction Control Subsystem
S	South
SIRCA	Silicone Impregnated Reusable Ceramic Ablator
SLA	Super Light-weight Ablator
SMD	Science Mission Directorate
SOCM	Space Operations Cost Model
SOP	State of Practice
SRAM	Silicone Reinforced Ablative Material
TCM	Trajectory Correction Maneuver
TEI	Trans-Earth Injection
TES	Thermal Emission Spectrometer
TPS	Thermal Protection System
TPSSZR	Thermal Protection System Sizer
VGA	Venus Gravity Assist

C	Centigrade
C_D	Drag Coefficient
cm	centimeter
C_P	Pressure Coefficient
ΔV	Delta-Velocity
g	Acceleration due to gravity – 9.8 m/s^2
Hz	Hertz
J	Joule
kg	kilogram
km	kilometer
km/s	kilometers per second
m	meter
MJ	Mega-Joules
mm	millimeter
m/s	meters per second
u	Freestream Velocity
u_e	Velocity at edge of boundary layer
Re	Reynolds Number
Re_θ	Reynolds Number based on boundary layer momentum thickness
s	seconds
W	Watt

| α | Angle of Attack |
| μ | Freestream Atmospheric Viscosity |

μ_e	Viscosity at edge of boundary layer
ρ	Freestream Atmospheric Density
ρ_e	Density at edge of boundary layer
σ	Standard Deviation
θ	Angle, or Boundary Layer Momentum Thickness

Study Overview

Mars Aerocapture Systems Study (MASS) addressed the implementation of a Fast-Return (or Opposition) class approach for an early return of Mars surface samples. This approach considers only the elements needed for the Earth return segment of MSR. The integrated systems study included mission design assessments, aeropass environmental definitions (aerodynamics and aerothermodynamics), GNC assessments, trajectory assessments, TPS assessments, spacecraft configuration and packaging, aeroshell and structural sizing designs, and cost assessments. The study was initiated in April 2005 with the final review held in March 2006. This report provides the summary of the study efforts and conclusions.

MASS Problem Statement

The basic problem statement addressed through the MASS was to: "Assess and characterize the feasibility of using Aerocapture for Mars Orbit Insertion with an Opposition class ("Fast Return") Sample Return mission as a component of MSR, while identifying and assessing any enhancing or enabling technologies." With this problem statement are numerous mission constraints and assumptions. The basic guidance was to define what is required to rendezvous and capture the orbit sample capture and return system (OSCAR), transfer up to 2 kg of Mars surface sample in its sample container to the container within the Earth Entry Vehicle (EEV), and then return the sample to Earth. Previous studies by JPL's Team X (refs. 4, 5, and 6) indicated the all-propulsive option was not viable and that aerocapture was a likely candidate for enabling this mission architecture. Using the results from the JPL Team X studies as a "point of departure," the study team assessed the use of aerocapture using a rigid aeroshell (large ballistic coefficient) to enable return of this sample.

Aerocapture Assumptions

Assessing the feasibility of aerocapture as a component of MSR was addressed through MASS. It is noted that the results indicate that while the MSR mission concept did not fully close using an existing launch vehicle, the study results did indicate that a substantial mass savings could be realized for a Conjunction class sample return architecture as well as for any generic "large" delivered mass mission.

Aerocapture is defined as a single pass through the atmosphere of a body where aerodynamic drag is used to lower the excess vehicle energy sufficiently to allow the vehicle to then use a small propulsive maneuver (order <200 m/s) to raise the periapsis and achieve a nearly circular orbit. The typical aerocapture sequence is illustrated on Figure 1. The vehicle navigates through the drag maneuver modulating the bank angle to increase or decrease lift, and thus optimize its drag to achieve the desired atmospheric exit conditions (6 on Figure 1). After atmospheric exit, the spacecraft is extracted from the aeroshell (7 on Figure 1) prior to achieving the desired orbital altitude. When the spacecraft is at a predetermined intermediate altitude, the spacecraft performs the periapsis raise maneuver (8 on Figure 1) so there will be no subsequent aeropasses. When the spacecraft has achieved the predetermined orbital altitude, the spacecraft then executes the orbit circularization maneuver (9 on Figure 1).

Inherent in the aerocapture are a number of key assumptions. These assumptions begin with the selection of a rigid (high ballistic coefficient) aeroshell due to its heritage and analytic basis. The forebody configuration is then selected, which for MASS was a 70° sphere cone shape. Use of an active control system allows the peak structural and thermal loads to be limited and reduce the impact on the spacecraft. For MASS, the 99.87 percentile (3-σ) values were used as the thermal and structural load limitations. Use of the recently released Mars-GRAM 2005 was baselined for the study. Other assumptions included achieving a 500 km circular orbit with a single aeropass and up to two propulsive maneuvers (periapsis raise and circularization) with a maximum uncertainty of ±25 km (3-σ). The remaining assumptions were to consider near term technological solutions since the target launch date was within the next 10 years (note that future technologies which result in reduced system masses can allow this overall architecture to close).

Study Programmatics

MASS was an iterative, optimization study including the discipline areas key for entry mission assessments. JPL performed the interplanetary mission design efforts and the general spacecraft configuration definition. NASA-JSC performed the aeropass GNC design and assessment. NASA-ARC performed the baseline TPS sizing and assessments with inputs on alternative TPS materials (Silicone Reinforced Ablative Material [SRAM] and Carbon-Carbon) provided by Applied Research Associates (ARA) and Lockheed-Martin respectively. NASA-LaRC led the study, performed the aeropass trajectory analysis, defined the aeropass aerodynamic and aerothermodynamic environments, and performed the aeroshell design and configuration definition. NASA-MSFC provided the Mars atmospheric model data, performed the mission cost estimates, and provided the overall programmatic guidance including providing the funding. Systems engineering was balanced between NASA-LaRC, NASA-MSFC and JPL.

MASS included two reviews. An interim peer review was conducted in September 2005. The final findings were presented in the final review in March 2006. This report completes the MASS activity.

Summary Results

Comparison to Other Aeropass Missions

Missions which use aerodynamic drag to their benefit, include aerocapture missions as well as entry missions. Since aerocapture has not yet been demonstrated, only results from other similar studies can be made for relevance. Two comparisons between the MASS aerocapture maneuver with other aeropass maneuvers are made.

Comparing the MASS aerocapture with the demonstrated (or near-term) entry missions (as shown in Table 1), it can be seen that MASS has a significant increase in integrated heat loads than with previous or planned entries. The entry mass is anywhere from 3 (Mars Science Laboratory) to 12 (Mars Pathfinder) times greater than previous entries with the resulting increase in ballistic coefficient. This increase in mass and ballistic coefficient results in a 3x to 6x increase in peak heat rate. Coupled with the increased heat rate is the extended flight period at the high heating conditions resulting in a dramatic increase in integrated heat load. What these comparisons illustrate is that the aerodynamics and aerothermodynamics and their associated uncertainties drive the final answer. MASS flow assessments indicate a fully turbulent flowfield will exist, which due to the currently unverified computational fluid dynamics (CFD) models, requires a significant uncertainty value (50%) to be applied to the final aerothermodynamic results. The conclusion to be reached is that an integrated analysis which couples the aerodynamic, aerothermodynamic, and TPS uncertainties specifically addressing the turbulent flow conditions is

essential for the use of aerocapture or entry missions where turbulent flow conditions exist. Also shown in Table 1, is the reduction in peak deceleration for the aerocapture case due to the active control system, which reduces the impact on the primary structure. The final element of comparison between these missions is the aeroshell packing density. Aerocapture for this mission allows for an increase of aeroshell packing density because there is no supersonic deceleration parachute in the center of the aeroshell as well as the MASS vehicle is a "propellant heavy" vehicle where 50% of the entry mass is propellant which packs more efficiently than other systems.

Comparing MASS to other aerocapture studies, including the MSP-2001 orbiter is illustrated in Table 2. All of these missions exhibit the typical high heating conditions (high heat rate with high ballistic coefficients, and high heat load due to extended time at hypersonic deceleration conditions). All of these missions have comparable lift to drag (L/D) ratios (with the exception of the Neptune mission due to its mid-L/D configuration) and corridor widths, indicating that the MASS solution is typical for an aerocapture mission. A final comparison is with the payload to entry mass fraction. With an 85% payload to entry mass fraction, the MASS solution represents a practical upper performance limit regarding mass fraction.

Comparison to an All-Propulsive Option

To demonstrate the efficacy of the MASS conclusions, a comparison to an all-propulsive Mars orbit insertion was made. The basic assumption was that all of the other mission parameters were identical (e. g., arrival state and earth return strategies) with the "only" difference being the mode of achieving Mars orbit. The basic result (see Table 3) is that an all-propulsive mission architecture requires a 300% to 400% increase in the launch mass.

With both cases assuming launching to a positive C_3 of 10.3, then the largest expendable launch vehicle has a 7760 kg launch capability. The MASS total launch mass of 9096 kg can be accommodated if the system contingency is reduced from 30% to 11% (or if extensive system optimization is performed). The all-propulsive cannot meet this constraint, thus eliminating it as a viable option.

Mission Analysis

Mission Analysis includes all aspects of the interplanetary trajectory. With the mission design completed, an assessment of the arrival state was performed to ensure the delivery and delivery knowledge uncertainties could be tolerated by the aerocapture Hypersonic Predictor-corrector Aerocapture Scheme (HYPAS) algorithm. The integrated navigation and GNC results indicate traditional interplanetary navigation strategies, including two-way ranging and Doppler and Delta-Differential One-Way Ranging (D-DOR), provide adequate knowledge.

Mission Assessment

The objective of the MSR mission is to retrieve up to 2 kg of material from the surface of Mars and return it to Earth for scientific evaluation. A variety of different mission architectures have been proposed for this mission, including architectures utilizing conventional chemical rockets for propulsion in all phases of the mission ("all-propulsive" architectures), architectures utilizing chemical propulsion in combination with aerobraking, and architectures utilizing chemical propulsion in combination with aerocapture. In addition, both single and multiple launch architectures have been considered for this mission. For this study, we adopted a multiple launch mission architecture developed by the Mars Program's advanced studies group for an MSR mission launched in the 2013 timeframe. Separate

launches are conducted for three separate elements: two landers and one orbiter/ERV. Each element is launched directly to a positive C_3 Earth escape trajectory. The landers themselves incorporate multiple systems including the entry and descent and landing system, the sample collection system, and the MAV. When the landers arrive at Mars, they land using a direct entry trajectory. The landers then collect the samples and transfer them to the MAV. The MAV launches the samples into a 500 km circular Mars orbit to await retrieval by the ERV. Further details on the design of the landers and MAV are available in reference 7.

When the Orbiter/ERV arrives at Mars, it uses an aerocapture maneuver to capture into a low Mars orbit. After retrieving the orbiting sample (OS), the Orbiter/ERV's onboard propulsion system is used to escape Mars via a trans-Earth injection (TEI) maneuver. When the Orbiter/ERV arrives at Earth, the EEV containing the OS is released and returns to Earth on a direct entry trajectory.

The primary focus of this study was on the Orbiter/ERV, which is the only element of the overall mission to utilize aerocapture. Because the Orbiter/ERV and the landers are launched on separate launch vehicles, the ERV's design requirements are generally independent from those of the lander, with the exception of the OS itself and the parameters of the rendezvous orbit. In this study, the OS was treated as a passive 4.6 kg. element which is retrieved directly from a 500 km circular orbit. No other elements of the lander were designed or analyzed in this study.

Constraints

Although the landers and Orbiter/ERV are launched separately, the arrival of the landers must be coordinated with the arrival of the Orbiter/ERV to allow sufficient time to collect and launch the samples, but still allow the Orbiter/ERV to depart for Earth within its specified departure return window. The need to coordinate launch and operation of multiple elements places the following requirements on the mission design.

1. A minimum of 14 days shall pass between the nominal launch date of each element (lander or Orbiter/ERV).

2. There shall be > 45 days between the time the Orbiter/ERV arrives at Mars and time at which it departs for Earth (i.e. the stay time at Mars in a 500 km orbit must be greater than 45 days).

3. The landers shall arrive at least 75 days prior to departure of the ERV.

4. The time between arrival of each element (lander or Orbiter/ERV) at Mars shall be greater than 5 days.

5. The landers shall reside on the surface of Mars for no more than 30 days before the MAV launches the sample into Mars orbit.

6. All elements shall utilize a common TPS. As a consequence of this requirement, the Lander's entry velocity is not constrained to current Mars Science Laboratory (MSL) limits. Instead, the aerocapture TPS is utilized for landers, allowing for higher entry velocities than allowed on current programs.

7. The maximum allowable Earth return hyperbolic $V_{infinity}$ shall be 3.19 km/s. This value is consistent with the current Mars advanced programs office baseline EEV design requirements.

8. The ERV may be on-station prior to MAV launch.

9. Knowledge/control of the MAV delivery orbit node location shall be available prior to ERV orbit insertion at Mars.

10. The OS rendezvous orbit shall be a 45° inclination (±1.0°), 500 km altitude (±100 km on both periapsis and apoapsis) circular Mars orbit. MAV's targeting accuracy for the rendezvous orbit ascending node is currently undefined.

11. The Lander will enter with a flight path angle of -14.5° and shall have the ability of targeting any landing site between the latitudes of 45S and 45N.

Note that the possibility that Mars dust storms may occur during the landing and MAV launch periods is not considered in this analysis.

Investigation of the Opportunities

Although MSR requires the use of outbound (Earth to Mars) and inbound (Mars to Earth) trajectories that are phased correctly, there are a variety of different combinations of trajectories that can fulfill the mission requirements. In this study, we considered three sets of trajectory options, each with different mission durations, propulsive requirements, and limitations.

The existence of a viable set of inbound and outbound trajectories for a particular mission is a function of the phasing between Earth and Mars. The minimum energy opportunity for transferring between the Earth and Mars presents itself every 26 months. For typical type I or II (180°- 360° transfer) trajectories, transfer times will range from 7 to 13 months.

If the landers and Orbiter/ERV are launched on type I/II trajectories in one opportunity, the total mission duration for a typical "slow" MSR architecture will be ~33 to 39 months. When using type I/II trajectories for the outbound and inbound legs of the mission, the stay time at Mars (the time between Orbiter/ERV arrival and departure) is constrained by the phasing between Earth and Mars and is approximately 1 year. This leaves ample, if not excessive, amounts of stay time at Mars for a multi-month aerobraking campaign followed by OS rendezvous and departure. Aerobraking into Mars orbit is an attractive option for this architecture, as a fully propulsive Mars insertion increases the size of the Orbiter/ERV to the point where the Orbiter/ERV alone must be launched on a Delta IV-4050H-19 launch vehicle instead of an Evolved Expendable Launch Vehicle (EELV) (ref. 4). Because sufficient time is available for a three month aerobraking campaign, aerocapture is potentially mission enhancing on this architecture, but is not mission enabling. An example "slow" MSR architecture launched in 2013 is shown in Table 4. Note that the architecture shown violates the Earth entry velocity upper limit constraint of 3.19 km/s.

Because the stay time at Mars is constrained by phasing, faster MSR options require the use of different classes of trajectories. One "fast" MSR architecture that reduces the overall mission duration from 33 to 20 months uses a type I trajectory for the Earth-Mars outbound transit combined with Venus gravity assist (VGA) on the Earth return path. With a 2013 launch opportunity, the phasing of the Mars-Venus-Earth trajectory allows for a much earlier Mars departure than in the "slow" MSR architecture. Table 4 shows an example "fast" MSR architecture launched in the 2013 timeframe.

The 2013 "fast" mission meets all of the mission constraints, however, the energy required for the return is relatively high. Aerobraking is incompatible with this architecture due to the short Mars stay time (45 days). Because of the high energy required for the return trajectory, the mass of an all-propulsive mission would greatly exceed the capability of the Delta IV-4050H-19 launch vehicle. Aerocapture is considered potentially mission enabling for this architecture based on the reduction of propellant mass.

In a search for a low-energy "fast" option, a survey was conducted of all available Mars-Venus-Earth trajectories between 2014 and 2025. The 2013 opportunity was found to be the only viable "fast" mission available in this time frame. Table 5 summarizes the results of this search for "fast" options. Essentially, the departure date for the Mars-Venus-Earth trajectory always occurs near or even before the arrival of the Earth-Mars trajectory. As a result, stay times and departure C_3's at Mars are unfavorable, making the overall architecture unviable. Examples of the problems encountered with these trajectories are shown in Appendix B.

One potentially viable alternative to the "fast" architecture is the "medium" architecture shown in Table 4. This option satisfies the requirements outlined in the Constraints section. Its launch date is 2.5 years later but it offers an attractive energy trade vis-à-vis the 2013 flights. The "medium" 2016 opportunity requires a high-energy interplanetary injection, but in return for this investment the flight back from Mars is inexpensive. This trade is favorable because the booster supplies most of the required ΔV, leaving only a minimal propellant load to be carried by the ERV for the return journey. The 2016 mission duration is six months shorter than the "slow" option and saves at least 200 kg in propellant with respect to that option. The Medium option is, like the Fast option, limited in its stay-time at Mars. The stay time of 1.5 months precludes the use of aerobraking for the ERV, while an all-propulsive architecture would greatly increase the mass of the Orbiter/ERV. Aerocapture is therefore potentially enabling for the "medium" option on an EELV class launch vehicle. Selection of the Medium Option was deferred since the overall mission duration is 6 months less than for the Conjunction class mission, therefore, one of the primary mission constraints is not met.

Baseline Mission Architecture

At the request of the Mars Program's Advanced Studies Group, the 2013 "Fast" MSR mission architecture was selected as the baseline for the MASS. The Orbiter/ERV launches to an Earth departure C_3 of 10.3 km^2/s^2 and utilizes both a deep space maneuver and a VGA on the return trajectory to shorten the overall trip time. The overall trajectory is shown in Figure 2 and the mass and maneuver history is shown in Figure 3 and Figure 4. The mass and maneuver calculations are shown in Appendix C.

The Orbiter/ERV stack launches from Earth in December 2013 and travels to Mars on a type I ballistic trajectory. After using the cruise stage to conduct several trajectory correction maneuvers (TCM's), the vehicle arrives at Mars in June 2014 with a hyperbolic approach velocity of 4.7 km/s. The cruise stage separates just prior to atmospheric entry. The vehicle then executes an aerocapture maneuver to enter an elliptical orbit with a 500 km apoapsis (nominal) and low periapsis (within the atmosphere). The forebody and backshell (collectively referred to as the "Aeroshell stage") and the structural mid-truss stage are separated from the main vehicle just after the Aerocapture maneuver. A periapsis raise maneuver is then executed by the propulsion stage and the vehicle enters a 500 km circular orbit. Over the course of the next 92 days, the Orbiter/ERV stack maneuvers to rendezvous with, and capture, the OS from its holding orbit. The OS is a passive element, with no on-board maneuvering capability; all of the rendezvous maneuvers are conducted by the propulsion stage.

After acquiring the OS, a portion of the sample capture hardware is jettisoned before the vehicle begins a sequence of two apoapsis raise maneuvers and a periapsis lowering maneuver to prepare for the TEI maneuver. The propulsion stage is jettisoned after this maneuver sequence. The Orbiter/ERV provides propulsion for the final TEI maneuver, which puts the ERV on a return trajectory to Earth utilizing a VGA. Two months after the VGA, a deep space maneuver is conducted by the Orbiter/ERV to target the Earth. As the vehicle approaches Earth, a final Earth entry targeting maneuver is conducted

before the EEV separates from the ERV. The EEV directly enters the Earth's atmosphere while the ERV is deflected away from the Earth to enter its disposal orbit.

The overall ΔV requirements for the Orbiter/ERV stack are substantial, as fast return requires a high energy Mars departure and a large deep space maneuver (1200 m/s). The ΔV requirements are summarized in Table 6. Aerocapture is a critical element of this architecture because of the very high ΔV requirements imposed on the vehicle. With aerocapture, the separated mass from the launch vehicle is 9096 kg. (see Table 19). If aerocapture were removed from the architecture and an all-propulsive mission used instead, the separated mass from the launch vehicle would increase by over 20,000 kg (see Table 3 and Figure 49).

Arrival State (Arrival Navigation)

An aerocapture trajectory differs from the more traditional Mars approach trajectories in that the typical arrival velocity is high. Aerocapture benefits from maximizing arrival velocity due to the orbital type velocity at atmospheric exit (up to the heating and deceleration limits of the system), whereas just the opposite is the norm with traditional Mars arrivals (entry cases where the entire arrival velocity must be removed by the system). A higher arrival velocity limit provides increased flexibility in the mission design for an aerocapture mission.

The primary objective of approach navigation is to determine initial conditions at the atmosphere's entry interface point and to minimize the associated uncertainties. The arrival trajectory defines the nominal initial conditions for the ERV at the atmosphere entry interface point (*i.e.* start of the aerocapture flight). Significant uncertainty at the atmospheric interface point could lead to loss of the vehicle to a degraded orbit, however, the traditional navigation strategies previously demonstrated on entry missions are sufficient to meet the aerocapture delivery and knowledge requirements.

A tracking schedule of doppler and ranging data is sufficient to meet the needs of an aerocapture entry at Mars, but augmenting the tracking data with D-DOR observations will improve the spacecraft delivery such that the benefits of high accuracy (conserves propellant, leaves margin for aerodynamic and atmospheric uncertainties, and calibrates on-board inertial measurement units accurately) accrue. Four approach maneuvers are scheduled during the final two months of cruise to achieve the required precision at Mars entry. The arrival state uncertainties that are required for aerocapture are achievable with proven navigation methods, including D-DOR. The baseline entry flight path angle (FPA) is -12.731°. The navigation subsystem delivery accuracies lie between FPA = ±0.5° and ±0.3° (3σ). The higher uncertainty represents a state estimate made 3 days distant from Mars; the lower uncertainty is the entry knowledge immediately before entry. The improvement during the last 3 days is only modest because thrusting events occur during that time, and those events tend to maintain the overall entry uncertainty.

Two post-atmospheric exit maneuvers are required to circularize the orbit at 500 km (total ΔV ~200 m/s 3σ). The first maneuver, to raise the orbit out of the atmosphere, must occur ~1 hour after atmosphere exit. This maneuver can be large and perform 100% of the circularization, or it can be split into two maneuvers with a small burn one hour after atmospheric exit (ΔV ~35 m/s) for the sole purpose of raising the periapsis up to 160 km (just out of the atmosphere). The second, larger circularization ΔV is applied later without tight schedule constraints.

The rendezvous with the OS must occur as rapidly as possible because significant OS orbit dispersions result from the MAV injection uncertainties, and those dispersions grow with time. For example, the OS semi-major axis uncertainty (assuming δa = ±100 km, 3σ) yields a nodal regression rate of 7.0 ±0.7° per

day (3σ) for a 30º latitude site. The ERV needs to match orbits with the OS, so the mission needs to demonstrate that the ascending node of the ERV orbit, after aerocapture, will match the OS orbit node. Bank angle steering during aerocapture offers some flexibility and can adjust the ERV's ascending node. This strategy requires no propellant and places the ERV immediately into the target orbit with no time spent precessing nodes. Bank angle steering allows up to a ±15º ascending node adjustment capability. Node adjustment performance improves as entry velocity and L/D increase.

The MAV launches the OS shortly before the ERV arrives (no more than ~1 week). The ERV targets this orbit as it approaches Mars. After circularization (or near-circularization), the ERV determines its relative location with respect to the OS. Assuming nearly-aligned nodes, an OS-ERV rendezvous will require 3-4 weeks and approximately 100 m/s to complete.

Aerocapture Process

The aerocapture schematic is shown in Figure 1. With the arrival states well defined, the aerocapture performance analysis is performed. Mars-GRAM 2005 model was used as the atmosphere model with ancillary assessments of the aerocapture performance assessed using the Thermal Emission Spectrometer (TES) data. The basic aerocapture flight configuration is to fly a constant 16° angle of attack to maintain an L/D of 0.24 throughout. High fidelity aerodynamic and aerothermodynamic analyses provided inputs into the guidance and control simulations. The HYPAS guidance algorithm enables the vehicle to remain within the 2.4° corridor by modulating the bank angle to achieve the desired drag (maintain constant L/D so as change lift, drag is also changed). The analyses also addressed the deceleration loading as well as the thermal loading including TPS sizing.

The initial phase of aerocapture has been demonstrated on numerous guided entry missions (all of the crewed missions and the two Viking landers). The exit phase is where aerocapture has not been demonstrated as no vehicle has done this before. This is the key area of uncertainty where the guidance robustness was focused and demonstrated acceptable performance.

After exiting the atmosphere, the system waits until the predicted state is 10 minutes above the exit interface. At that time the spacecraft (Earth Return Vehicle and Propulsion Module) is extracted from the aeroshell. Approximately 40 minutes later, the propulsion module executes the periapsis raise maneuver to ensure the spacecraft does not reenter the atmosphere. At this point the spacecraft is a safe configuration in an elliptical orbit. For MASS, the assumption was made that the spacecraft would then perform the circularization maneuver as the spacecraft approached the final orbital altitude. With the final circularization being complete, the spacecraft then provides updates to Earth such that the final orbital ephemeris can be established and the next phase of the mission begun. After completing the initial periapsis raise maneuver, and prior to performing the circularization maneuver, the spacecraft could have begun the ephemeris updates with Earth such that the circularization maneuver was perfomed much later. Another alternative was to perform a single maneuver to raise the periapsis and circularize, however, that method was not considered for this study.

Modeling of the Atmosphere of Mars

Mars Global Reference Atmospheric Model (Mars-GRAM)

Mars-GRAM 2005 (references 8, 9, and 10) is an engineering-application atmospheric model for Mars. It is built around global output data sets (climatology) from the NASA Ames Mars General Circulation Model (MGCM) (ref. 11), and the University of Michigan Mars Thermospheric General

Circulation Model (MTGCM) (references 12 and 13). Two major new features of Mars-GRAM 2005 are:

1. Climatology data sets from MGCM/MTGCM model runs where the General Circulation Model (GCM) dynamics were driven by spatial and temporal variations of dust optical depth, as measured by the TES, aboard Mars Global Surveyor (ref. 14). Two Mars years of such TES-dust-driven GCM data are included, referred to as TES mapping years 1 and 2. Earlier climatology from model runs where the GCM dynamics were driven by three different, globally-uniform dust distributions (referred to as TES mapping year 0) are still included (these are the same as the GCM climatology provided with Mars-GRAM 2001).

2. An option to substitute an "auxiliary profile" of measured data in place of the conventional MGCM/MTGCM climatology values is available in MarsGRAM 2005, and was used in the MASS. TES-observed profiles of temperature, pressure, and density for mapping years 1 and 2 have been assembled into large databases that can be queried for desired locations and times, and the results (individual profiles or averages of a number of observed profiles) can be used in Mars-GRAM as "auxiliary profile" input.

Mars-GRAM Auxiliary Profiles from Observed Data

Auxiliary profiles can be generated either from TES nadir data (surface to about 40 km) or TES limb sounding data (surface to about 60 km). Table 7 provides an example auxiliary profile, generated from an average of 17 TES limb sounding profiles. Figure 5 shows a graph of the ratio of density from the auxiliary profile data in Table 7 to Mars-GRAM density from a vertical profile at the same latitude and longitude, using conventional climatology. Auxiliary profile data from Table 7 were used in Mars-GRAM to compare aerocapture results versus results obtained using Mars-GRAM with conventional MGCM climatology. Results from that comparison are presented in Appendix D. Briefly, it appears that larger density values seen in the TES observations above about 40 km give better aerocapture performance results, because the larger densities lead to better control authority for the aerocapture guidance system.

Figure 6 shows that TES-observed densities are typically larger than those simulated from conventional MGCM climatology, especially for low-to-middle latitudes, and altitudes above about 40 km. This altitude range is a typical region where periapsis would occur for rigid-aeroshell aerocature. TES observations versus climatology results in this figure have been averaged over all seasons (all L_s values) and both times of day for TES observations (2 and 14 hours local), for both TES mapping years 1 and 2.

Configuration and Aerodynamics

The following sections describe the analysis used to select the aeroshell orbiter shape and the predicted aerodynamic performance of that shape using Navier-Stokes computational flowfield solutions.

Aeroshell Configuration Basis (60° vs 70° Sphere Cone)

Aerocapture performance is influenced heavily by the L/D ratio and drag coefficient (C_D) that are generated by the ERV aeroshell. The aeroshell shape must give sufficient control authority to target the correct exit conditions, but still produce enough drag deceleration. The candidate shapes considered for Mars aerocapture were taken from past experience for atmospheric entry vehicles for Earth and Mars applications. All successful Mars landers (Viking, Mars Pathfinder, and Mars Exploration Rovers) have used a 70° sphere-cone forebody as the basis for the aeroshell. For Earth applications (Genesis, Stardust),

a 60° sphere-cone forebody has been used successfully. Both shapes produce lift primarily through axial force that is typical of blunt bodies. A brief analysis of the aerodynamic performance tradeoffs between of 60° and 70° sphere-cones was done using modified Newtonian aerodynamics, a method that gives reasonable results for hypersonic blunt bodies. Newtonian aerodynamics are based on a surface pressure distribution that is a simple function of the geometry. The pressure coefficient (C_p) is determined from the pressure ratio across a shock and the angle between the freestream velocity vector and the body surface:

$$C_p = C_{p,max}\, sin^2\theta \tag{1}$$

The term $C_{p,max}$ is the pressure coefficient behind a normal shock and θ is the angle between the freestream velocity and surface normal vectors. The aerodynamics resulting from this pressure distribution are reasonably accurate for blunt bodies at hypersonic speeds.

Figure 7 shows the L/D and C_D for 60° and 70° sphere-cones. Also shown is the performance of the Viking and MSL entry vehicles. The results show that the 70° sphere-cone gives higher L/D and C_D than does a 60° sphere-cone for the same angle-of-attack. The modified Newtonian 70° sphere-cone results also compare well to the Viking and MSL data. Based on the higher L/D, the 70° sphere-cone was chosen as the forebody shape for the MASS. A target L/D of 0.24 at a trim angle of 16° is possible with the 70° sphere-cone, and has been shown to give the desired aerocapture performance. Detailed computational fluid dynamic flowfield solutions were obtained on the selected shape at this attitude and used for aerocapture trajectory simulations.

Aerodynamics

Detailed Navier-Stokes flowfield solutions were obtained for the 70° sphere-cone geometry to confirm the preliminary analysis and provide aerodynamic coefficients for aerocapture trajectory simulations. The Langley Aerothermodynamic Upwind Relaxation Algorithm (LAURA) CFD code was used to obtain flowfield solutions at Mars flight conditions.   LAURA has been used in the past to define the aerodynamic characteristics of the Mars Pathfinder (MPF) and Mars Exploration Rover (MER) entry vehicles, which both had a 70° sphere-cone forebody. Finite-rate chemistry and thermal non-equilibrium are modeled in LAURA using an 8-species gas model to account for the high-temperature effects of hypersonic flight. Two LAURA solutions were run on each of two bounding aerocapture trajectories: lift-up, L/D=0.24, ballistic coefficient (BC)=300 kg/m^2 and lift-down, L/D=0.2, BC=200 kg/m^2. The solutions were obtained for a 4.65 m diameter aeroshell at a trim angle-of-attack of 16°. Figure 8 shows the trajectories and CFD solution points for the range of BC's considered.

Symmetry plane Mach number contours are shown in Figure 9 for the peak heating point along the Lift-Up, L/D=0.24, BC=300 kg/m^2 trajectory. The freestream Mach number is approximately 25, so the shock standoff distance is small compared to the aeroshell diameter. The Navier-Stokes equations were modeled in LAURA, but the viscous contributions to aerodynamics are small for hypersonic Mach numbers; pressure is the dominant aerodynamic force. Consequently, the aerodynamics are approximated very well with Newtonian methods.

Figure 10 and Figure 11 show that the aerodynamics are essentially independent of velocity and trajectory. For a trim α of 16°, C_D and L/D are about 1.45 and 0.25 respectively for both trajectories. Newtonian aerodynamics resulted in C_D=1.46 and L/D=0.24.   The C_D and L/D from the lift-up, (L/D=0.24, BC=300 kg/m^2) trajectory were used for aerocapture trajectory simulations with the HYPAS guidance algorithm. Figure 12 shows the line along which the center of gravity (CG) must be located for

a trim α of 16°. The needed angle of attack is achieved through an offset in the radial CG. The design CG is; axial $X_{cg}/D=0.305$ and radial $Z_{cg}/D=-0.0223$ (10.4 cm).

Guidance and Integrated Trajectory Performance

HYPAS Guidance

The HYPAS guidance algorithm was used to provide autonomous guidance for the vehicle in the simulations. The scheme was originally developed at the Johnson Space Center for the Aeroassist Flight Experiment (AFE) program (ref. 15) and its derivation was published in reference 16. During the AFE program, the algorithm was tested, compared, and evaluated against other guidance algorithms in three degree of freedom (3-DOF) and six degree-of-freedom (6-DOF) simulations, and selected for the AFE flight, prior to program cancellation.

Since the initial development, the algorithm has been actively maintained and further refined. It has been used in numerous human and robotic exploration mission studies performed by JSC and LaRC over the last 15 years. These studies involved developing nominal and dispersed trajectory simulation results for aerocapture at Earth, Mars, Titan (ref. 17), Neptune (ref. 18), and Venus (ref. 19), for a wide range of vehicle L/D, BC's, entry conditions, and target orbits. The algorithm was tested in computer-based simulation environments at JSC and LaRC and found to perform well under nominal and dispersed conditions for the wide range of conditions.

The HYPAS algorithm guides a lifting vehicle through the atmosphere to a desired exit apoapsis altitude and inclination or orbital-plane using only bank-angle as the control. The guidance is an analytic predictor-corrector algorithm based on deceleration due to drag and altitude-rate error feedback. Inputs to the algorithm are the current position, velocity, sensed acceleration, and body attitude. The algorithm outputs the commanded bank angle. It is adaptable to a wide range of initial state vectors, vehicle L/D ratios, BCs, planetary atmospheres, and desired target conditions.

The HYPAS algorithm is divided into two flight phases: the equilibrium glide, and exit phase. In the equilibrium glide phase, the vehicle computes the required bank angle to stabilize the trajectory and drive the vehicle towards conditions where all forces (aerodynamic, gravity, and centripetal) are balanced. In the exit phase, triggered when the vehicle decelerates to a specified velocity, the algorithm computes an estimate of the atmospheric exit state velocity vector. Bank angle commands are generated to follow an altitude rate profile which is corrected every computation cycle to achieve the desired analytically computed exit condition.

Bank reversals are performed throughout the flight in order to minimize the error in inclination and/or node. The lateral logic generates a deadband in wedge angle, or inclination, as a function of inertial velocity. Whenever the vehicle exceeds this lateral error, a bank reversal is commanded. The direction of the bank reversal is selected as a function of flight phase, and angular distance from the current desired bank angle.

In this study, two vehicle configurations were investigated, a nominal 300 kg/m^2 BC case, and a 200 kg/m^2 BC case. The 300 kg/m^2 BC case represents the maximum mass capability provided by the Delta IV-4050H-19 launch vehicle with a 4.65 m diameter aeroshell. The HYPAS algorithm was tuned in each case to minimize the final post-aerocapture circularization ΔV. Additionally, after mass estimates were updated, a 365 kg/m^2 BC case was investigated. The HYPAS algorithm was not re-tuned from the

nominal 300 kg/m^2 case to test the robustness of the guidance. The basic results showed acceptable performance of the 365 kg/m^2 case.

POST2 Trajectory Simulation

The trajectory program used to simulate the guided aerocapture maneuver at Mars was Program to Optimize Simulated Trajectories-II (POST2) (ref. 20). POST2 is a generalized point mass, discrete parameter targeting and optimization trajectory program. It has the ability to simulate 3DOF, 6DOF and multiple degree-of-freedom (multi-DOF) trajectories for multiple vehicles in various flight regimes (i.e. entry, launch, rendezvous, and intercept trajectories). POST2 also has the capability to include different atmosphere, aerodynamics, gravity, propulsion, parachute and navigation system models. Many of these models have been used to simulate the entry trajectories for previous NASA missions (i.e., MER, Genesis, MPF), as well as current and planned NASA missions (i.e. Stardust, Phoenix, and MSL).

The total MASS flight simulation is comprised of three main components: the 3DOF POST2 trajectory simulation, a Monte Carlo simulation which parallel process' up to 64 simulations, and supporting scripts for compiling and data analysis. The 3DOF POST2 aerocapture simulation includes vehicle geometric parameters, aerodynamic tables, Mars's gravity and atmosphere models, HYPAS guidance algorithm and initial states all integrated with the equations of motion to produce the nominal aerocapture trajectory. A Monte Carlo analysis was also conducted to tune the guidance and to measure the performance, risk and robustness of the Mars aerocapture. Exactly 2000 individual POST2 aerocapture trajectories were simulated with random perturbations applied to the entry FPA, vehicle aerodynamics, vehicle mass and Mars atmospheric conditions.

Simulation Results and Performance

The nominal HYPAS guidance profile, in bank angle, drag deceleration, altitude rate, and wedge angle error can be seen in Figure 13. This profile results in a final apoapsis altitude of 502.9 km, a periapsis altitude of -14.3 km, and a peak deceleration load of 4.0 g's. Once the guidance was tuned, Monte Carlo simulations (2000 cases) were performed to assess estimated errors in initial conditions, aerodynamics, atmosphere, and mass properties (see Table 8). The Monte Carlo trajectory simulation results can be seen in Figure 14 through Figure 19, and a summary can be seen in Table 9.

The Monte Carlo uncertainties for the nominal 300 kg/m^2 case are presented in Table 8 and include estimated errors in FPA, aerodynamic coefficients, Mars atmosphere, and vehicle mass. The nominal FPA of -12.731° was determined from the middle of the 2.349° corridor width (-13.905° to -11.556°) of the full lift up and full lift down trajectories for the 300 kg/m^2 nominal case. A uniform dust tau variation was also used along with a random number seed perturbation of atmospheric density in Mars-GRAM.

The results from the 2000 case Monte Carlo analysis are presented in Figure 14 through Figure 19. Figure 14 shows the final apoapsis altitude versus the periapsis altitude at atmospheric exit, before a circularization maneuver is performed. The resulting dispersion in apoapsis altitude is 504.5 km ± 26.4 km (3σ). Figure 15 shows the ΔV required for orbit circularization after aerocapture. The circularization ΔV dispersion is 122.8 m/s ± 10.2 m/s (3σ). The peak laminar heat rate and integrated heat load indicator are shown in Figure 16. The resulting dispersion in laminar peak heat rate is 120.7 W/cm^2 ± 11.4 W/cm^2 (3σ), and the laminar peak heat load dispersion is 12023.5 J/cm^2 ± 1091.7 J/cm^2 (3σ). Figure 17 presents the maximum loading, or deceleration, on the vehicle. The peak deceleration dispersion is 4.3 g's ± 0.9 g's (3σ).

A turbulent heating rate estimate, specific to MASS, was generated from LAURA and implemented into POST2. Figure 18 and Figure 19 show the peak turbulent integrated heat load and heating rate respectively calculated in POST2. The peak turbulent heat load dispersion is 19003 J/cm^2 ± 1788 J/cm^2 (3σ). The dispersion in peak turbulent heating rate is 275.5 W/cm^2 ± 45.3 W/cm^2 (3σ). The basis of the turbulent heating is discussed in the Forebody Heating Environments section.

Similarly, the 200 kg/m^2 BC case was tuned to minimize the post aerocapture ΔV. The nominal profile achieved a 504.0 km apoapsis altitude, and 4.6 km Periapsis altitude, with a peak 4.0 g deceleration load, as can be seen in Figure 20. Monte Carlo simulation dispersion can be seen in Table 11, and Figure 21 through Figure 26.

The Monte Carlo uncertainties for the 200 kg/m^2 case, are presented in Table 10 and include estimated errors in FPA, aerodynamic coefficients, Mars atmosphere, and vehicle mass. The nominal flight path angle of -12.497° was determined from the middle of the 2.317° aeropass corridor width (-13.655° to -11.338°) of the full lift up and full lift down trajectories for the 200 kg/m^2 nominal case. A uniform dust tau variation was also used along with a random number seed perturbation of atmospheric density in Mars-GRAM. Also the nominal vehicle mass is smaller than the 300 kg/m^2 case at 4900 kg with the same dispersions.

The results from the 2000 case Monte Carlo analysis for the 200 kg/m^2 ballistic coefficient are presented in Figure 21 through Figure 26. Figure 21 shows the final apoapsis altitude versus the periapsis altitude at atmospheric exit, before a circularization maneuver is performed. The resulting dispersion in apoapsis altitude is 510.5 km ± 14.4 km (3σ). It should be noted that the standard deviation is 4.4 km smaller than the nominal case. Figure 22 shows the ΔV required for orbit circularization after aerocapture. The circularization ΔV dispersion is 117.7 m/s ± 6.3 m/s (3σ). The peak laminar heat rate and integrated heat load indicator are shown in Figure 24. The resulting dispersion in laminar peak heat rate is 99.2 W/cm^2 ± 9.6 W/cm^2 (3σ), and the laminar peak heat load dispersion is 9947.6 J/cm^2 ± 978.6 J/cm^2 (3σ). Figure 23 presents the maximum loading, or deceleration, on the vehicle. The resulting peak deceleration dispersion is 4.3 g's ± 1.2 g's (3σ).

The LAURA turbulent heating rate estimate, implemented into POST2, produced the results for the 200 kg/m^2 BC case shown in Figure 25 and Figure 26; peak turbulent integrated heat load and heating rate respectively. The peak turbulent heat load dispersion is 13674.5 J/cm^2 ± 1306.8 J/cm^2 (3σ). The resulting dispersion in peak turbulent heating rate is 198.8 W/cm^2 ± 33.6 W/cm^2 (3σ). It can be seen that the 200 kg/m^2 case trajectories produced lower peak turbulent heating rates and a lower standard deviation compared to the nominal case. Also, the integrated turbulent heat load standard deviation was lower than the nominal case by approximately 160 J/cm^2. This reduction is due to the reduced BC.

Aeroheating Environment

The heating environments (peak heat flux and total integrated heat load) are based on convective heating only. Radiative heating is typically small for Mars entries because no strong radiators appear in the chemical makeup of the dissociated Mars gases. Forebody heating environments were based on Navier-Stokes CFD flowfield solutions using LAURA. The afterbody environments were generated by scaling the forebody heating time-history. The likelihood of turbulent transition was assessed and accounted for in the heating environments.

Forebody Heating Environments

The magnitude of the heating environments depends largely on whether turbulent transition is expected to occur before the time of peak heating. There is no generic method to predict turbulent transition for 70° sphere-cone geometries. In the case of MSL, a momentum-thickness Reynolds number (Re_θ) criterion of 200 has been established as the transition indicator, where Re_θ is defined at the edge of the boundary layer:

$$Re_\theta = \frac{\rho_e u_e \theta}{\mu_e} \qquad (2)$$

$$\theta = \int_0^\infty \frac{\rho u}{\rho_e u_e}\left(1 - \frac{u}{u_e}\right)d\eta \qquad (3)$$

If Re_θ exceeds 200 using a laminar CFD solution, then the CFD is re-run with turbulence turned on. The freestream conditions were taken from the guided, L/D=0.24, BC=300 kg/m² trajectory that resulted in the 3-σ high stagnation point heat flux. Figure 28 shows the Re_θ distribution on the forebody at the time of peak stagnation point heat flux. The LAURA results indicate that Re_θ exceeds 200 on the forebody. Consequently, the LAURA solution was re-run using the Baldwin-Lomax algebraic turbulence model turned on. A user-defined transition location was specified to give a fully turbulent solution. Figure 27 shows a comparison of the laminar and fully turbulent heat flux along the middle of the forebody. Turbulence increases heat flux by a factor of 2.5 over the laminar value (not including uncertainties). A 50% uncertainty was added to the LAURA turbulent heat flux for the TPS sizing analysis. The 50% uncertainty is larger than the laminar uncertainty typically used for past Mars entry vehicles (Pathfinder, MER). A larger uncertainty is warranted given the relative difficulty of predicting a turbulent flowfield, as well as TPS material response effects in a turbulent environment (roughness, blockage, etc.).

Figure 29 shows the turbulent heat pulse for guided, L/D=0.24, BC=300 kg/m² trajectories. A 50% uncertainty has been added to account for unknowns in the computational methods, especially in the presence of turbulent conditions. Results are shown for the 3-σ high (99.87%) heat rate (HR) and 3-σ high (99.87%) heat load (HL) trajectories. These design trajectories were obtained through a Monte-Carlo analysis of the aerocapture system, which includes uncertainties in navigation, atmosphere, and aerodynamics. The maximum heat rate determines selection of the TPS material and total integrated heat load determines the material thickness. Including uncertainty, peak heat rate is about 372 W/cm² and maximum total heat load is 24200 J/cm². These heating levels are well in excess of past Mars lander aeroshells. For example, Mars Pathfinder experienced a peak heat rate near 106 W/cm² for a 7.6 km/sec direct entry and a BC of 62 kg/m².

Afterbody Heating Environments

The afterbody heating environments were estimated using the results of the forebody analysis: CFD solutions were not obtained for the wake flowfield. It is generally known that, for blunt bodies such as a 70° sphere-cone, the afterbody heat rate is a small percentage of the forebody level. For this analysis, the maximum afterbody heat rate was estimated to be 5% of the maximum forebody laminar heat rate. The afterbody heat pulse was shaped using the forebody heat pulse. A 200% environments uncertainty was included for TPS material sizing. A large uncertainty was used since no CFD analysis was done for the

afterbody flowfield. Using this method, peak heat rate is about 15 W/cm^2 and maximum total heat load is 1500 J/cm^2, including uncertainties (Figure 30). The environments are shown for the same design trajectories that were used to define the forebody environments. The TPS material selection and sizing were based on the forebody and afterbody environments shown in Figure 29 and Figure 30.

Radiative Heating

A cursory radiative heating analysis was performed for MASS, using the Tauber-Sutton relationship (ref. 21), for the 3σ low trajectory with the 1.163 m nose radius. The peak radiative heat rate was found to be 29 W/cm^2 (see Figure 31). This heat rate is about 8% of the peak turbulent convective heat rate, consequently, no further analysis was performed and radiative heating was neglected for the integrated heating analysis.

Thermal Protection System

The primary purpose of the TPS is to protect the vehicle from the high heating and oxidizing environment experienced during atmospheric entry. The several steps in the TPS design process include:

1. Determination and review of the heating environment,

2. Determination of the TPS system substructure

3. Specification of TPS materials suitable for the anticipated heating environment, and

4. Specification of TPS thickness based on analysis by a TPS material response code.

TPS design is affected by the unique requirements of the present Mars aerocapture mission concept. Relative to prior Mars missions, the present mission concept involves a larger diameter vehicle (4.65 m dia) with the Mars atmospheric entry intended for aerocapture rather than descent to the surface. The larger diameter vehicle results in high heating levels associated with predominantly turbulent flow over the heatshield, while the aerocapture maneuver is of extended time duration leading to a long soak time of the thermal protection materials in the high heating environment. The net result is that the aerothermal heating environment that this vehicle would experience during the aerocapture maneuver is particularly harsh. Additionally, behind the hypersonic bow shock the relatively chemically inert CO_2 of the Martian atmosphere undergoes dissociation into a chemically active, highly oxidizing mixture of CO, O and other constituents. Such an environment promotes surface oxidation and recession of an ablative TPS material. As a consequence, the TPS design requirement likely leads to a choice of materials capable of handling higher heating than previous Mars missions and may lead to higher TPS system mass fractions than previous Mars mission designs would suggest.

Due to limitations in resources available for this study, TPS sizing was based on a subset of the full procedure used for full mission design. Only one spatial location for a constant thickness forebody heatshield and one spatial location for the constant thickness aftbody were considered. A typical fully supported mission design would provide a heatshield, fore and aft, of varying thickness which would typically be of reduced mass relative to the single point design of the present study. Further, multiple trajectories would be considered in the full mission design process to ensure the correct thickness was specified over the surface of the heatshield.

The particular trajectory heating curve used for the TPS design process for the MASS was the 99.87% HR trajectory as shown in Figure 29 and Figure 32. This heating curve, which incorporates a 50% heat rate uncertainty, gives a peak heat rate of 372 W/cm^2, and an integrated heat load of 23,200 Joules/cm^2

prior to heatshield ejection at t=867 seconds (t=0s at atmospheric entry). Although the 99.87% HL trajectory gives a slightly higher integrated heat load (24,000 J/cm^2), preliminary analysis demonstrated that the 99.87% HR trajectory was the worst-case TPS sizing heating environment provided.

To first approximation, the peak heat rate trajectory (undershoot) determines the TPS material, while the peak integrated heat load trajectory (overshoot) determines TPS sizing. However, as in this instance, the earlier high heating pulse seen in the 99.87% HR heating curve of Figure 32 results in a longer soak time and resultant thicker TPS sizing with the peak heat rate trajectory, even though the peak integrated heat load trajectory of 99.87% HL does have a slightly (by 4%) higher integrated heat load.

Prior Mars missions have used Super Lightweight Ablator (SLA)-561V TPS material for their heatshield. At present, this material is limited to 290 W/cm^2 or less. Other materials considered and rejected based on preliminary analysis for use as a baseline TPS are shown in Table 12. After sufficient review, phenolic impregnated carbonaceous ablator (PICA) was chosen for the forebody heatshield and SLA-561V was chosen for the aftbody TPS.

For the purposes of thermal response analysis of the TPS heatshield, it is assumed that the substructure upon which the TPS is mounted consists of 2.8 mm thick carbon fiber sheet mounted to 25.4 mm thick Aluminum honeycomb which is then mounted upon a 2.8 mm thick carbon fiber sheet. The interface of the TPS material with the first carbon sheet is the bondline for which the temperature must be maintained below 250° C to protect the adhesives used. The 25.4 mm thick aluminum honeycomb and carbon face sheets are included in the TPS system thermal response modeling.

The Fully Implicit Ablation and Thermal (FIAT) material response code described in references 22 and 23 provided the thermal response analysis used to determine the TPS thickness. A primary objective of this thermal analysis is to ensure that the bondline temperature during the aerocapture maneuver does not exceed 250° C prior to heatshield ejection. The FIAT code has seen extensive use for TPS sizing with the recent Stardust and MER missions, as well as being central to the Exploration Systems Architecture Study/Crew Exploration Vehicle studies. FIAT accomplishes 1D transient modeling of heat and mass transfer within the depth of the TPS material as it responds in time to input boundary layer convective heating and gas phase radiative heating (no radiative heating used in the MASS) to the heatshield surface. Included in the FIAT TPS modeling is the pyrolysis, or decomposition, of the TPS material at depth within the heatshield. Heat transfer (uncorrected for blowing) to the surface as a function of time for the particular trajectory being simulated must be provided as an input. The convective heating is typically provided by a real-gas Navier-Stokes solution such as from either Data Parallel Line Relaxation (DPLR) code or LAURA (used in the MASS). Alternatively, the gas-phase radiation and convective heating can be derived based either engineering codes such as configuration based aerodynamics (CBAero; see reference 27) or from empirical heat transfer relations, such as Marvin-Diewart (reference 30), Tauber-Sutton (reference 21) or from a CFD based curve-fit such as given by Loomis (reference 31).

$$p,q,\tau \sim C\rho_\infty^m V_\infty^n \qquad (4)$$

The specified convective heating is obtained without the effect of gas blowing associated with ablation. Consequently, FIAT itself makes use of an engineering relation to account for the reduction in heat transfer convection coefficient with boundary layer surface mass blowing. Within an ablative TPS material, conduction heat transfer from the surface to the heatshield interior then occurs through the insulating char layer to the pyrolysis zone, where the TPS undergoes thermal decomposition, absorbing energy while producing pyrolysis gases and ablation products. These gases then migrate through the

porous char layer back to the surface where they produce a boundary layer blowing effect to reduce the convective heat transfer coefficient. While heating of the char layer and energy spent in accomplishing the pyrolysis reaction accounts for a significant portion of the thermal energy entering the TPS at the surface, conduction to the virgin TPS material located interior to the pyrolysis zone results in a gradual increase in temperature at the bondline. This increase in TPS bondline temperature is mitigated in part by the substantial thermal mass associated with the substructure to which the TPS is mounted. However, as stated previously, one measure of the effectiveness of the TPS heatshield is to maintain the bondline temperature below 250° C during the aerocapture maneuver until the heatshield ejection.

To accomplish the FIAT analysis, the TPS material response properties are required. For many such TPS materials, either historically used or proposed for future missions, properties may be found in the TPSX database (see reference 24 or http://www.tpsx.nasa.gov). The properties of many TPS materials are, however, considered proprietary.

PICA (see references 25 and 26) was the TPS material chosen for the baseline forebody heatshield material. PICA is a high-performance, relatively light weight ablative material which was extensively tested in the Arc-jet at high heat flux for the successful Stardust mission. Stardust is the highest velocity Earth reentry mission to date. A high fidelity material response model compatible with FIAT was developed in connection with the Stardust development work. Other TPS materials considered for the baseline heatshield design included AVCoat(Apollo), Carbon-Carbon(Genesis), SLA-561V, etc.

The FIAT-based design for a single thickness heatshield using PICA as the design TPS material and the undershoot trajectory heat pulse of Figure 32 yielded a PICA unmargined thickness of 4.724 cm thick with 2.032 cm of recession (see Figure 33). The areal density for PICA of this thickness is 11.66 kg/m^2. The rather substantial recession appears to be the consequence of the high heat pulse early in the design trajectory and of the highly oxidizing characteristic of the dissociated gases behind the bow shock to which the TPS char surface is exposed. One concern of such a high recession rate must be the effect on aerodynamic properties during the aerocapture maneuver associated with the resultant shape change of the heatshield.

The TPS specified for the aftbody was obtained by a process similar to that described for the forebody heatshield. A simplified engineering estimate of heating pulse for the design trajectory was provided as 5% of the forebody heat pulse throughout the trajectory. An unmargined thickness of 1.98 cm for SLA-561V with no recession and an areal density of 5.06 kg/m^2 was determined suitable for the afterbody design. Silicone Impregnated Reusable Ceramic Ablator (SIRCA) was considered to be a close alternative aftbody TPS material with 2.28 cm unmargined thickness and 5.48 kg/m^2 areal density.

The split lines chosen for the forebody versus aftbody regions were aft of the vehicle maximum diameter where the shoulder radius is tangent to the conical aftbody. The forebody exposed area is 19.88 m^2 giving a forebody TPS mass for PICA at 231.8 kg (unmargined thickness), while the aftbody exposed area is 29.28 m^2 giving an aftbody TPS mass for SLA-561V at 145.75 kg (unmargined thickness). A TPS contingency of 30% was applied for both the forebody (1.417 cm) and aftbody (0.594 cm), with an additional 50% factor of safety applied to the forebody recession thickness (1.016 cm), and 10% factor of safety applied to the aftbody unmargined thickness (0.198 cm), see Table 13. The resulting forebody baseline TPS mass (with margins) is 347.3 kg with PICA thickness of 7.158 cm. The resulting baseline aftbody TPS mass (with margins applied) is 204.1 kg with 2.772 cm of SLA-561V.

One observation to be made is that the baseline TPS mass estimates obtained for the MASS are about twice that which might be derived from historical estimates. There are several reasons for the current

high baseline TPS mass estimates. The primary cause of the present high TPS mass estimates is high turbulent heating that occurs on the leeside of the forebody heatshield throughout the design trajectory. The transition to turbulence occurs due to the large aeroshell diameter of the present vehicle design and due to a high turbulent heat transfer bump factor associated with the 70° sphere cone once transition does occur. This suggests that alternative heatshield shapes might be explored (see Appendix E: Assessment of Alternative Forebody Configuration for Reduced Heating).

A further cause of the present high baseline TPS mass estimates is the simplified single-thickness TPS sizing approach used for the MASS. Such an approach leads to the entire heatshield being of the same thickness as is required for the peak heating location. Further, the engineering approximations used in the single thickness design lead to a more conservative margin (50% on heat transfer, 50% on recession and 30% on thickness) than could be realized through a higher -fidelity based approach.

A preferred thermal protection system design methodology such as described in reference 29 would lead to a less massive variable thickness heatshield design when generated by a high-fidelity based integrated design environment. In the method reported in references 27, 28, and 29, a relatively sparse (10x3x3 minimum) aerothermodynamic database is established in Mach-Q-Alpha space using solutions from a real-gas Navier-Stokes code such as DPLR or LAURA and when required a gas-phase radiation code such as non-equilibrium air radiation (NEQAIR) code. To then examine the variation of heat transfer to the entire surface of a proposed vehicle traveling a particular proposed design trajectory, an engineering methods based code such as CBAero is then used to accomplish "smart interpolation" between the aerothermodynamic solution points. This design trajectory's heat pulse variation with time then provides the input to the FIAT material response code being run for each surface point on the heatshield being analyzed. Resulting is the TPS thickness required at each of many points on the exposed surface of the fore and aft heatshields. As the heat transfer levels are derived from high-fidelity real-gas Navier-Stokes solutions, the potential for greater accuracy and reduced margin requirements exist by such an integrated design approach. The primary difficulty with this approach is that even with the sparseness of the aerothermodynamic database, roughly 100 Navier Stokes solutions are typically required to populate the database. Once such a database is established for a particular vehicle shape, however, it can be used for many proposed trajectories and candidate TPS materials. Such resources were not available for the purposes of this study, but typically would be for a full mission design.

In summary, a baseline thermal protection system design for the forebody and aftbody has been accomplished based on a simplified and conservative single thickness heatshield approach. The baseline forebody heatshield is composed of PICA with thickness of 7.158 cm and 347.3 kg including margins but not including the mass of the substructure. The baseline aftbody TPS system is composed of SLA-561V with thickness of 2.772 cm and mass of 204.1 kg including margins but not including the mass of its associated substructure.

With the high turbulent heating rate, and the uncertainty of the ability to fabricate PICA in the sizes necessary for this size aeroshell, alternatives to the baseline TPS were assessed. An alternative configuration using an elliptical forebody in lieu of the 70° sphere cone shape was assessed with the results provided in Appendix E. Two alternative materials (Carbon-Carbon and SRAM-20) were assessed as alternatives to PICA, on the 70° sphere cone forebody. The results of the alternative materials are provided in Alternative Heatshield Material Systems section.

Alternative Heatshield Material Systems

SRAM Family

ARA is developing an extensive array of TPS material systems for use on entry bodies in recent years, under ISPT and MSL funding. ARA provided an assessment of one of their family of ablative TPS materials (SRAM-20) for this environment. The forebody peak heat rate exceeds the capability of the traditional SLA-561 family of materials previously used at Mars, consequently, alternative material systems are needed. The thermal response of the SRAM-20 material is shown in Figure 34. These results have been developed using the same heating profile (Figure 29 and Figure 32), with the baseline forebody structure. The thickness, mass, and margin assumptions for the SRAM-20 TPS are provided in Table 14. The analytical results indicate the fully margined single thickness SRAM-20 forebody heatshield would have a thickness of 2.59 cm and a mass of 165.3 kg.

Carbon-Carbon Hot Structure

Lockheed-Martin Astronautics in Denver performed an assessment of using a Genesis-derived Carbon-Carbon hot structure for the heatshield system. This concept has been developed under ISPT and manufactured at a 2.5-m diameter scale, with the technology advances resulting in a 30-40% mass savings over the Genesis heatshield. The carbon-carbon structure is a laminate which consists of a T300 based carbon composite structure with Calcarb foam insulation behind the structure with high temperature blankets on the inside surface. This implementation is a hot structure and so it is different than the baseline implementation of a composite primary structure with a TPS system applied to the structure (and the SRAM-20 alternative). The carbon-carbon system was designed to the same heating profile (Figure 29 and Figure 32) to provide a consistent sizing comparison. In addition to the thermal response, this structure also needed to be sized to accommodate the structural loads (applied external pressure and the deceleration loads). The basic sizing results indicated 12 carbon-carbon integral ribs and 3 concentric carbon-carbon integral rings with a varying shell thickness of 0.36 to 1.37 cm. The calculated carbon-carbon recession was 0.104 cm, with 4.06 cm of calcarb high temperature insulation and an 11-layer high temperature blanket. The summary thickness and mass results for the carbon-carbon heatshield system are provided in Table 15.

TPS Comparison

Alternative TPS materials were considered to address the concern about the ability to manufacture PICA baseline TPS in the requisite sizes for this application. The comparison in terms of mass for the three TPS materials considered is provided in Table 16. Both the carbon-carbon and the SRAM-20 materials provide a lower mass alternative. While reducing launch mass is a critical metric, the reduction in TPS mass has only a moderate impact on the overall conclusion. The primary mass is propellant which is driven by the mass of the propulsion stage and the ERV stage. The aerocapture stage only influences the cruise stage propellant. So reducing the TPS by up to 182 kg, will only reduce the cruise stage propellant by 21 kg. Also, reducing the TPS mass will reduce the load carried by the aeroshell structure, so the structure mass could be reduced by another 25 kg. The maximum launch mass savings estimated to be realized by a forebody TPS change would be 296 kg (includes 30% contingency), which still results in the launch vehicle not closing. Consequently, the decision was made to maintain the baseline PICA TPS. Given an additional design cycle, which would address redesign of many other elements as well, the TPS would be changed as part of an overall mass reduction program.

Structural Configuration

The structure was evaluated in two distinct analyses. The aeroshell structure was analyzed as a stand-alone unit with the payload attached at the payload ring on the forebody. The payload support structure and separation planes were evaluated as a stand-alone unit with the influence of the aeroshell mass taken into account.

System Packaging

Packaging of the system blends the physical packaging of the systems within the aeroshell coupled with the strategies for separating the Propulsion Module and the ERV. A secondary packaging constraint is the need to achieve an offset of the center of gravity of the entry system to allow the entry body to fly at an angle of attack during the aeropass. Packaging of the systems was an iterative process to achieve the desired configuration.

Payload Structure Conceptual Design

There are four required separations for the MASS flight system (Figure 35):

1. Cruise stage separation

2. Forebody/Heatshield separation

3. Backshell separation from payload

4. Propulsion Module separation

Keeping the loads out of the aeroshell itself requires an internal structure to hold the main components together with separation planes between them. This internal structure must hold the individual tanks together and allow the two vehicles (Propulsion Module and ERV) to separate from each other and from the heatshield and backshell.

Three structural configurations are examined. The first configuration has the loads passing directly through each vehicle. This means that the load path during launch goes from the aeroshell to the Prop Stage, and then through the #4 separation plane, the ERV, the #1 separation plane, and finally to the Cruise Stage. In this case, pass through loads are taken through the Prop Stage and ERV vehicles during launch and entry, whether it be through the tanks or other secondary structure.

The second configuration looks at the load differences when the aeroshell is connected to the ERV, not the Prop Stage. The load path during launch would be from the aeroshell to the ERV, and then to the #4 separation plane, Prop Stage, the #1 separation plane, and then Cruise Stage.   There are slight difference in the loads between these two cases because of the differences in mass between the two vehicles, and the different g-loads taken on a nose-up launch compared to a nose down entry. Some of the forces seen in the second configuration are smaller, but there is added length in some of the primary structure, and pass through loads in the vehicles still exist.

The third configuration, which can be observed in Figure 43, has the loads from the aeroshell, located at a payload ring, passing from the payload ring to a Mid Separation Plane. This Mid Separation Plane will take loads independently from the aeroshell, Prop Stage, and ERV and send them to a Cruise Separation Plane. The load path then goes from the Cruise Separation Plane to the Cruise Stage. This third configuration is chosen because of the avoidance of pass-through loads in both vehicles, and the

ability to separate massive structure from the vehicles after aeroshell separation. Note that there are clearance holes in the backshell for the reaction control subsystem (RCS) thrusters for control during the aerocapture maneuver.

Editing Team X Study

The Team X study for the aerocapture, last updated on June 1, 2005, made several assumptions about the aerocapture that have since been changed. The Team X study assumed the load path from the payload mass travels through the aeroshell during entry. The Team X study also has the Prop Stage located below the ERV (launch). The mass estimate from the Team X study were: aeroshell - 2752 kg, the ERV - 2867 kg, and the Prop Stage - 3422 kg. These estimates for the vehicles included primary and secondary structure for the individual stages as well as attachments and adapters between the stages, however, pass-through loads in the Prop Stage were never accounted for during the original study because of time constraints. Because of this, 150 kg (without contingency – per Gerhard Klose 09/27/2005) was added to the Prop Stage primary structure bringing the Team X study total launch mass, including Cruise Stage, to 9559 kg, with contingency.

New Mass Estimates

The mass for the new structure is estimated based on parametrics and comparisons to previous missions. The Payload Ring Separation Plane and Cruise Separation Plane are estimated to be 52 kg. The Mid Separation Plane is estimated to be 65 kg. All three truss structures are estimated to be 208 kg. These estimates are with contingency. The additional structure mass with contingency is 793 kg.

Mass estimates for structural elements from the original Team X model are now consistent with the new structural mass estimates. They are paired up and replaced with structural elements from the new design (Figure 36). The added 150 kg to the primary structure of the Prop Stage in the Team X study is removed since there are no longer any through-loads in the Prop Stage.

Total launch mass saved from taking structure out of the aeroshell and creating new internal structure is 1244 kg, with contingency. This can be seen in Table 20, comparing the Team X aeroshell mass with the MASS aeroshell plus mid-truss stage masses. These results do not consider the new propulsion requirements based on these new mass estimates.

Payload Structure Stiffness Evaluation

The payload structure mass was estimated parametrically. A more in-depth evaluation was performed to verify the "order of magnitude" results. A simple beam element finite element model (FEM) was created of the payload support structure trusses and rings. The payload was split into ERV and Prop Stage/aeroshell and modeled as simple concentrated masses. The estimated masses used represented a snapshot in time. The primary design/sizing driver was structural stiffness. Several iterations were made to get gross "EA" and "EI" structure requirements to meet launch stiffness requirements. A finite element model of the payload structure is shown in Figure 37.

Table 17 lists the component mass estimates. The assumed material for the tubes and rings was Gr/EP IM7/977-2 composite. The total stackup mass estimate of 799 kg compared very closely with the original parametric value of 793 kg, so no further payload structure analysis was performed

Aeroshell Structure

General Description

The aeroshell structure consists of a forebody, backshell, and payload attach ring. The forebody is a 70° sphere-cone with a maximum diameter of 4.65 m, a 1.163 m nose radius, and a 0.116 m shoulder radius. The backshell is a single conic frustum with a 32.5° half angle from vertical. The total aeroshell height is 3.18 m (see Figure 42 and Figure 43). The payload ring diameter is 1.8 m, and is permanently attached to the forebody. The payload ring attaches the aeroshell to the payload via eight separation fittings, with six separation fittings attaching the backshell to the forebody. The original Team X report had a very large aeroshell mass of 2752 kg, based on parametric scaling of previous aeroshell structure, primarily using an historic mass fraction. A more in-depth analysis was required to develop accurate aeroshell mass for improved trajectory, aeroheating, and TPS analyses.

Structural requirements

The structure must be sized for sufficient strength and stiffness for launch and aerocapture loading environments. Per the Delta IV-4050H-19 Payload Planner's Guide launch load envelope the payload must sustain launch accelerations of 6 g's axial combined with 0.5 g's lateral, and 2.3 g's axial with 2.0 g's lateral. A final iteration 3σ peak deceleration value of 5.2 g's during aerocapture was calculated from a Monte Carlo entry analysis, assuming 16° angle of attack. For structural analysis, factors of safety of 1.4 are added for ultimate strength of metals and composites, 1.25 for yield of metals, and 1.5 for buckling. Natural frequency minimums at launch are 8 Hz for first lateral mode and 30 Hz for first axial mode, also per the Payload Planner's Guide.

Analysis Assumptions and Methods

Several iterations were done on the aeroshell structural sizing, with different assumptions made based on the maturity level of the full design and individual subsystems. For all iterations, some basic assumptions remained constant. At launch the aeroshell was nose up with the payload structure supporting the aeroshell at the forebody payload ring. The payload structure load went through the backshell and was the primary load path during launch, leaving the aeroshell "hanging" and supporting only its own mass and inertia loads at launch. At aerocapture, the forebody was nose down with a coarse aerocapture pressure distribution applied to the forebody to balance payload and aeroshell inertia loads at entry g levels. Specific aeropressures and entry g values varied through the iteration process, with 5.2 g's being the final value. To envelope the structure sizing, contingency values for payload and TPS mass were applied, with the resulting aeroshell structure mass being the current best estimate (CBE) structure mass value.

A plate element FEM, shown in Figure 38, was created to represent the aeroshell structure. The forebody was tied to the backshell at six equally spaced points with rigid elements representing separation fittings. The payload was represented as a point mass, tied to the payload ring with a constraint element. First and second round sizing iterations used 6500 kg and 6999 kg for the payload, respectively. The payload CG was adjusted so that the combined payload-aeroshell CG would balance the aeropressure loads at 16° angle of attack. The initial FEM was created using ProbeMASS1, a quick sizing tool in development at NASA LaRC. It was modified in the commercial software SDRC I-DEAS™ to add the forebody/backshell attachments, launch boundary conditions, and aerocapture pressure distributions, as seen in Figure 38. The I-DEAS solver was also used to get internal structure loads at launch and aerocapture using static and inertia relief solutions, respectively. A universal file containing the mesh and

internal loads was then input into the commercial software Hypersizer® where a large trade space of designs, materials, and sizing parameters were evaluated. Closed form solutions checked local component strength and stability and output the lowest mass structure. These results were then manually "smeared" to allow for a manufacturable structure, and a second universal file was created which was read back into I-DEAS for another round of iterations. The aeropressures and payload CG were adjusted to balance the new aeroshell-payload mass combination for the given entry g's. Natural frequencies at launch configuration and global buckling at aerocapture configuration were also checked in I-DEAS at this time.

Since no TPS analysis or mass estimates had been done at the start of the structural sizing, the first round of model balancing and sizing was based on an initial guess of aeroshell structure mass and TPS mass using trend curves of historical data contained in ProbeMASS1. The initial TPS sizing was based on SLA-561V material, assuming the Team X estimated heat load of 124 MJ/m^2. Figure 39 and Figure 40 show the trend curves for aeroshell forebody structure and TPS mass, respectively. Later calculations, as discussed elsewhere in this report, showed the need to use PICA TPS material for the forebody and SLA-561V for the backshell, both at much higher areal densities than were estimated for the first round of structural iterations.

The aeroshell mass estimates from the first round of sizing iterations were input back to the systems study team for further iterations on entry analysis, guidance, and TPS sizing. Revised entry g loads and TPS mass estimates, as discussed above, were then used for the next set of aeroshell sizing iterations, using the finite element procedures outlined above.

Aeroshell Sizing Results

The resulting aeroshell structure was a honeycomb sandwich construction for the forebody and backshell, and a stiffened panel concept for the payload ring. The resulting forebody is 0.2794 cm (0.11 in) quasi-isotropic Graphite polyimide (Gr/PI) face sheets on 2.54 cm (1.0 in) 5052 aluminum honeycomb core. The backshell cone, top and interface ring are 0.1397 cm (0.055 in) quasi-isotropic GR/Pi face sheets on 1.27 cm (0.5 in) 5052 aluminum honeycomb core. The payload ring is a 7075 aluminum Z-stiffened panel in a ring shape. All components had positive margins of safety as calculated from the Hypersizer software. The resulting CBE masses from the analysis are shown in Table 18.

An additional 7% of the forebody and backshell primary structure mass (14.7 kg and 10.9 kg, respectively) was included in the Master Equipment List (MEL) to account for secondary structure (brackets, assembly hardware, etc.) not obtained from the analysis.

For the launch configuration with the aeroshell held at the payload ring, Modes 1 and 2 are 16.7 Hz, lateral motion, and Mode 3 is 30.34 Hz, axial motion. These natural frequencies for the aeroshell alone are above launch requirements. Due to the use of parametric mass scaling for the payload structure and cruise stage, no finite element modes were available to create a full stackup model, and so full launch stackup natural frequencies were not determined.

At aerocapture loading, the buckling eigenvalue is 7.84, based on an inertia relief buckling solution in I-DEAS. This value exceeds the lower threshold requirement of 1.5. The buckling shape is shown below in Figure 41.

Spacecraft Description

Even with the use of aerocapture at Mars arrival, the total on-board ΔV required from the Orbiter/ERV is very substantial, exceeding 5.5 km/s, for this opposition class mission. Because the propulsive requirements are so high, multiple staging events are used to lighten the spacecraft as much as possible prior to the TEI maneuver. For the MASS, a multi-stage design for the Orbiter/ERV was developed, which divides the vehicle into five major elements, four of which are staged prior to the TEI maneuver: the Cruise stage, the Aerocapture stage, the Mid-Truss stage, the Propulsion Stage, and the main ERV. In addition, 79 kg of sample capture hardware is jettisoned from the ERV prior to TEI. This staging approach was derived from a multi-stage Orbiter/ERV design developed in a previous study conducted by the JPL Advanced Projects Team (ref. 6). The Team X design was substantially modified in the MASS, with major changes to the spacecraft's primary structure and TPS including the addition of the mid-truss stage.

It should be noted that no systematic effort has been made to optimize the number of stages or the point at which the stage separation events should occur. The main reason the staging occurs prior to the TEI is because there is a desire to avoid autonomous staging in the middle of the maneuver occurring at periapsis. Some further reduction in launch mass may be achievable by staging differently or possibly by adding an additional propulsion stage.

Figure 42 and Figure 43 show the overall vehicle configuration. The propulsion stage is located at the front of the vehicle and the ERV at the back, with both elements surrounded by the primary truss structure and aeroshell elements. The vehicle is launched nose-up and fits within the faring of a Delta IV-4050H-19 launch vehicle. The allowable diameter of the aeroshell is limited by the diameter of the launch vehicle fairing.

In an effort to lower the mass of the aeroshell, a structural design that carries primary structural loads through the spacecraft rather than through the aeroshell has been adapted. This allows for a substantial reduction in the mass of the aeroshell, giving an aeroshell mass fraction (defined as aerostage mass / entry mass) of approximately 15%. This is much lower than the 30% used in the Team X study. The vehicle design is based around a truss structure that carries primary loads around (not through) the ERV and propulsion stage. The aeroshell stage connects to a payload ring at the front of the vehicle, while the propulsion stage and ERV connect to the mid-separation plane shown in Figure 43. Details of the structural design are available in the Structural Configuration section. The truss structure is relatively massive and is discarded in stages after the aeroshell separation. This minimizes the mass carried in large propulsive maneuvers and lowers the propellant mass required by the vehicle.

A summary mass budget for the overall vehicle is shown in Table 19. Detailed MEL's for each element are provided in Appendix A.

Table 19 shows that the total system launch mass exceeds the capability of the launch vehicle by over 1000 kg. This result is not unexpected, as previous work by JPL's Team X also concluded that this configuration has negative mass margin (ref. 6). Although aerocapture substantially lowers the mass of the system compared to an all propulsive architecture for this opposition class mission, the high propulsive requirements for the system on the return leg result in a total propellant loading of over 5000 kg for the vehicle. A comparison between the masses calculated in this study and those generated by Team X is shown in Table 20. The Team X results are taken from an update to (ref. 6) generated in Jun 2005.

The overall launch mass of the Team X option is approximately 500 kg more than that of the current vehicle in the MASS. The main source of this difference is the lower mass of the aeroshell and backshell used in the current study. It is interesting to note that aeroshell to entry mass fraction of the current design is much lower than that used in the Team X study. Team X chose to size the aeroshell using a simple "rule of thumb" which assumes the mass of the aeroshell is equal to 30% of the total entry mass. MASS used more accurate structural and thermal analysis tools to design the aeroshell.

One of the goals of the MASS was to determine if the entry mass fraction used by Team X is applicable to very large aerocapture vehicles. The results of this study suggest that a lower fraction than 30% is appropriate for large vehicles. However, it should be noted that the total launch mass savings (~500 kg) is much less than the savings achieved in the aeroshell stage (~1500 kg). This occurs because part of the aeroshell mass savings in this study is achieved by changing the structural load path so the launch loads associated with the aeroshell are carried through the spacecraft's primary structure rather than through the aeroshell itself. Although this lightens the aeroshell, it also requires additional primary structure mass in the ERV, mid-truss, and propulsion stages. The net structural mass added to the non-aeroshell portions of the vehicle is less than the dry mass saved within the structure of the aeroshell stage. Although the structure is staged as the mission proceeds, a portion of the added structural mass is carried through the propulsive maneuvers occurring after sample collection. In particular, the dry mass of the propulsion stage in the current design is much higher than the dry mass of the propulsion stage in the Team X design largely because of the added mass associated with the primary truss structure. The wet mass of the vehicle increases as propellant is added to accelerate the added structural mass, substantially reducing the net mass savings to the overall vehicle. For future work, it would be desirable to design an aeroshell that carries launch loads though its internal structure to determine if that configuration is more mass efficient overall for this mission.

Cruise Stage

The cruise stage is mounted external to the aeroshell and provides propulsion and communications services after launch and prior to the aerocapture maneuver at Mars. The stage incorporates a monopropellant chemical propulsion system that uses 16 thrusters for TCM's, attitude control, and targeting prior to Mars arrival. It also incorporates a small X-band antenna for communication with Earth. The entire cruise stage is separated from the aeroshell and discarded prior to the aerocapture maneuver.

The mass of the propulsion, telecom, thermal, and harness subsystems were estimated directly from previous studies conducted by JPL's Team X. A detailed MEL for the cruise stage is shown in Appendix A. The cruise separation plane's structural elements are included in the MEL for this stage.

Aerocapture Stage

The aerocapture stage consists of the aeroshell (both forebody and backshell) and includes the TPS, separation devices, support structure, and interface structure connecting the aeroshell to the rest of the vehicle. The structural interface between the main spacecraft and the aerocapture stage is through a payload ring attached to the forebody. The backshell attaches structurally to the forebody and does not directly interface with the launch vehicle or the main spacecraft. The stage separation occurs after the aerocapture maneuver and before the periapsis raising maneuver and consists of two separate events; the forebody is initially separated from the main vehicle, the ERV/Prop stage is then extracted from the backshell and the backshell is discarded.

The elements of this stage were designed for this study as described in detail in the body of this report. A detailed MEL for the aerocapture stage is shown in Appendix A.

Mid-Truss Stage

The mid-truss stage consists entirely of external primary structure designed to support the spacecraft during launch and aerocapture. This structure is not needed after the aerocapture maneuver and is jettisoned just after the aerocapture stage is released. This element was designed for this study as described in the Structural Configuration section. A detailed MEL for the mid-truss stage is shown in Appendix A.

Propulsion Module

The propulsion stage provides primary and secondary propulsion for the post-aerocapture apoapsis raise maneuver and for the apoapsis raise and periapsis lowering maneuvers that occur just prior to TEI. The propulsion stage consists of a large dual-mode bipropellant propulsion system and its associated thermal control and structural hardware and includes the external truss that connects the structural mid-plane to the aeroshell structural support plane. The stage sits above the ERV in the launch configuration and interfaces to the ERV though a series of separation points connected to the main structural ring on the ERV. The stage interfaces to the aerocapture stage through a payload ring. The major elements of the propulsion stage are shown in Figure 44.

The propulsion stage is scaled from a propulsion stage design previously developed by Team X (ref. 6). The mass of the tanks was scaled from the Team X design by assuming that the overall tank mass fraction (fraction of tank dry mass to propellant wet mass) remains constant as one increases or decreases the amount of propellant in the tank. This assumption is valid for custom sized propellant tanks which are relatively close in size to the original Team X tanks. The assumption is valid in this case, as the final tank capacity is within 10% of the tanks defined in the original Team X study. A detailed MEL for the propulsion stage is shown in Appendix A.

Earth Return Vehicle and Earth Entry Vehicle

The Orbiter/ERV provides primary and secondary propulsion for the TEI maneuver and for the deep space maneuver executed after the VGA. The Orbiter/ERV also provides power as well as command and data handling for all elements of the vehicle stack and provides the tracking and capture hardware necessary to capture the OS. The Orbiter/ERV also provides the majority of the telecommunications hardware necessary to communicate with the Earth through all phases of the mission. Two ultraflex solar arrays provide power for the vehicle. The major elements of the ERV are shown in Figure 45.

The designs for the attitude control system, power system, command and data handling system, telecommunications system, and thermal system are all derived from a previous study conducted by Team X. Mass estimates for the EEV and Sample Capture Hardware were provided by the Mars Advanced studies program office. The propulsion system mass is scaled from a previous Team X design by assuming that the overall tank mass fraction (fraction of tank dry mass to propellant wet mass) remains constant as one increases or decreases the amount of propellant in the tank. This assumption is valid for custom sized propellant tanks, which are relatively close in size to the original Team X tanks. The assumption is valid in this case, as the final tank capacity is within 7% of the tank capacity defined in the original Team X study. The structure was designed for this study.

Cost Assessment

The following section describes the models used to perform the cost assessment, the groundrules and assumptions for the estimate, and the results of the assessment.

Description of Cost Models

NAFCOM

NASA/Air Force Cost Model (NAFCOM) is a parametric estimating tool for space hardware that uses cost estimating relationships (CERs) which correlate historical costs to mission characteristics to predict new project costs. It is based on historical NASA and Air Force space projects and is intended to be used in the very early phases of a development project. NAFCOM can be used at the subsystem or component levels and estimates development and production costs.

SOCM

The Space Operations Cost Model (SOCM) is an evolving, multi-level, constructive model that estimates the costs and staffing for space operations projects by a comparison of mission characteristics to an advancing "State of the Practice" (SOP). High-level project characteristics are used to generate a Level 1 estimate with a ± 30% accuracy. A more detailed characterization of the project's operations implementation strategy is used to refine the Level 1 estimate, and thus generate a Level 2 estimate with improved accuracy.

Cost Assumptions

1. All estimates presented in fiscal year (FY) 05$M

2. Fee (10%) and Program Support (25%) included

3. December 2013 Launch Date

4. Used NAFCOM to estimate the following mission segments: ERV, Prop Stage, Mid-Truss Stage, Cruise Stage, and Aeroshell

5. Cost for the EEV and Sample Capture System including Optical Navigation Cameras taken from reference 6.

6. No scientific instruments included

7. No cost for the Lander or any systems associated with the lander delivery, Entry, Descent, Landing, or MAV are included

8. Launch Vehicle cost obtained from Mars Program Advanced Studies request to KSC (through NASA HQ) for launch services costs for future missions to be used in development of the POP inputs.

9. Included standard Education/Public Outreach levels (1% of Total Cost less Launch Vehicle)

10. JPL Design Principles used to determine reserve levels (30% Phase B/C/D, 15% Phase E)

11. SOCM used to estimate Phase E costs (assumed 22 months total mission and 3 months intense ops)

Cost Estimate Results

The results of the cost analysis are presented in Table 21. The cost and estimating methodology is identified by Work Breakdown Structure element.

Technology Assessment

As part of the study, assessments of the influence of technologies which could either enhance, or enable the mission were performed. Since the study was focused on a nearer term solution, only near term technologies were considered. The basic technology which influences the mission is the use of aerocapture itself. The second tier elements influencing the mission, are any elements significantly influencing the overall launch mass. Since the majority of the mission mass is split between propellant, structure and TPS, there are only limited technologies to assess. While avionics and power systems are continually having their mass and power reduced, their mass is inconsequential for this class of a mission. Technologies considered were divided into enhancing and enabling technologies.

Enabling Technologies

In general, no enabling technologies were identified.

Aerocapture itself was envisioned to be an enabling technology itself for the Fast-Return (Opposition-Class) mission. The mission did not close using the largest expendable launch vehicle while maintaining a 30% contingency. If the contingency was reduced to approximately 10%, then the mission would close and thus aerocapture could be enabling. Further efforts to reduce the major mass components could result in the ability for the mission to close.

Aerocapture itself is an enabling technology for the Conjunction class return missions. Aerocapture is also enabling for large orbiters.

Enhancing Technologies

MASS can most likely be implemented within existing capabilities. Further development work is required for TPS, to demonstrate manufacturing at the 4.65 m scale. Current monolithic PICA fabrication is limited to approximately 1 m diameter; manufacturing to 1.75 m may be demonstrated by 2008. The use of PICA on a 4.65 m scale requires joints, which need additional analysis and testing. This is also the case for SRAM-20 at the large scale. The Carbon-Carbon heatshield system concept has been demonstrated at the 2 m scale and is supported by high-quality predictive models that should allow it to be scaled up without additional large-scale manufacturing tests.

Validation of the CFD tools for the hypersonic turbulent flow regime is an enhancing technology area. At present, without that validation, significant uncertainty values are used on the heating, which increases TPS mass. Also, without a good knowledge of the actual margins being carried in the TPS system, it is difficult to make risk-based technical decisions. Lowering these uncertainties can allow the aerocapture system hardware to be more efficient, possibly resulting in enhanced science return.

Future Efforts

With the completion of the MASS, recommendations for future efforts are also provided. The following are areas suitable for additional study.

1. Mission Design - Reassess mission design constraints and see how close some were - can they be relaxed? Is there an opportunity beyond 2024?

2. Aerothermal - Reduce environmental uncertainty through additional analysis and testing. Current computational tools are not validated for predicting turbulent aerothermodynamics in a hypersonic Mars environment

3. Aeroshell - Integrate aeroshell with payload structure and cruise stage to check full stackup structure (stress, buckling, natural frequencies, etc.).

4. Aeroshell - Optimize aeroshell-payload structure interface diameter.

5. Aeroshell - Evaluate alternate structural concepts such as substituting or integrating hot structures.

6. Aeroshell - Evaluate alternate structural load paths such as backshell vs. payload structure as primary load path.

7. TPS - Assess alternate forebody geometry (modified ellipsoid) - with the goal of reducing turbulent heating and thus reducing TPS mass

8. TPS - Develop integrated TPS Design Environment (e. g., NS-CBAero, FIAT, TPSSZR) - resulting in a Variable surface TPS thickness and thus reducing TPS mass

9. Aerothermal and TPS -Perform combined Monte-Carlo analysis bringing together aerothermal uncertainties with TPS uncertainties to generate an integrated probabilistic answer. Should reduce TPS mass.

10. Programmatic - Consider a change of problem statement to focus on "Large Science Orbiter" for Mars and define when Aerocapture is a viable alternative

11. Programmatic - Consider a change of problem statement to focus on "Fast Arrival" to assess implications of using Aerocapture to enable significantly higher arrival energies than typically used for Mars orbiters.

Concluding Remarks

Assessment of the use of aerocapture for the Opposition class return for an MSR mission with the defined mission implementation constraints could not close using existing expendable launch vehicles. With additional design and analysis effort, a different conclusion may be reached in that the mission could close. Aerocapture enables the delivery of large payloads to Mars or Venus. Aerocapture also enables delivery of moderate payloads to outer planet destinations. The HYPAS algorithm is the baseline GNC algorithm and has been found to be very robust and resilient across the entire spectrum of aerocapture. Current technologies are sufficient for demonstration of aerocapture which would allow it to then be an additional alternative to mission planners.

Acknowledgements

Appendix A: Baseline Master Equipment List

All hardware elements and propellant masses were computed using either parametric tools or definition of existing hardware or derived from the design efforts as part of this study. The MELs are provided for the ERV (Table 22), the Propulsion Module (Table 23), the Mid-Truss Stage (Table 24), the Aeroshell Stage (Table 25), and the Cruise Stage (Table 26).

Appendix B: Fast Return Trajectories 2013-2025

This study included an assessment of the Mars opportunities from 2013 through 2025 (see Table 5). Provided in this appendix are the general trajectory plots for these opportunities for the cases of excessive Mars departure C_3 (Figure 46) and excessive Earth to Mars trip times (Figure 47).

Appendix C: Mass/Maneuver Calculation Tables

Calculations for the baseline aerocapture case indicating the mass changes including propellant usage for each mission maneuver or event are provided in Figure 48. For comparison, the similar mass and maneuver calculation set is provided for the All-Propulsive option as shown in Figure 49. The basic comparison of these two options illustrates the dramatic reduction in mass afforded by aerocapture for this architecture, with a greater than factor of 3 mass reduction.

Appendix D: Comparison of the TES Limb Measured Atmospheric Profile to the Standard MarsGRAM Atmospheric Profile

A 2000-run Monte Carlo analysis was performed for the nominal 300 kg/m^2 BC case to test the Mars-GRAM 2005 TES limb-measured auxiliary atmospheric profile feature. The TES observation density auxiliary profile, in comparison to the MGCM climatology, can have up to 40% lower density than density observed by TES limb sounding at low to mid latitudes and altitudes above 40 km. The uncertainties used in the Monte Carlo analysis are exactly the same as for the 300 kg/m^2 BC case   (see the Monte Carlo Uncertainties for 300 kg/m^2 BC table in the Guidance and Integrated Trajectory Performance section). It should be noted that the HYPAS guidance was not retuned from the nominal for the TES profile comparison.

The results from the 2000-run Monte Carlo analysis are presented in Figure 50 through Figure 53. The TES performance in the Monte Carlo analysis showed slightly better results than the 300 kg/m^2 BC without the profile due to the higher density values from TES, and also proved a robust HYPAS guidance algorithm since there was no retuning from the nominal 300 kg/m^2 BC case. Figure 50 shows the final apoapsis altitude versus the periapsis altitude at atmospheric exit, before a circularization maneuver is performed. The resulting dispersion in apoapsis altitude is 497.7 km ± 24.1 km (3σ). Figure 51 shows

the ΔV required for orbit circularization after aerocapture. The circularization ΔV dispersion is 122.1 m/s $\pm$ 5.1 m/s (3σ). The peak LAURA turbulent heat rate estimate is shown in Figure 52. The resulting dispersion in turbulent peak heat rate is 274.8 W/cm^2 $\pm$ 45.9 W/cm2 (3σ), and the total integrated turbulent peak heat load dispersion is 19051.4 J/cm^2 $\pm$ 1780.2 J/cm2 (3σ). Figure 53 presents the maximum loading, or deceleration, on the vehicle. The peak deceleration dispersion is 4.3 g's $\pm$ 0.9 g's (3σ).

Appendix E: Assessment of Alternative Forebody Configuration for Reduced Heating

Associated with the large diameter of the proposed Mars vehicle is that the forebody boundary layer will undergo transition to turbulence early in the aerocapture maneuver (prior to peak heating). High heating levels typically associated with turbulent flow then occur throughout most of the atmospheric flight portion of the trajectory. For many common heatshield geometries, transition to turbulence occurs predominantly over the leeside of the heatshield leaving the stagnation point laminar, but with turbulent heating bump factor on the leeside in excess of three.

Many Mars missions have made use of the 70° sphere-cone geometry heatshield, but for those missions, the vehicle was smaller than for the MASS concept such that the forebody boundary layer remained laminar throughout much of the atmospheric flight. The 70° sphere-cone heatshield geometry, however, proves to be particularly susceptible to excessive heating once turbulent transition occurs. On the lee-side of the heatshield the turbulent heating bump factor can reach as high as 6, causing the leeside turbulent heating to exceed even the heating level at the stagnation point (which may yet remain laminar). This turbulent excessive heating for the 70° sphere-cone is seen both in Navier-Stokes solutions for the MASS concept and in T5 experiments accomplished in support of MSL (ref. 32). As an example of this turbulent heating effect, Figure 54 depicts heatshield surface results obtained using the DPLR real-gas Navier-Stokes code for the peak heating time of one trajectory considered for the present MASS. For this trajectory point, the 70° sphere-cone of 4.65 m diameter is held at an angle of attack of 16° and the aerodynamic L/D is 0.24. Solutions were obtained for both laminar and turbulent flow over the heatshield with uncertainties. The DPLR results are consistent with the LAURA results (Figure 27 without uncertainties and Figure 29 with uncertainties). Figure 54 also shows the momentum thickness for the laminar solution. Using a transition criterion of Re_θ of 200, the stagnation point and windward portion of the heatshield is seen to remain laminar, while the leeside of the heatshield becomes turbulent (consistent with Figure 28). Figure 54 also shows both the laminar (on the figure's left half) and turbulent (on the figure's right half) heating levels obtained from the Navier-Stokes solver. As can be seen, turbulent peak heating actually occurs on the leeward-most shoulder far in excess of the stagnation point heating level. This turbulent heating susceptibility of the 70° sphere-cone suggests that, where turbulent transition early in the trajectory is likely, a search for a heatshield geometry as an alternative to the 70° sphere-cone may result in a decreased design heating pulse, both integrated and peak levels, with a possibility for relatively lighter density TPS materials and lower forebody TPS mass.

In order to explore this potential, an ellipsoidal heatshield configured to match the aerodynamic lift and drag properties of the 4.65 m diameter 70° sphere-cone heatshield at hypersonic velocities for the Mars atmosphere was assessed. Figure 55 depicts the ellipsoidal heatshield surface results obtained by the DPLR Navier-Stokes solver for the same trajectory conditions as for the Figure 54 70° sphere-cone heatshield results. For the ellipsoidal heatshield, transition occurs on the leeward side of the heatshield similar to the 70° sphere-cone. However, the peak turbulent heating for the ellipsoid heatshield is at a much reduced level relative to the 70° sphere-cone. The turbulent peak heating for the ellipsoidal heatshield is 163 W/cm^2 compared to 323 W/cm^2 for the 70° sphere-cone, a reduction of nearly 50%.

TPS sizing for the ellipsoid heatshield has been accomplished using a reduction of 50% in peak convective heat transfer as a characterization of the ellipsoid heatshield and applying that to the trajectory heating pulse of Figure 32. The FIAT material response code accounts for the reduction in convective heat transfer coefficient associated with the ablative mass blowing effect. For the simplified single-point approach used, similar to how the baseline TPS design was established, it is determined that SLA-561V is suitable for this peak heat transfer level with a thickness of 1.176 cm and a unmargined forebody heatshield TPS mass of 63.67 kg. Figure 56 compares this estimate for unmargined mass of the SLA-561V ellipsoidal heatshield with the 231.8 kg for the unmargined mass for the PICA baseline 70° sphere-cone heatshield. The considerable saving in TPS mass for the ellipsoidal heatshield relative to the 70° sphere-cone is the consequence not only of the reduction in thickness of the heatshield but also that a switch to the lighter density SLA 561V due to the much lower peak heating level. The reduction in peak heating by 50% for the ellipsoidal heatshield over the 70° sphere-cone thus leads to forebody heatshield with only 27% of the TPS mass.

A more thorough aerodynamic stability and aerothermodynamic analysis of the ellipsoid heatshield, followed by experimental validation, would be required before its use could be confidently recommended for a Mars mission. No optimization of the heatshield geometry was attempted, only that the hypersonic lift and drag levels were matched to the baseline 70° sphere-cone heatshield. The mass savings advantage of the ellipsoid heatshield seen here would likely be reduced for a variable thickness heatshield. However, there is sufficient potential demonstrated in this brief analysis to justify further exploration of heatshield geometry alternatives to the traditional 70° sphere-cone for future Mars missions.

References

1. Lockwood, Mary Kae, et. al., Aerocapture Systems Analysis for a Titan Mission. NASA TM-2006-214273, March 2006.

2. Lockwood, Mary Kae, et. al., Aerocapture Systems Analysis for a Neptune Mission, NASA TM 2006-214300, May 2006.

3. Lockwood, Mary Kae, et. al., Systems Analysis for a Venus Aerocapture Mission, NASA TM 2006-214291, April 2006.

4. Oberto, Bob. "MSR ERV Options 2004-05," JPL Advanced Projects Design Team, Team X Report #726, May 13, 2004.

5. Oberto, Bob. "MSR Mars Aerocapture Option 1" JPL Advanced Projects Design Team, Team X Report #X-746, July 30, 2004.

6. Oberto, Bob. "MSR Mars Aerocapture Option 2" JPL Advanced Projects Design Team, Team X Report #X-746, Aug. 19, 2004.

7. Mattingly, R. "The Many Faces of the Mars Sample Return Mission Architecture," AAS 05-066, 27th AAS Guidance and Control Conference, February 2005.

8. Duvall, A. L., Justus, C. G., and Keller, V. W., "Global Reference Atmospheric Model (GRAM) Series for Aeroassist Applications", AIAA-2005-1239. January, 2005.

9. Duvall, A. L., Justus, C. G., and Keller, V. W., "Global Reference Atmospheric Models for Aeroassist Applications", 3rd International Planetary Probe Workshop, Anavyssos, Attiki, Greece, 27 June - 01 July, 2005.

10. Justus, C. G., Duvall, A. L., and Keller, V. W., "Atmospheric Models for Mars Aerocapture", AIAA-2005-4106. July, 2005.

11. Haberle, R.M., M.M. Joshi, J.R. Murphy, J.R. Barnes, J.T. Schofield, G. Wilson, M. Lopez-Valverde, J.L. Hollingsworth, A.F.C. Bridger, and J. Schaeffer., "General circulation model simulations of the Mars Pathfinder atmospheric structure investigation/meteorology data", *Journal of Geophysical Research, 104*(E4), 8957-8974, April 25, 1999.

12. Bougher, S.W. and H. Shinagawa., "The Mars thermosphere-ionosphere: Predictions for the arrival of Planet-B", *Earth Planets Space, 50*, 247-257, 1998.

13. Bougher, S. W., G. M. Keating, R. W. Zurek, J. M. Murphy, R. M. Haberle, J. Hollingsworth, and R. T. Clancy., "MGS Aerobraking: Atmospheric Trends and Model Interpretation", *Advances in Space Research, 23*(11), 1887-1897, 1999.

14. Smith, M.D., J.C. Pearl., B.J. Conrath, and P.R. Christensen., "Mars Global Surveyor Thermal Emission Spectrometer (TES) observations of dust opacity during aerobraking and science phasing", *Journal of Geophysical Research, 105*(E4), 9539-9552, 2000.

15. B. Bragg, C. Cerimele, R. Delventhal, J. Gamble, O. Hill, R. Kincade, D. Lee, W. Long, R. McHenry, G. McSwain, K. Nagy, M. Richardson, R. Ried, B. Roberts, C. Scott, D. Smith, "A Design Study for an Aeroassist Flight Experiment," NASA Johnson Space Center, JSC-20593, June 1985.

16. C. Cerimele, J. Gamble, "A Simplified Guidance Algorithm for Lifting Aeroassist Orbital Transfer Vehicles," AIAA-85-0348, AIAA 23rd Aerospace Sciences Meeting, Reno, Nevada, January 1985.

17. Masciarelli, J., and Queen, E., "Guidance Algorithms for Aerocapture at Titan," AIAA-2003-4804.

18. Masciarelli, J., Westhelle, C., and Graves, C. "Aerocapture Guidance Performance for the Neptune Orbiter," AIAA 2004-4954.

19. Starr, B., and Westhelle, C., "Aerocapture Performance Analysis of a Venus Exploration Mission," AIAA 2005-5913.

20. Bauer, G. L., Cornick, D. E., and Stevenson, R., "Capabilities and Applications of the Program to Optimize Simulated Trajectories (POST)," NASA CR-2770, February 1977.

21. Tauber, M. E., Sutton, K. Stagnation-Point Radiative Heating Relations for Earth and Mars Entries. Journal of Spacecraft, vol. 28, no. 1. 1991

22. Chen, Y. K. and Milos F. S. Ablation and Thermal Response Code for Spacecraft Heatshield Analysis," JSR, Vol 36, No 3, May-June 1993.

23. Milos, F. S. and Chen, Y. K. "Methodology for Full-Body TPS Sizing of Access to Space Vehicles," AIAA 96-0614, Jan. 1996.

24. Squire, T.H., Milos, F.S., Hartlieb, G.C., and Rasky, D.J. "TPSX: Thermal Protection Systems Expert and Material Property Database," ICCE/4, Fourth International Conference on Composite Engineering, International Community for Composites Engineering and College of Engineering, Univ. of New Orleans, New Orleans, LA, 1997, pp. 937-938.

25. Tran, H.K., Johnson, C.E., Rasky, D.J., Hui, F.C.L., Tsu, M.-T., and Chen, Y.-K., "Phenolic Impregnated Carbon Ablators (PICA) for Discovery Class Missions," AIAA 96-1911, June 1996.

26. Covington, M.A., Heinemann, J.M., Goldstein, H.E., Chen, Y.-K., Sailinas, T.-S., Balboni, J.A., Olejniczak, J., and Martinez, E.R., "Performance of a Low Density Ablative Heat Shield Material, AIAA 2004-2273, June 2004.

27. Kinney, D. "AeroThermodynamics for Conceptual Design," by Kinney, D., AIAA 2004-31, Jan. 2004.

28. Kinney, D., and Garcia, J., and Huynh, L., "Predicted Convective and Radiative Aerothermodynamic Environments for Various Reentry Vehicles using CBAero," by AIAA 2006-659, Jan. 2006.

29. McGuire, M., Bowles, J., Yang, L., Kinney, D. and Roberts, C., "TPS Selection and Sizing Tool Implemented in an Advanced Engineering Environment," AIAA 2004-342, Jan. 2004.

30. Marvin, J.G., and Diewart, G.S., "Convective Heat Transfer in Planetary Gases," NASA TR R-224, July, 1965.

31. Olynick, D., Loomis, M., Chen, Y.-K., Venkatapathy, E. and Allen, G., "New TPS Design Strategies for Planetary Entry Vehicle Design, AIAA 99-0348, January, 1999.

32. Wright, M.J., Olejniczak, J., Brown, J.L., Hornung, H.G. and Edquistm, K. T. "Computational Modeling of T5 Laminar and Turbulent Heating Data on Blunt Cones, Part 2: Mars Applications," by Wright, M.J., Olejniczak, J., Brown, J.L., Hornung, H.G. An AIAA 2005-0177, Jan. 2005

Tables

Table 1: Comparison of MASS Aerocapture to Entry Missions

Parameter	Viking	MPF	MPL	MER	Phoenix (2007)	MSL 2009 (05-22)	MASS
Trajectory	Deorbit	Direct	Direct	Direct	Direct	Direct	Direct
Entry Mass (kg)	980	585	494	832	538	2804	8279
Payload Mass (kg)	600	370	290	421	364	1791	7087
Payload/Entry Mass Fraction	61.2%	63.2%	58.7%	50.6%	67.7%	63.9%	85.6%
Diameter (m)	3.54	2.65	2.4	2.65	2.65	4.5	4.65
Ballistic Coeff. (kg/m^2)	63	63	60	89	64	121	365
Entry Velocity (m/s)	4610	7260	6900	5700	5790	5601	7150
Peak Heat Rate (W/cm^2)	21	106	80	41	47	179	372
Heat Load (J/cm^2)	1100	3865	4322	3687	2827	5013	24,200
Peak Decel. (Earth g's)	7.24	11	12	6.2		12.7	5.2
L/D	0.18	--	--	--	--	0.24	0.24
G&C	3-Axis	Spin	Spin	Spin	Spin	3-Axis	3-Axis
Aeroshell Packing Density (kg/m^3)	140.6	178.3	194	248.5	164	287.3	338.2

Table 2: Comparison of MASS to Other Aerocapture Studies

Parameter	Titan Study	Neptune Study	Venus Study	MSP-01	MASS
Entry Mass (kg)	1026	1834	1087.7	554	8279
Payload Mass (kg)	600	949	788.2	347	7087
Payload/Entry Mass Fraction	58.5%	51.7%	72.5%	62.6%	85.6%
Diameter (m)	3.75	--	2.65	2.4	4.65
Ballistic Coeff. (kg/m^2)	90	895	114	63.4	365
Entry Velocity (m/s)	6500	29,000	11,250	6520	7150
Peak Heat Rate (W/cm^2)	280	12,000	1200	68	372
Heat Load (J/cm^2)	33,000	3 x 10^9	15,900	9800	24,200
Peak Decel. (Earth g's)	3.5	22	15.3	4.4	5.2
L/D	0.25	0.8	0.25	0.18	0.24
GNC Algorithm	HYPAS	HYPAS	HYPAS	HYPAS	HYPAS
Theoretical Corridor Width (degrees)	3.5	2.27	1.55	--	2.42
Drag Pass Duration (minutes)		1834	1087.7	554	8279
Aeroshell Packing Density (kg/m^3)		949	788.2	347	7087

Table 3: Comparison of MASS with an All-Propulsive MOI

	MASS	All-Propulsive
Total Mission Duration	1.77 years	1.77 years
ERV Delta-V	3787 m/s	3787 m/s
Prop Module Delta-V	1729 m/s	3881 m/s
Cruise Stage Delta-V	60 m/s	0 m/s
Total Delta-V	**5576 m/s**	**7668 m/s**
ERV (+EEV) - Dry	882 kg	882 kg
Prop Module – Dry	1135 kg	3959 kg
Aerocapture – Dry	1247 kg	0 kg
Cruise Stage – Dry	502 kg	0 kg
Sub-total – Dry	**3766 kg**	**4841 kg**
ERV Propellant	2120 kg	2120 kg
Prop Module Propellant	2950 kg	17,550 kg
Cruise Stage Propellant	260 kg	0 kg
Sub-Total Propellant Mass	**5330 kg**	**19,870 kg**
Total Launch Mass	**9096 kg**	**24,711 kg**

Table 4: Sampling of MSR Aerocapture Architectures available in 2013/2016

	"Slow" 2013 / ERV	"Fast" 2013 /ERV	"Medium" 2016 /ERV
Earth Depart Trajectory			
Launch Date	Dec 2013	Dec 2013	Aug 24 2016
Launch Vehicle	Atlas V 521	Delta IV-4050H-19	Atlas V 531
Launch C_3	13.7 km^2/s^2	10.3 km^2/s^2	23.5 km^2/s^2
Mars Arrival Vinf	6.3 km/s	4.7 km/s	6.1 km/s
Earth Return Trajectory			
Mars Departure C_3	11.1 km^2/s^2	29.8 km^2/s^2	6.5 km^2/s^2
Deep Space DV	None	1.2 km/s	None
Trajectory	Ballistic	VGA on Earth Return	Ballistic
Arrival Vinf	4.0 km/s	3.2 km/s	3.7 km/s
Total Orbiter DV	3.1 km/s	5.6 km/s	2.7 km/s
Mission Duration	32 months	21.5 months	27 months
Earth to Mars	*10 months*	*6.5 months*	*18 months*
At Mars	*9 months*	*3 months*	*1.5 months*
Mars to Earth	*13 months*	*12 months*	*6.5 months*
Spacecraft Configuration	2 Stages	3 Stages	2 stages
Stage 1	Aeroshell Stage	Aeroshell Stage	Aeroshell stage
Stage 2	ERV Stage	Propulsion Stage	ERV stage
Stage 3		ERV Stage	
Notes		Negative Launch Mass Margin: -550 kg	About 200 kg propellant saved relative to "slow" 2013 option

Table 5: MSR "Fast" Aerocapture Options from 2013 to 2025

Trajectory No.	Mars Departure Date	Earth Arrival Date	Flight Time (days)	Viable for MSR?
1	9/30/2014	10/4/2015	368.7	Yes; Baseline Trajectory
2	7/2/2015	2/25/2017	604.5	No; Return flight time too long
3	7/26/2016	6/18/2017	327.4	No; Stay time <45 days
4	5/1/2017	2/25/2019	644.6	No; Return flight time too long
5	5/22/2018	6/13/2019	386.5	No; Bad arrival phasing
6	2/27/2019	1/8/2021	680.4	No; Return flight time too long
7	4/5/2020	4/2/2022	727.7	No; Return flight time too long
8	1/6/2021	1/21/2022	379.8	No; Mars depart C3 too high
8(b)	2/3/2021	2/3/2022	365	No; Mars depart C3 too high
9	12/28/2021	7/18/2023	566.5	No; Return flight time too long
10	10/26/2022	12/6/2023	405.4	No; Bad arrival phasing
11	10/20/2023	6/8/2025	597.1	No; Return flight time too long
12	8/30/2024	12/27/2025	484.1	No; Outbound flight time too long
13	8/19/2025	6/8/2027	657.2	No; Return flight time too long

Table 6: Mars Sample Return Orbiter/ERV Maneuver List

Maneuver	DV Requirement	Propellant Mass Requirement
Mars Arrival Maneuvers		
Trajectory Correction	60 m/s	
Aerocapture RCS		5 kg
Circularize, Clean up, and Rendezvous with OS	420 m/s	
Mars Departure Maneuvers		
Apocenter Raise Maneuver 1	664 m/s	
Apocenter Raise Maneuver 2	635 m/s	
Pericenter Lowering Maneuver	10 m/s	
Attitude Control Maneuvers		20 kg
Trans-Earth Injection Maneuver and Cleanup	2527 m/s	
Post-Mars Departure Maneuvers		
Deep Space Maneuver	1200 m/s	
Earth Entry Targeting	30 m/s	
Post-EEV Release Deflection Maneuver	30 m/s	
Total	**5576 m/s**	

Table 7: Example auxiliary profile data (TES), for use in Mars-GRAM simulations

(Data used as a substitute for conventional Ames MGCM climatology. These data were averaged from 17 TES limb-sounding profiles, obtained from TES mapping year 1, near $L_s = 78°$, and local time = 14 hrs. Wind values of 0.0 mean that winds were not observed, so default values from conventional MGCM climatology values are used.)

Height (km)	Lat (deg)	LonE (deg)	Temp (K)	Pressure (Pa)	Density (kg/m^3)	Uwind (m/s)	Vwind (m/s)
2.172	67.5	223.1	209.39	4.75E+02	1.19E-02	0.0	0.0
4.825	67.5	223.1	203.59	3.70E+02	9.51E-03	0.0	0.0
7.408	67.5	223.1	197.79	2.88E+02	7.62E-03	0.0	0.0
9.921	67.5	223.1	192.08	2.24E+02	6.11E-03	0.0	0.0
12.365	67.5	223.1	186.63	1.75E+02	4.90E-03	0.0	0.0
14.744	67.5	223.1	181.46	1.36E+02	3.93E-03	0.0	0.0
17.062	67.5	223.1	176.77	1.06E+02	3.14E-03	0.0	0.0
19.326	67.5	223.1	172.53	8.26E+01	2.50E-03	0.0	0.0
21.54	67.5	223.1	168.64	6.43E+01	2.00E-03	0.0	0.0
23.709	67.5	223.1	165.22	5.01E+01	1.59E-03	0.0	0.0
25.838	67.5	223.1	162.06	3.90E+01	1.26E-03	0.0	0.0
27.931	67.5	223.1	159.2	3.04E+01	9.98E-04	0.0	0.0
29.992	67.5	223.1	156.83	2.37E+01	7.89E-04	0.0	0.0
32.029	67.5	223.1	155.03	1.84E+01	6.22E-04	0.0	0.0
34.048	67.5	223.1	153.86	1.44E+01	4.88E-04	0.0	0.0
36.057	67.5	223.1	153.15	1.12E+01	3.82E-04	0.0	0.0
38.061	67.5	223.1	152.5	8.70E+00	2.99E-04	0.0	0.0
40.051	67.5	223.1	151.68	6.78E+00	2.34E-04	0.0	0.0
42.039	67.5	223.1	150.77	5.28E+00	1.84E-04	0.0	0.0
44.019	67.5	223.1	149.83	4.11E+00	1.44E-04	0.0	0.0
45.987	67.5	223.1	148.78	3.20E+00	1.13E-04	0.0	0.0
47.948	67.5	223.1	147.71	2.49E+00	8.85E-05	0.0	0.0
49.888	67.5	223.1	146.72	1.94E+00	6.95E-05	0.0	0.0
51.825	67.5	223.1	145.76	1.51E+00	5.45E-05	0.0	0.0
53.72	67.5	223.1	144.75	1.18E+00	4.29E-05	0.0	0.0
55.646	67.5	223.1	143.68	9.17E-01	3.36E-05	0.0	0.0
57.546	67.5	223.1	142.68	7.14E-01	2.64E-05	0.0	0.0

Table 8: Monte Carlo Uncertainties for 300 kg/m^2 Ballistic Coefficient

Category	Variable	Nominal	±3σ or min/max	Distribution
Initial Conditions	Flight path angle	-12.731°	± 0.35	Gaussian
Aerodynamics	C_L (lift force) multiplier	1.0	± 10%	Gaussian
	C_D (drag force) multiplier	1.0	± 10%	Gaussian
Atmosphere	Perturbation seed	1	1:29999	Integer
	Dust tau	0.45	0.1:0.9	Uniform
Mass Properites	Mass	7285 kg	± 25	Normal

Table 9: Monte Carlo Results Summary: 300 kg/m^2 Ballistic Coefficient

Category	Mean	Std. Dev.	Max	Min
Apoapsis Altitude (km)	504.5	8.8	527.8	448.1
Periapsis Altitude (km)	-21.5	13.7	17.9	-62.8
Post Aerocapture ΔV (m/s)	122.8	3.4	140.3	115.7
Peak Laminar Heat Rate (W/cm^2)	120.7	3.8	134.6	108.6
Laminar Heat Load (J/cm^2)	12023.5	363.9	13064.5	10779.6
Deceleration Load (g)	4.3	0.3	5.6	3.6
Peak Turbulent Heat Rate (W/cm^2)	275.5	15.1	331.3	231.4
Turbulent Heat Load (J/cm^2)	19003.0	595.9	21260.5	17124.6

Table 10: Monte Carlo Uncertainties for 200 kg/m² Ballistic Coefficient

Category	Variable	Nominal	±3σ or min/max	Distribution
Initial Conditions	Flight path angle	-12.497°	± 0.35	Gaussian
Aerodynamics	C_L (lift force) multiplier	1.0	± 10%	Gaussian
	C_D (drag force) multiplier	1.0	± 10%	Gaussian
Atmosphere	Perturbation seed	1	1:29999	Integer
	Dust tau	0.45	0.1:0.9	Uniform
Mass Properites	Mass	7285 kg	± 25	Normal

Table 11: Monte Carlo Results Summary: 200 kg/m² Ballistic Coefficient

Category	Mean	Std. Dev.	Max	Min
Apoapsis Altitude (km)	510.5	4.8	542.9	491.4
Periapsis Altitude (km)	0.5	10.7	31.8	-44.8
Post Aerocapture ΔV (m/s)	117.7	2.1	127.2	112.5
Peak Laminar Heat Rate (W/cm²)	99.2	3.2	110.6	87.5
Laminar Heat Load (J/cm²)	9947.6	326.2	10892.2	8822.8
Deceleration Load (g)	4.3	0.4	5.6	3.5
Peak Turbulent Heat Rate (W/cm²)	198.8	11.2	240.6	160.8
Turbulent Heat Load (J/cm²)	13674.5	435.6	15321.9	12377.0

Table 12: Candidate TPS materials: Low-Moderate Density TPS

	PICA	TUFROC	SRAM-20 (ARA)	PhenCarb 20 (ARA)
Density	0.24 gm/cm^3	Varies with layer sizing	0.32 gm/cm^3	0.32 gm/cm^3
Description	Low density carbon fiberform partially filled with phenolic resin	Multilayer composite. Carbon fiberform/AETB tile with high emissivity, high temperature coating	Low density cork silicone composite fabricated with strip bonding technique	Low-moderate density phenolic composite fabricated with strip bonding technique
Optical Properties				
Solar Absorptance	TBD	Approx. 0.9	Approx. 0.5	Approx. 0.5
Total Hemi. Emittance	Approx. 0.8	Approx. 0.9	Approx. 0.78	Approx. 0.78
Performance Limits	Ablative No recession in non-oxidizing atmosphere at heat rate <1000 W/cm². Excellent low density ablator, but not best insulator	Non-ablative May be usable to heat rate up to 300 W/cm². Has to be fabricated as a tile.	Ablative No (little) recession at heat rate < 100 W/cm². Differential recession between composite and interface strips may cause boundary layer transition	Ablative No recession in non-oxidizing environment. Differential recession between composite and interface strips may cause boundary layer transition
Uncertainties	Low density, porous material. In-depth radiant transmission may be important	Heat flux limit currently uncertain. Spectral emittance data on coating shows very high emittance at CN violet wavelengths. Will absorb (not transmit) radiation	Low density, porous material. In-depth radiant transmission may be important	Higher density and higher char yield of phenolics may mitigate in-depth radiant absorption at the penalty of higher thermal conductivity.

Table 13: PICA TPS Mass & Thickness - With Margin (Baseline TPS)

Parameter	Thickness (cm)	Mass (kg)
FOREBODY TPS (PICA-15) MASS & THICKNESS		
Unmargined TPS (maintains bond line below 250 C) NOTE: Found using areal density and TPS mid-thickness surface area.	4.724	231.8 (ρ_{areal} = 11.66 kg/m^2)
30% Contingency (50 C bondline margin plus manufacturing, etc.)	+1.417	+69.5
TPS Recession Factor of Safety (50% of recession - 2.032 cm of recession)	+1.016	+46 kg
Final Forebody TPS Thickness & Mass (with 30% Contingency and 50% Recession Factor of Safety) NOTE: Mass calculated using TPS mid-thickeness surface area	7.158	347.3
AFTERBODY TPS (SLA-561V) MASS & THICKNESS		
Unmargined TPS (maintains bond line below 250 C) NOTE: Found using areal density and TPS OML surface area	1.98	145.75 kg (ρ_{areal} = 5.06 kg/m^2)
30% Contingency (50 C bondline margin plus manufacturing, etc.)	+0.594	+43.7
TPS Factor of Safety (10% of unmargined thickness)	+0.198	+14.58
Final Aftbody TPS Thickness & Mass (with 30% Contingency and 10% Factor of Safety) NOTE: Mass calculated using OML surface area.	2.772	204.1

Table 14: SRAM-20 TPS Mass and Thickness –With Margin (Alternative TPS)

Parameter	Thickness (cm)	Mass (kg)
FOREBODY TPS (SRAM-20) MASS & THICKNESS		
Unmargined TPS (maintains bond line below 250 C) NOTE: Found using areal density and TPS mid-thickness surface area.	1.778	113.1 (ρ_{areal} = 5.69 kg/m^2)
30% Contingency (50 C bondline margin plus manufacturing, etc.)	+0.53	+33.7
TPS Recession Factor of Safety (50% of recession – 0.58 cm of recession)	+0.29	+18.5 kg
Final Forebody TPS Thickness & Mass (with 30% Contingency and 50% Recession Factor of Safety) NOTE: Mass calculated using TPS mid-thickeness surface area	2.598	165.3

Table 15: Carbon-Carbon TPS Mass - (Alternative)

Component	Mass with Contingency (kg)
Stiffened carbon-carbon shell	239 kg
TPS – Carbon-Carbon portion	36 kg
TPS – Calcarb	138 kg
High Temperature Blankets	113 kg
Carbon-Carbon Total	**526 kg**

Table 16: Forebody TPS Material Comparisons – Mass Only

Component	Baseline PICA	Alternative - Carbon-Carbon Hot Structure	Alternative – SRAM-20
Aeroshell Forebody Structure	273 kg	239 kg	273 kg
TPS	347 kg		165 kg
Insulation		287 kg	
Total Mass with Contingency	**620 kg**	**526 kg**	**438 kg**
Difference from Baseline	**--**	**-94 kg**	**-182 kg**

Table 17: Payload Structure Mass Summary

Item	Structure Mass (kg)	Est. fitting mass (kg)	Total Mass (kg)
Lower truss	140	48	188
Lower ring	40	8	48
Mid truss	194	48	242
Mid ring	89	8	97
Upper truss	155	48	203
Upper ring	17	4	21
TOTAL MASS			**799**

Table 18: Aeroshell Structure Mass

Item	Primary Structure mass (kg)	CBE TPS mass (kg)	TCS, harness mass (kg)	Total mass (kg)
Forebody	210.0	292.3	15.8	375.4
Backshell	155.3	145.8	14.5	215.8
Payload ring	14.7	--	--	14.7
TOTAL MASS				**605.9**

Table 19: MSR Aerocapture Mass Summary

Element	Dry Mass CBE (kg)	Dry Mass w/ Contingency (kg)	Propellant Mass (kg)	Total Wet Mass w/ Contingency (kg)
Earth Return Vehicle, Total	678	882	2120	3002
ERV, Earth Entry Vehicle		56		
ERV, Jettisoned Sample Capture Hardware		79		
ERV, Bus+Retained Sample Capture Hardware		747		
Propulsion Stage	672	874	2950	3824
Mid-Truss Stage	201	261		261
Aeroshell/Backshell	917			1247
Cruise Stage	386	502	260	762
Total Launch Mass				**9096**
	Launch Vehicle			Delta 4050H-19
	C_3 (km^2/s^2)			10.3
	Launch Vehicle Capability			7760
	Launch Vehicle Margin (kg)			-1335
	Launch Vehicle Margin (%)*			-17.2%

* %Margin= (Launch Capability – Wet Mass w/ Contingency)/ Launch Capability

Table 20: Comparison of Current Study Results to Team X Study (Ref 6)

Element	Current Study Dry Mass w/ Contingency (kg)	Propellant Mass (kg)	Total Wet Mass w/ Contingency (kg)	Team X Study Dry Mass w/ Contingency (kg)	Propellant Mass (kg)	Total Wet Mass w/ Contingency (kg)
Earth Return Vehicle, Total	882	2120	3002	843	1993	2836
ERV, Earth Entry Vehicle	*56*			*56*		
ERV, Jettisoned Sample Capture Hardware	*79*			*79*		
ERV, Bus+Retained Sample Capture Hardware	*747*			*708*		
Propulsion Stage	874	2950	3824	728	2693	3391
Mid-Truss Stage	261		261			
Aeroshell/Backshell			1247	2752		2752
Entry Mass			**8334**			**9159**
Cruise Stage	502	260	762	300	100	400
Aeroshell /Entry Mass Fraction			15.0%			30.0%
Total Launch Mass			**9096**			**9559**
Launch Vehicle			Delta 4050H-19			Delta 4050H-19
C$_3$ (km^2/s^2)			10.3			10.3
Launch Vehicle Capability			7760			7760
Launch Vehicle Margin (kg)			-1335			-1799
Launch Vehicle Margin (%)*			-17.2%			-23.2%

Table 21: MASS Summary Cost Estimate Results

Element	FY05-$M	Estimating Methodology
Phase A	**$1.0**	Standard
Phase B/C/D		
PM/SE/MA/PA	$94.1	NAFCOM
Instruments	$64.1	
Sample Cature System including Op-Nav Camera	*$44.8*	2004 Team X Report
EEV	*$19.3*	2004 Team X Report
Flight System	$221.5	
ERV	*$61.7*	NAFCOM
Prop. Stage	*$37.8*	NAFCOM
Mid-Truss Stage	*$6.8*	NAFCOM
Cruise Stage	*$41.6*	NAFCOM
Aeroshell	*$73.6*	NAFCOM
GDS/MOS	$12.0	2% on Non-Rec; 10% of Rec. H/W
Science Team	$6.6	5% on Non-Rec; 20% of Rec Instrument H/W
EPO	$4.6	AO Required 1%
Phase B/C/D Subtotal w/o Reserves	**$466.9**	
Phase B/C/D Reserves	$140.1	JPL Design Principles (30%)
Phase B/C/D Subtotal w/ Reserves	**$607.0**	
Phase B/C/D Fee	$60.7	10% Phase B/C/D Subtotal w/ Reserves
Phase B/C/D Contingency	$151.8	25% Phase B/C/D Subtotal w/ Reserves
Total Phase B/C/D	**$819.5**	
Launch Services	$288.0	MSR Orbiter
Phase E		
MO&DA	$7.0	SOCM
DSN	$3.3	$0.5M for Tracking Network + $1.5M/year
EPO	$0.1	AO Required 1%
Phase E Subtotal w/o Reserves	**$10.4**	
Phase E Reserves	$1.6	JPL Design Principles (15%)
Phase E Subtotal w/ Reserves	**$12.0**	
Phase E Fee	$1.2	10% Phase E Subtotal w/ Reserves
Phase E Contingency	$3.0	25% Phase E Subtotal w/ Reserves
Total Phase E	**$16.1**	
Total Life Cycle Cost	**$1,124.6**	

Figures
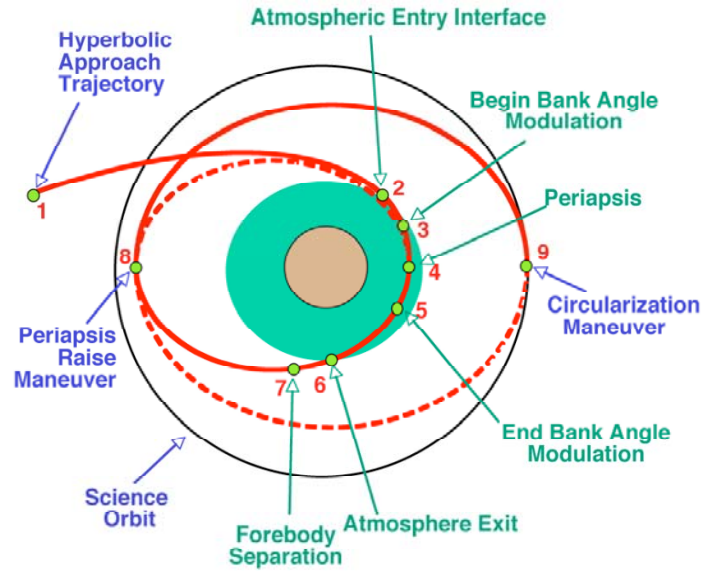
Figure 1: Aerocapture Schematic
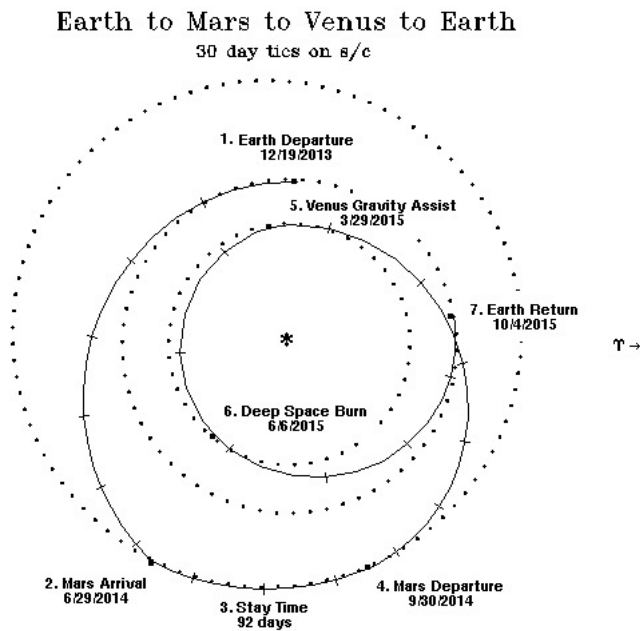
Figure 2: Baseline 2013 "Fast" Mars Sample Return Trajectory
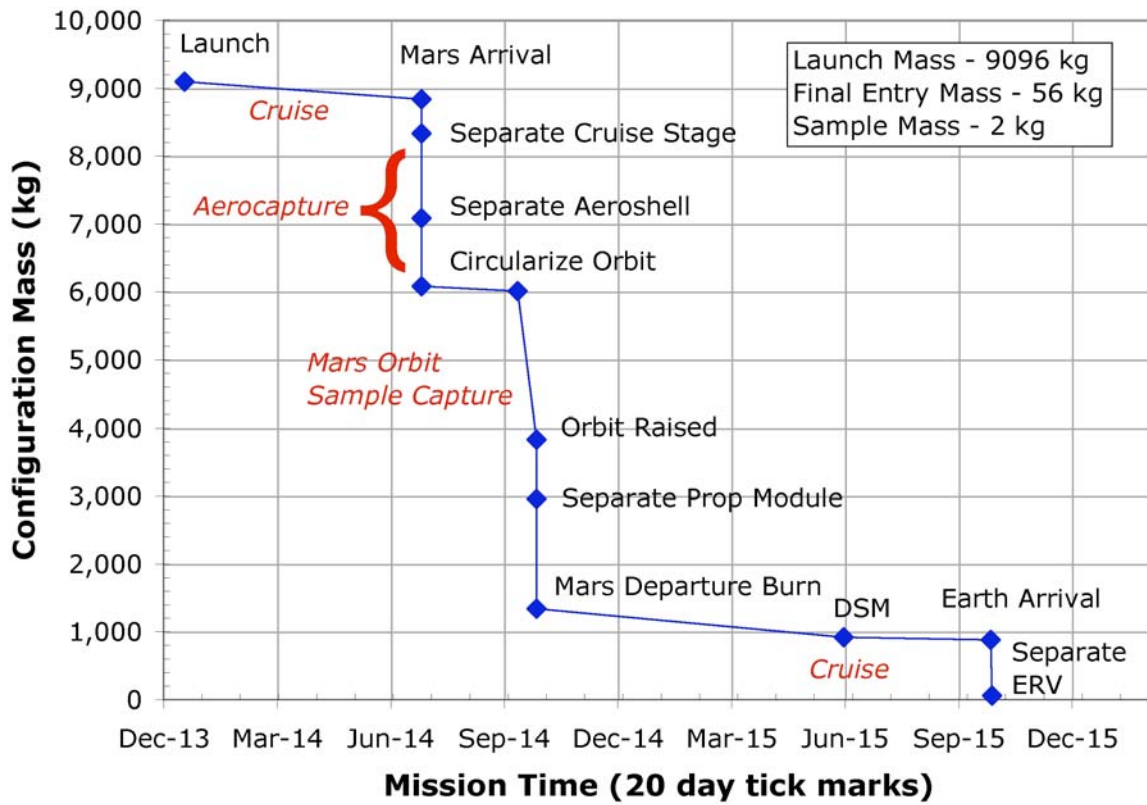
Figure 3: MASS - Mass throughout the mission
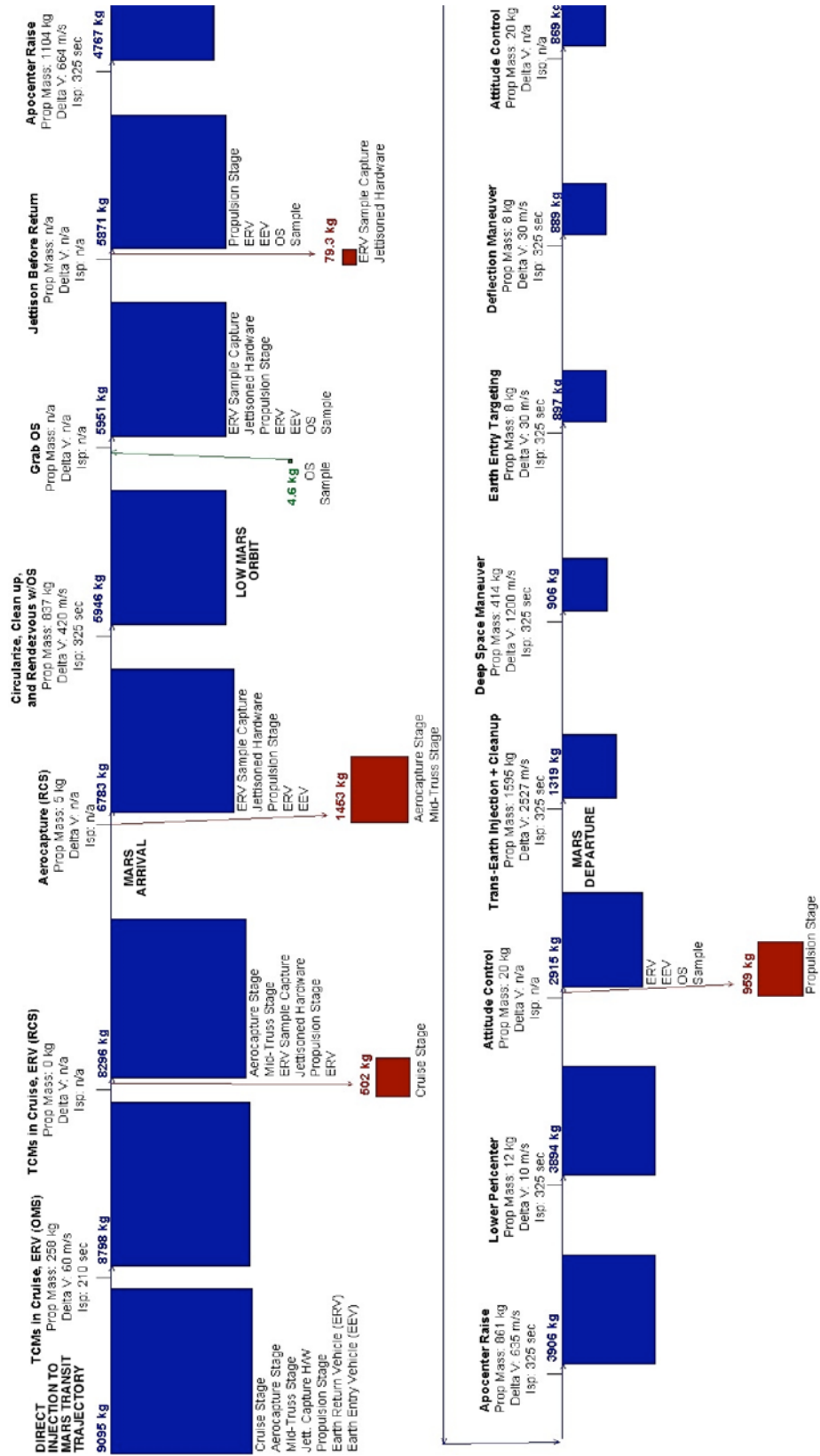
Figure 4: Mars Sample Return Mass/Maneuver History
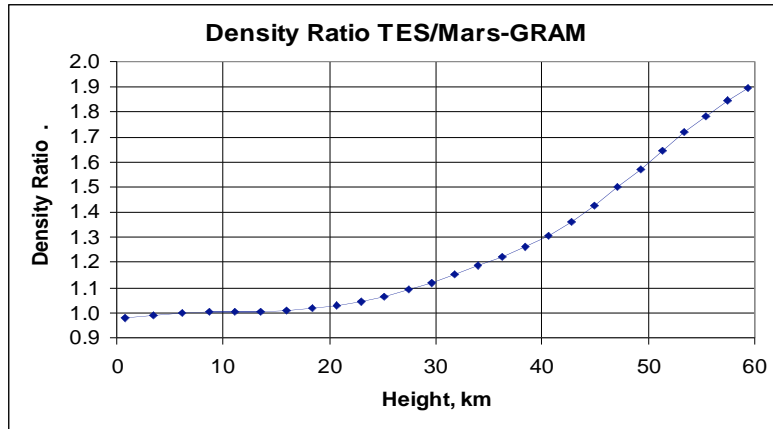
Figure 5: Ratio of atmospheric density from TES auxiliary profile to Mars-GRAM standard profile

(Data from Table 7 for TES profile compared to density from a Mars-GRAM vertical profile at the same latitude and longitude, using conventional climatology. See additional comparison results in Appendix D.)
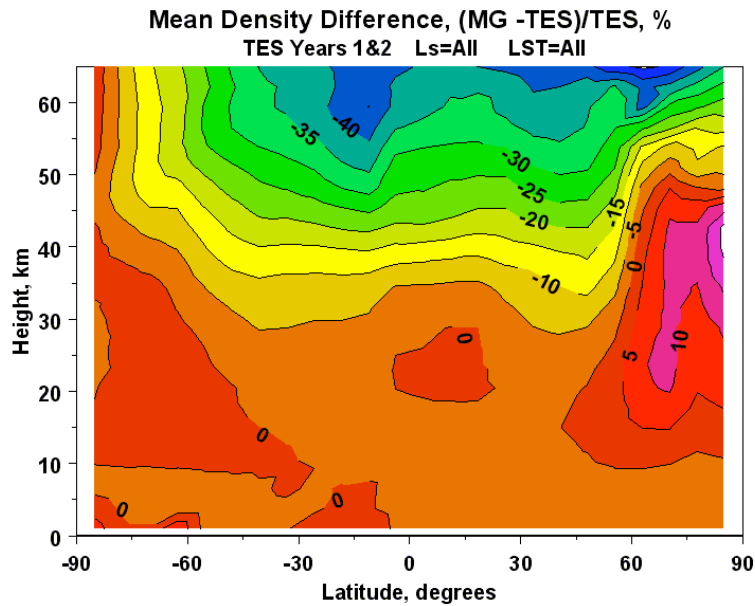
Figure 6: Mean percentage difference in density between Mars-GRAM conventional MGCM climatology and TES-observed limb sounding data.

(Results have been averaged over TES mapping years 1 and 2, for all times of year and both 2 and 14 hours local time. Negative contours mean that TES observed densities are larger than Mars-GRAM values obtained from conventional MGCM climatology.)
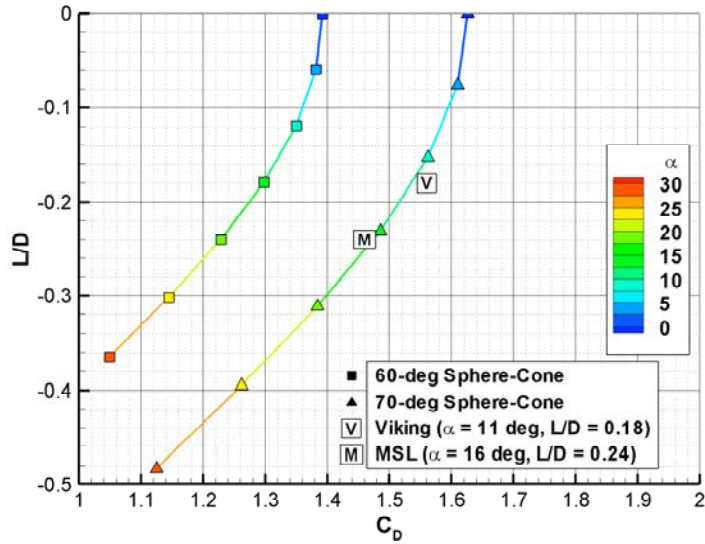
Figure 7: Modfied Newtonian L/D and C_D for 60° and 70° Sphere Cones
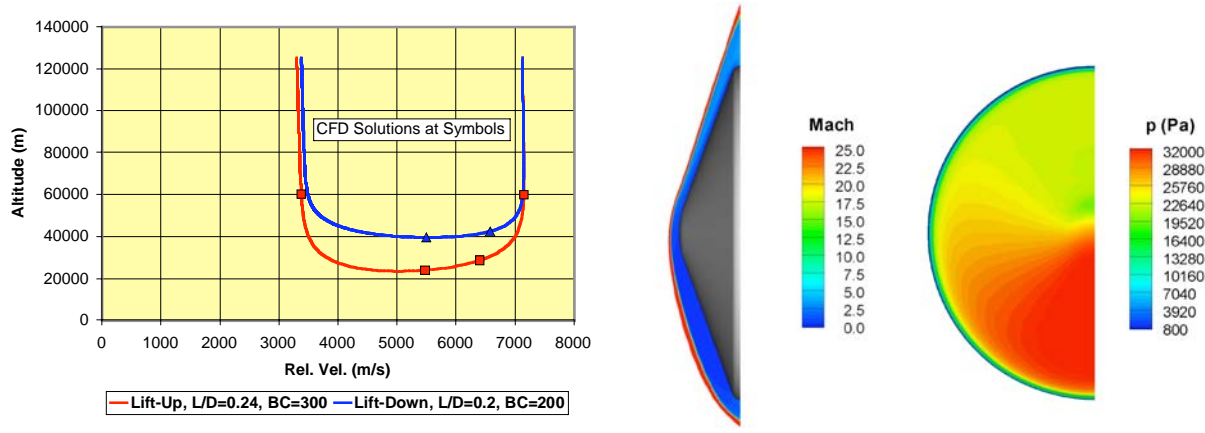
Figure 8: Aerocapture Performance Design Trajectories and CFD Solutions

Figure 9: Symmetry Plane Mach Number (left) and Surface Pressure (right) Contours at V=6406 m/s on the Lift-Up, L/D=0.24, BC=300 kg/m^2 Trajectory (α=16°)
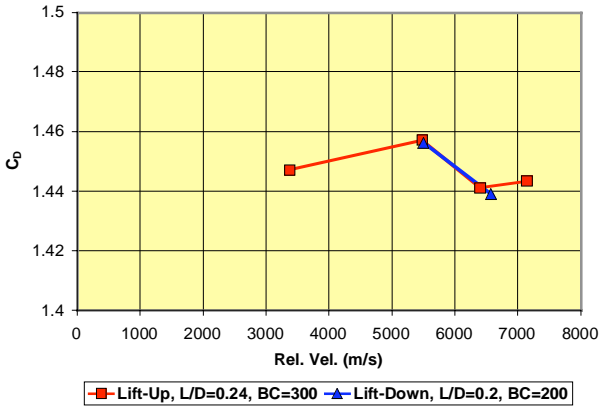
Figure 10: Aerocapture C$_D$ on the Performance Design Trajectories ($\alpha = 16°$)
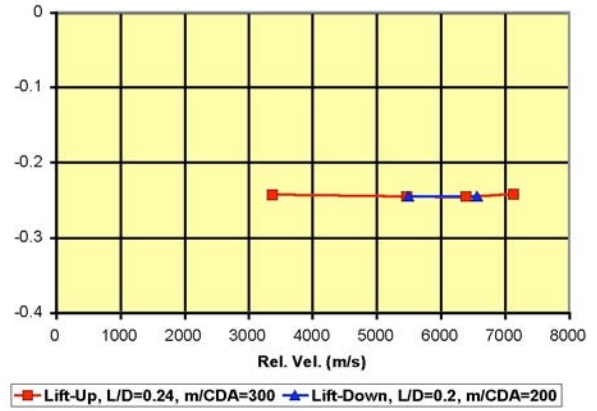
Figure 11: : Aerocapture L/D on the Performance Design Trajectories ($\alpha = 16°$)
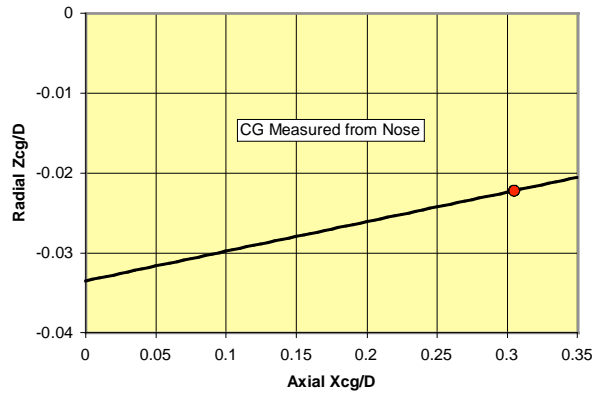
Figure 12: Axial CG Location for Trim (α=16°)
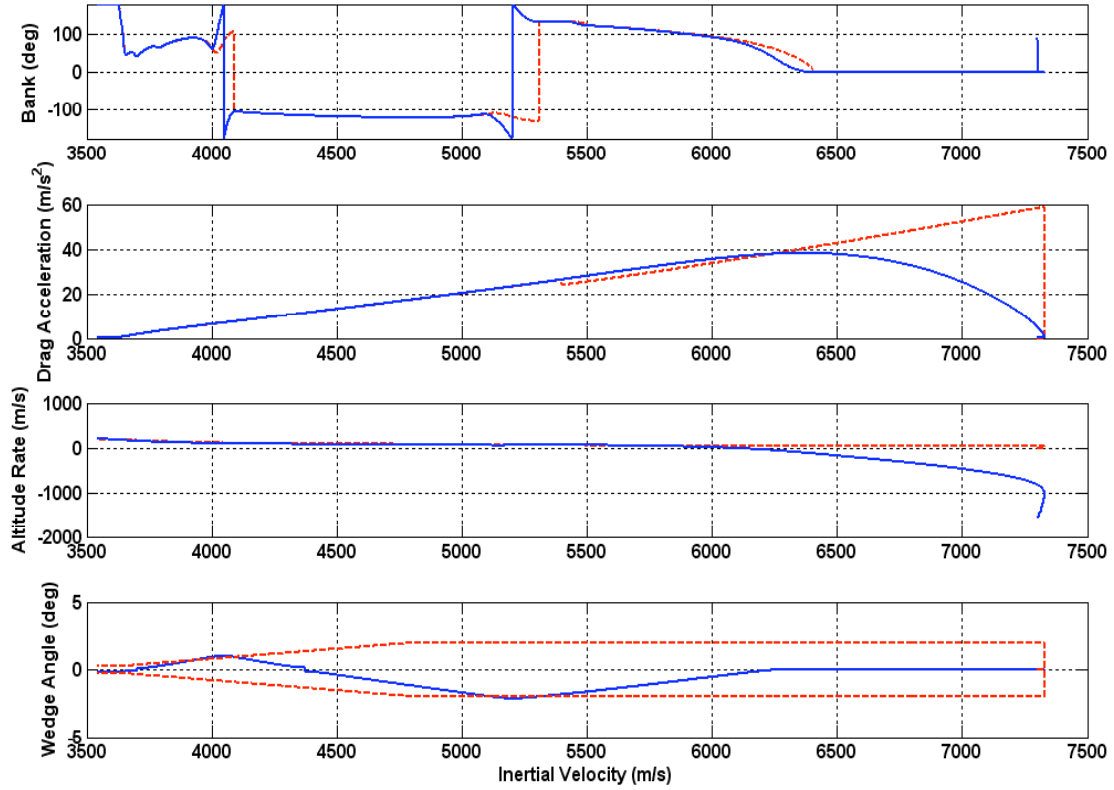
Figure 13: Nominal BC = 300 kg/m² Guidance Profile
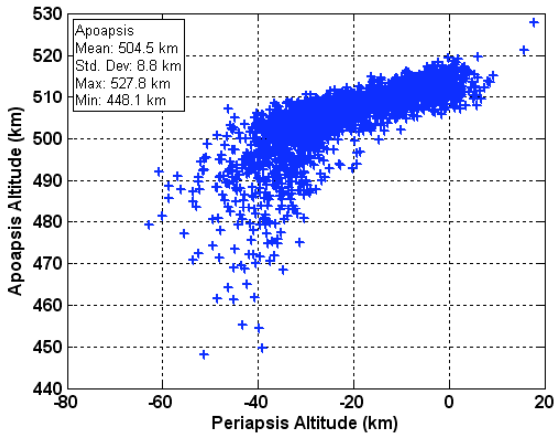
Figure 14: Apoapsis vs. Periapsis Altitude (300 kg/m²)
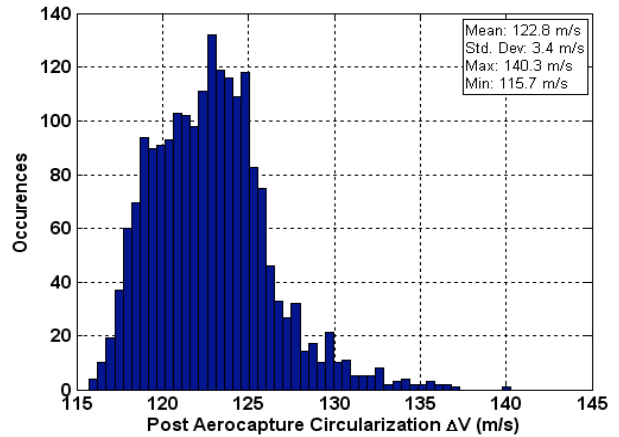
Figure 15: Post Aerocapture Circularization ΔV (300 kg/m²)
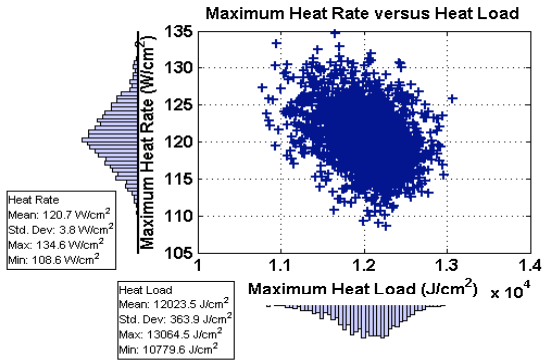
Figure 16: Maximum Laminar Heat Rate vs. Heat Load (300 kg/m^2)
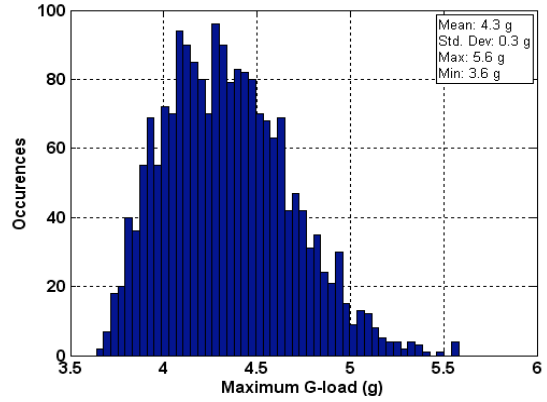
Figure 17: Maximum Deceleration (300 kg/m^2)
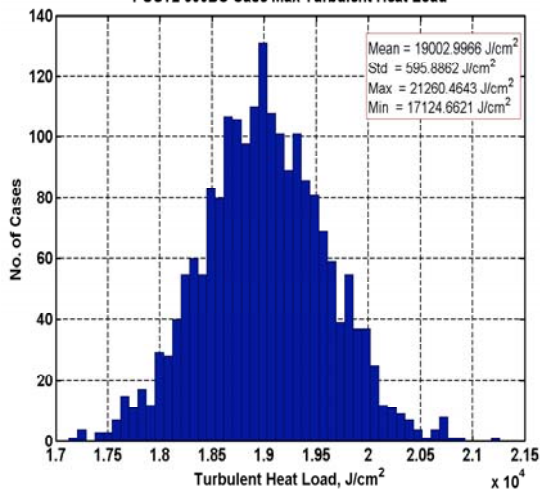
Figure 18: Maximum Turbulent Heat Load (300 kg/m^2)
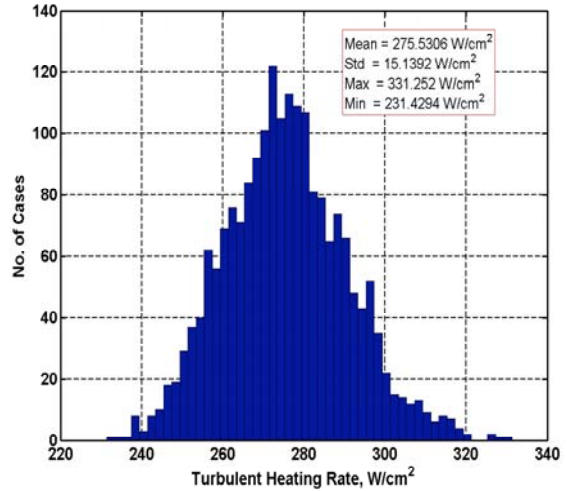
Figure 19: Maximum Turbulent Heat Rate (300 kg/m^2)
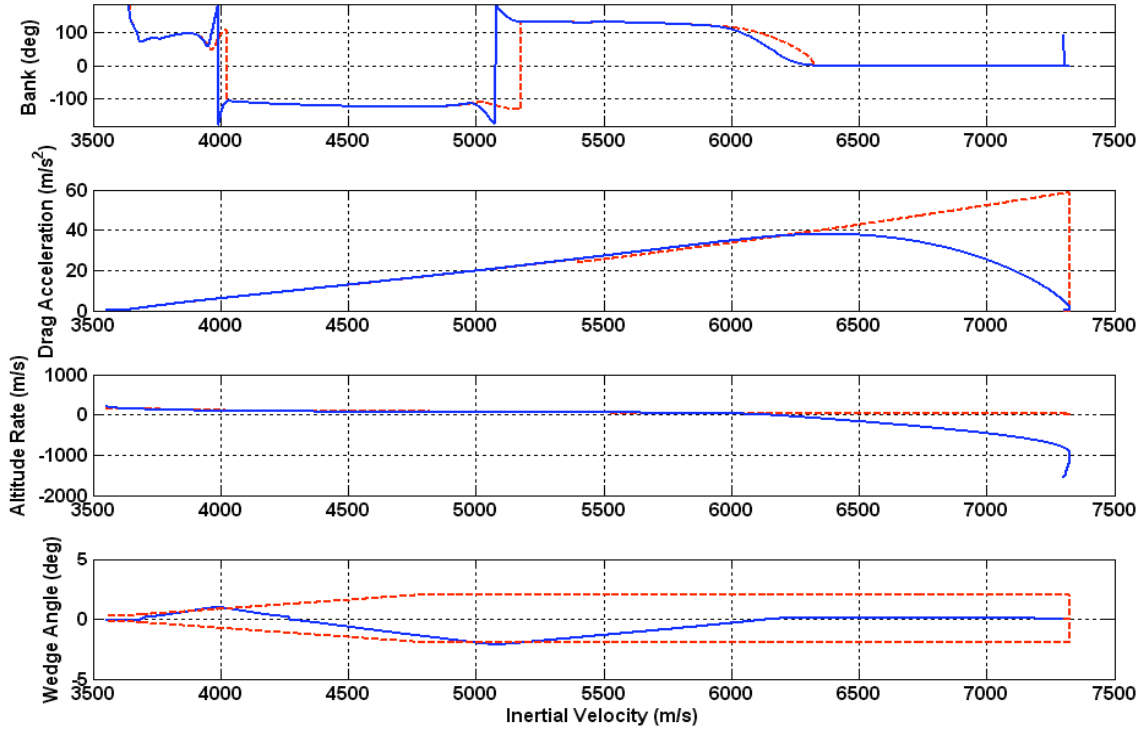
Figure 20: Nominal BC = 200 kg/m² Guidance Profile
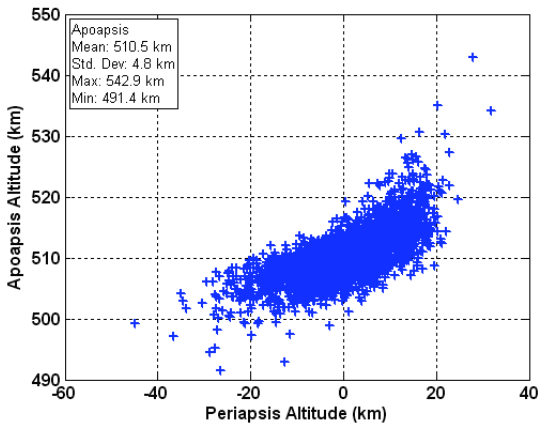
Figure 21: Apoapsis versus Periapsis Altitude (200 kg/m²)
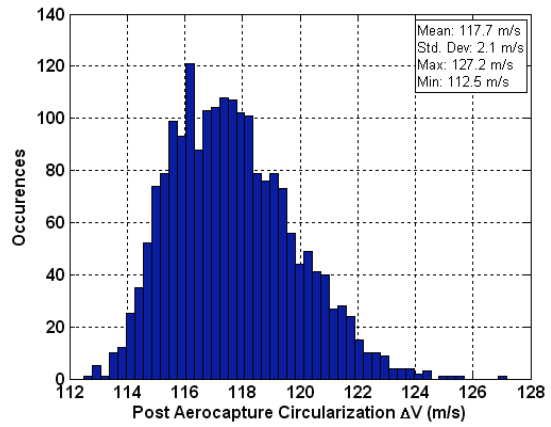
Figure 22: Post-Aerocapture ΔV (200 kg/m²)
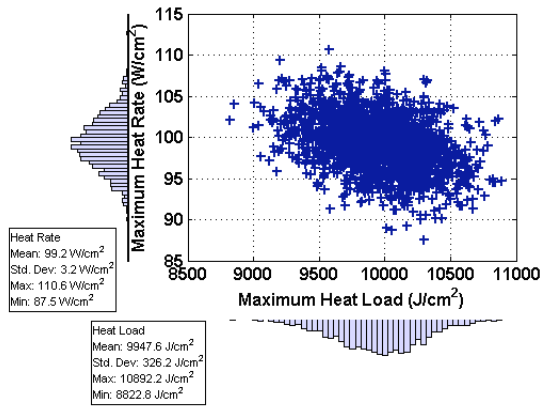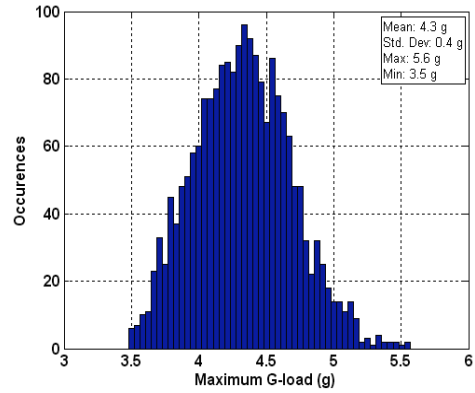
Figure 24: Maximum Laminar Heating (200 kg/m^2)

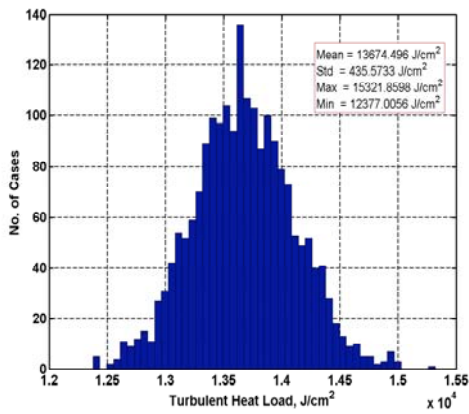**Figure 23: Maximum Deceleration (200 kg/m^2)**

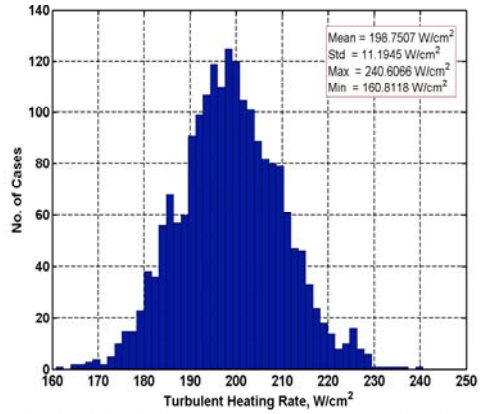**Figure 25: Maximum Turbulent Heat Load (200 kg/m^2)**

Figure 26: Maximum Turbulent Heat Rate (200 kg/m^2)
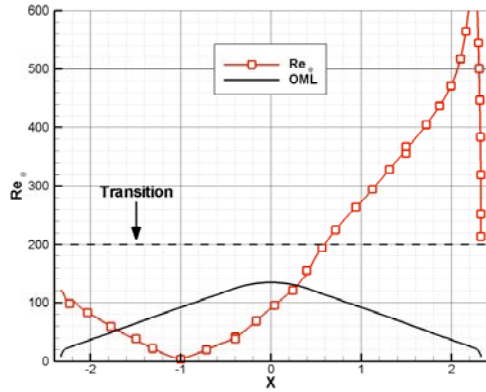
Figure 28: LAURA Laminar Forebody Re$_q$ Distribution at Peak Heating
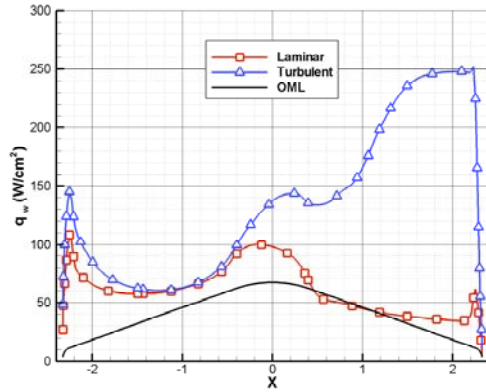

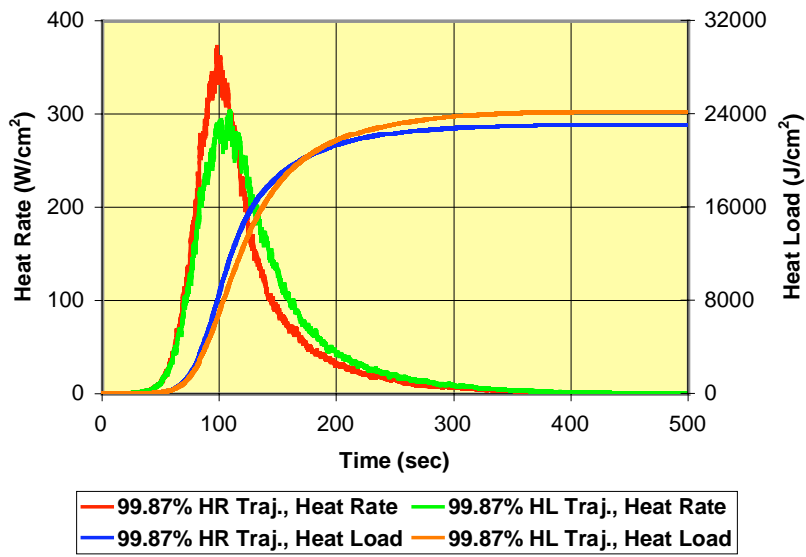**Figure 27: LAURA Laminar and Turbulent Forebody Heat Rate (No Uncertainties)**

Figure 29: Forebody Convective Heating Environments Including 50% Uncertainty
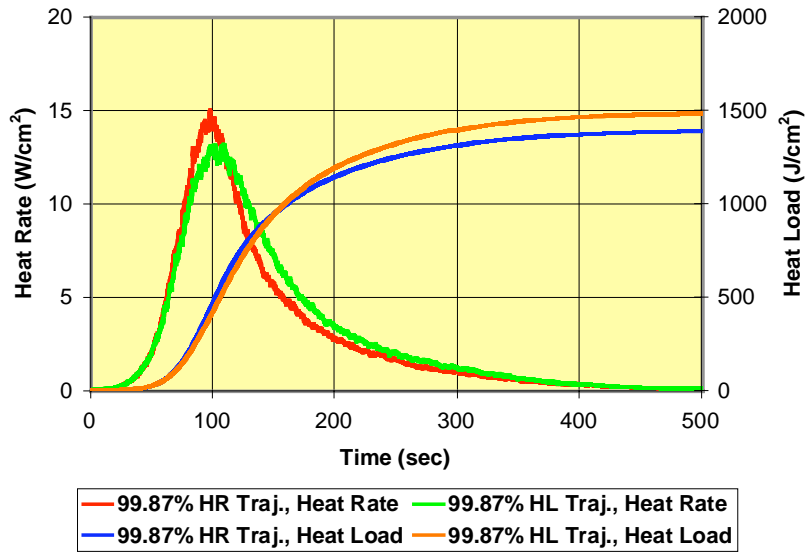
Figure 30: Afterbody Convective Heating Environments Including 200% Uncertainty
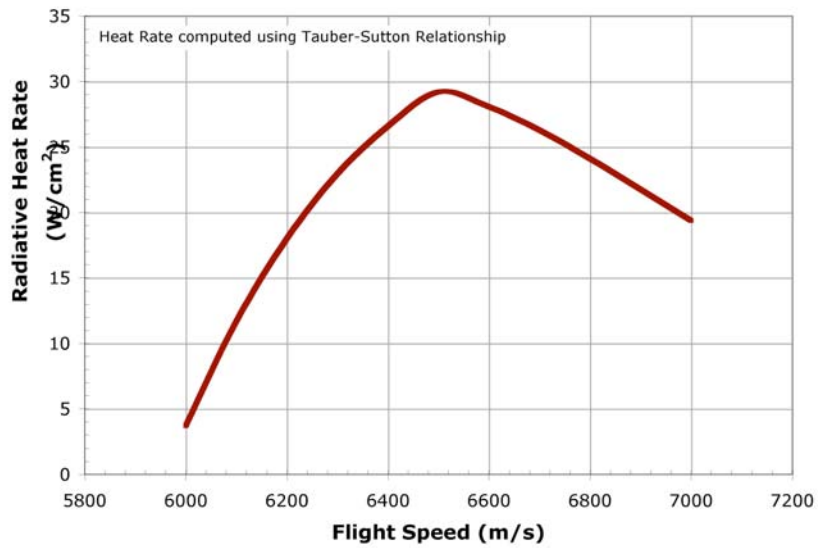
Figure 31: Radiative Heat Rate for 3σ low trajectory
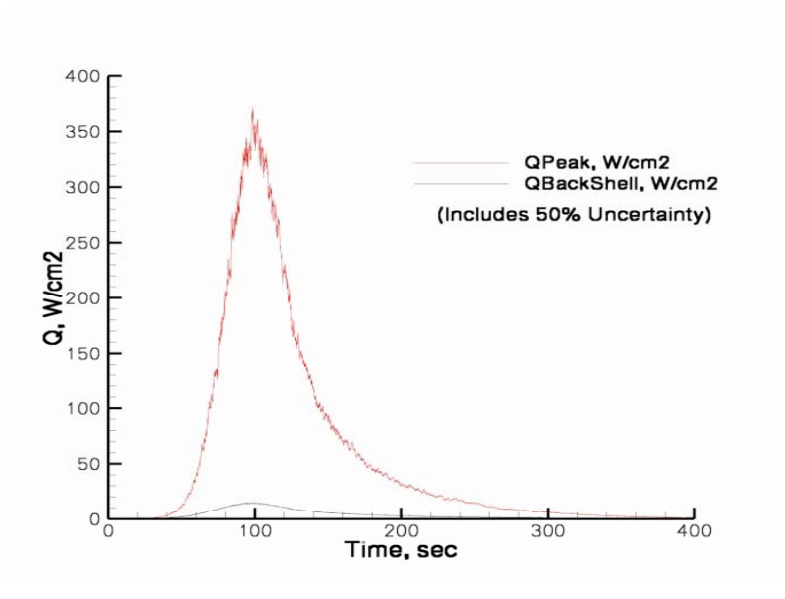
Figure 32: Heating Pulse, Mars Aero Trajectory, includes 50% Uncertainty on Turbulence Trajectory with peak heat transfer.

Source: MASS_Guided_BC300_99.87HR2.dat
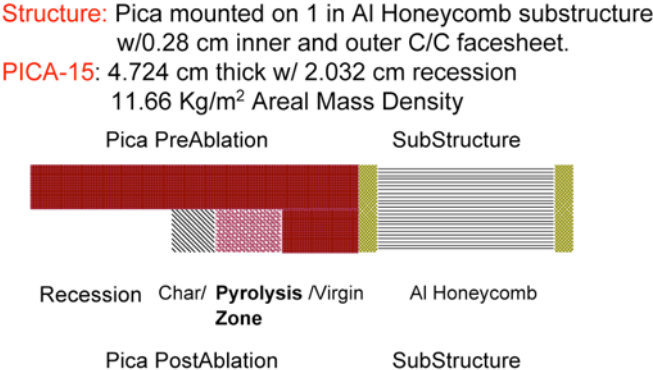
Figure 33: Baseline PICA TPS Heatshield Specifications, without margins.
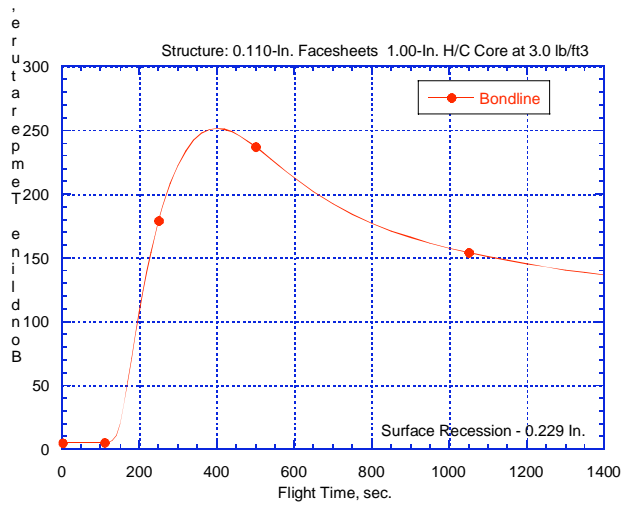
Figure 1 - MASS Analysis for 0.70-In. SRAM-20 Ablator Over 1.22-In. Composite Structure

Figure 34: Thermal response of the SRAM-20 ablative TPS
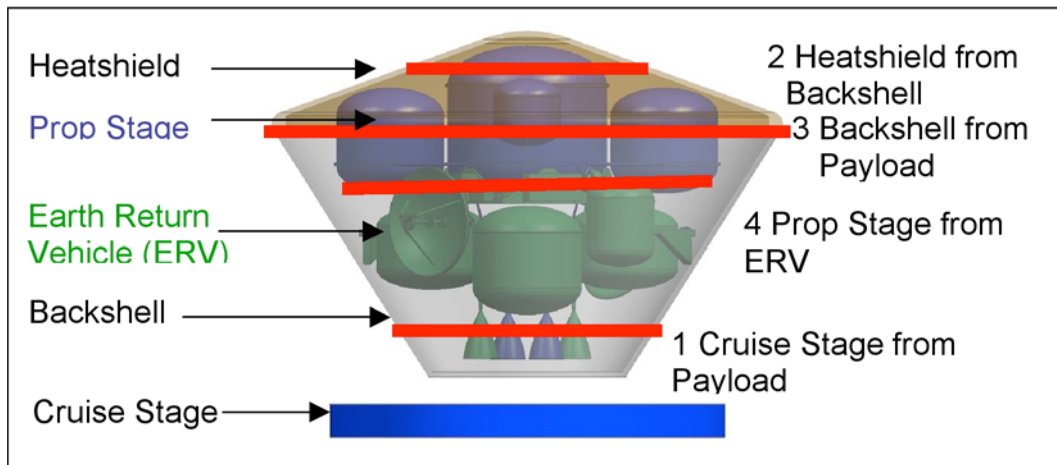
Figure 35: Spacecraft Separation Planes
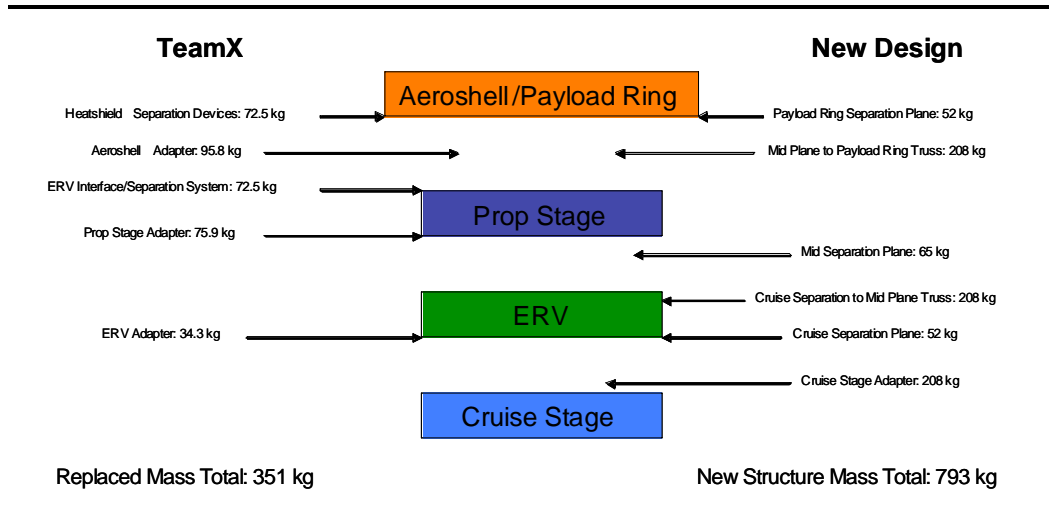
Figure 36: Comparison of the changes in the flight system mass from the initial Team X configuration.
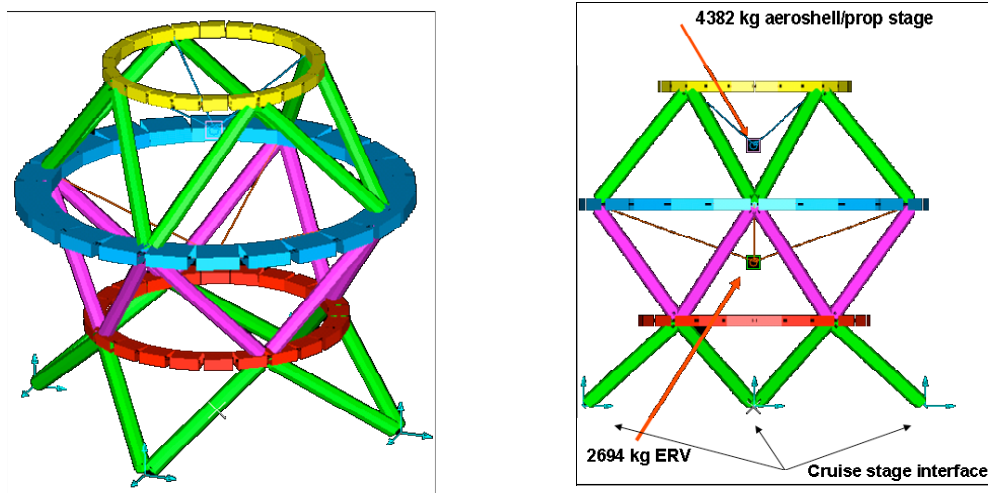
Figure 37: Finite Element Model of the Payload Structure
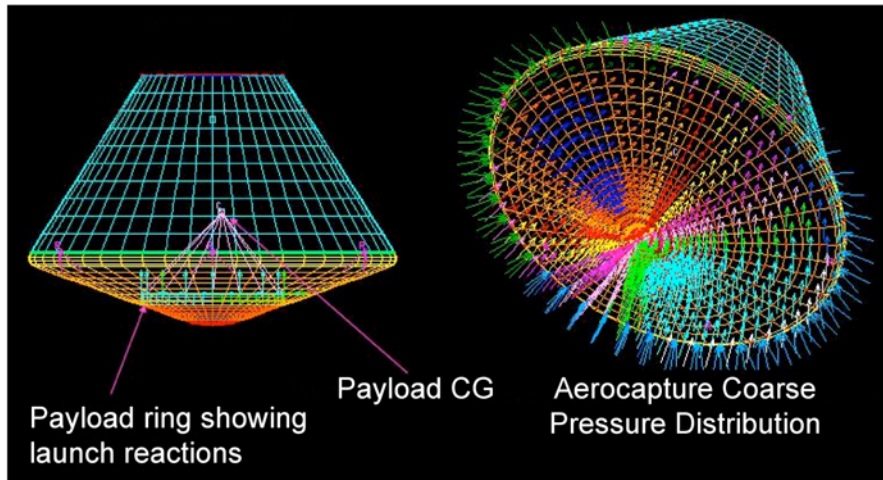
Figure 38: Aeroshell FEM with Inertial Loads (Launch) and Pressure Distribution (Aerocapture)
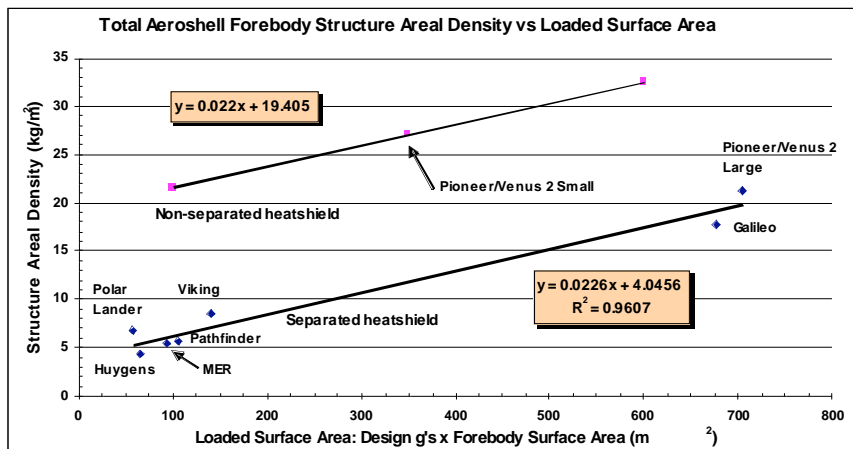
Figure 39: Sphere-Cone Aeroshell Forebody Structure Mass Trend Curves
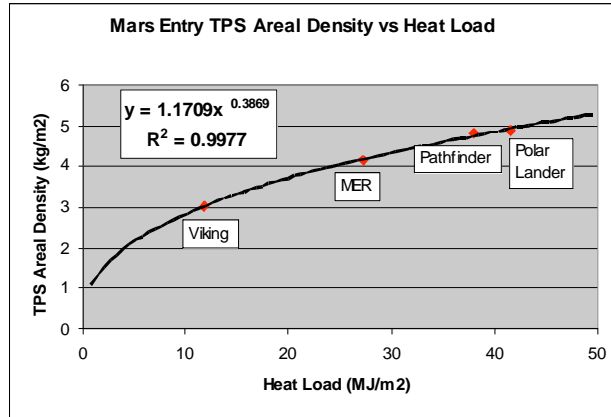
Figure 40: TPS Mass Trend Curve for Mars
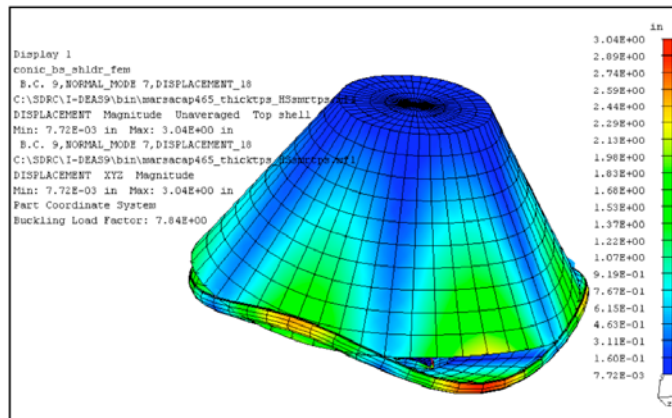
Figure 41: Aeroshell Buckling Mode Shape
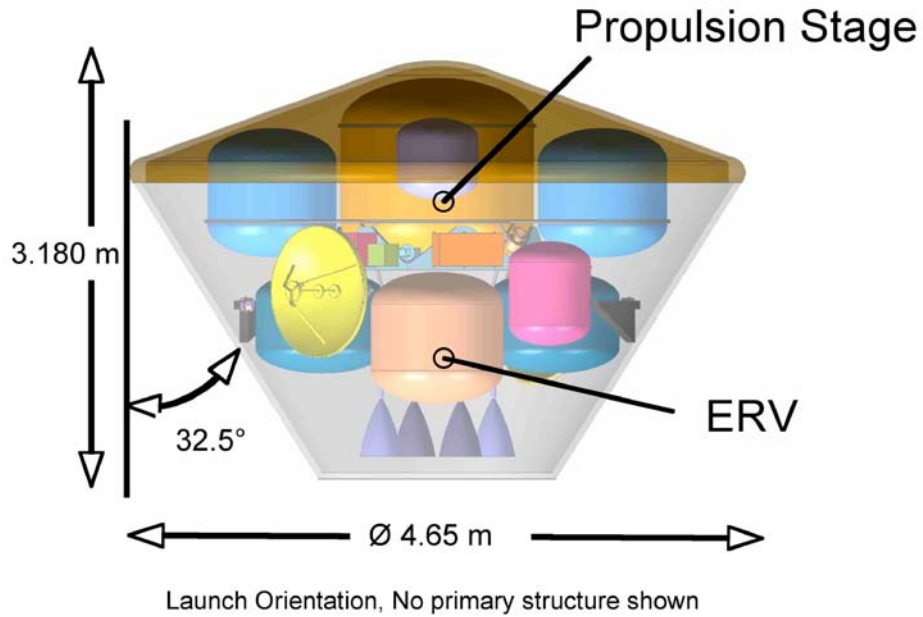
Figure 42: MSR Vehicle Configuration, no Primary Structure
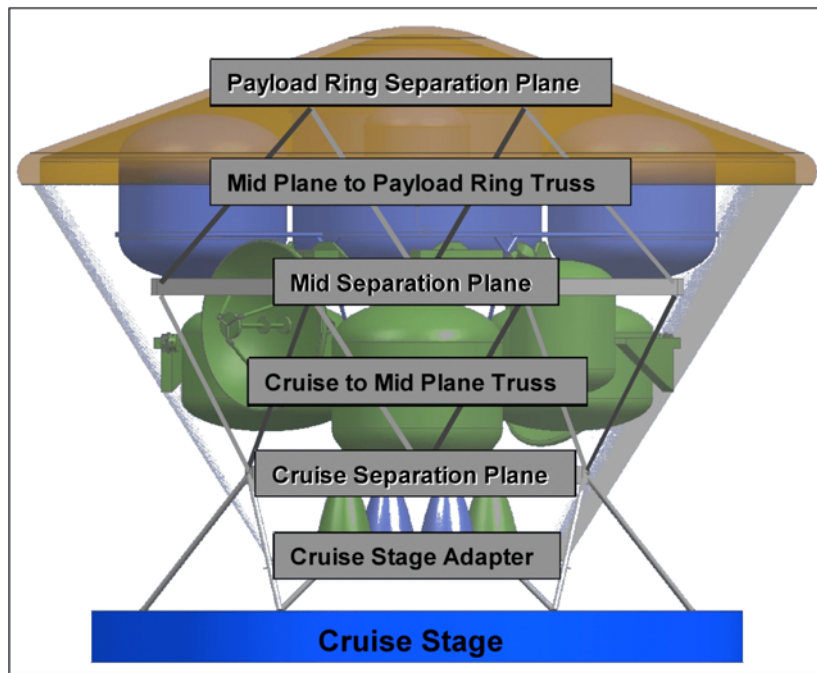
Figure 43: MSR Vehicle Configuration, w/Primary Structure.

(Primary structure within Prop Stage and ERV connects to mid-plane; mid-plane, through trusses, connects to payload ring and to cruise separation plane, avoiding pass-through loads in either vehicle.)
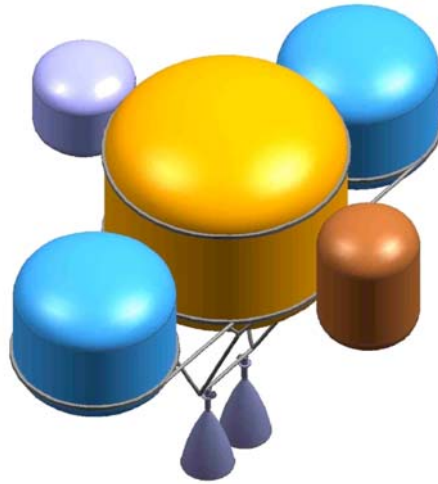
Figure 44: Propulsion Stage Configuration (Primary Structure Omitted for Clarity)
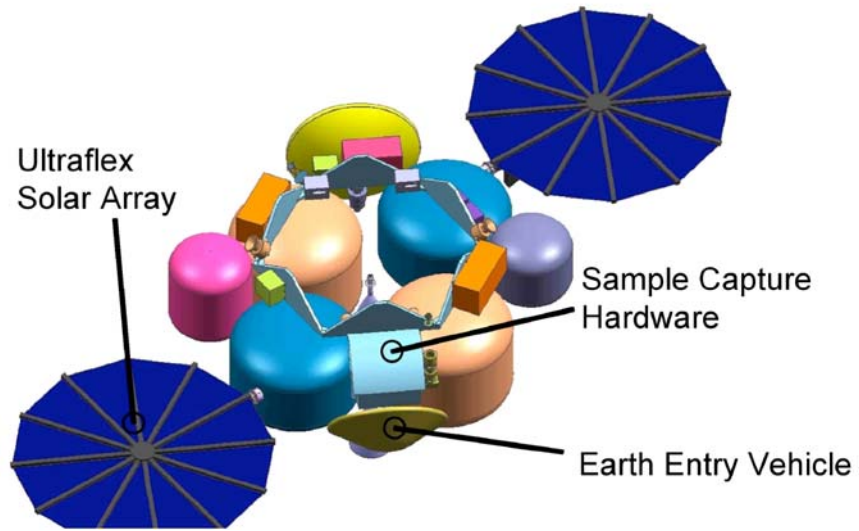
Figure 45: Earth Return Vehicle Configuration (Primary Structure Omitted for Clarity)

Appendix Tables and Figures

Table 22: APPENDIX A - Master Equipment List for Earth Return Vehicle

	Mass, CBE (kg)	Contingency	CBE + Contingency (kg)
ERV Payload	129.0	30%	167.7
Earth Entry Vehicle	43.0	30%	55.9
Sample Capture Hardware, Jettisoned	61.0	30%	79.3
Sample Capture Hardware, Retained	25.0	30%	32.5
ERV Bus	549.5	19%	653.2
Attitude Control	16.6	10%	18.3
Sun Sensors	*0.6*	*10%*	*0.6*
Star Trackers	*5.0*	*10%*	*5.5*
IMU	*1.5*	*10%*	*1.7*
HGA Drive Motors	*2.6*	*10%*	*2.9*
S/A Drive Motors	*4.0*	*10%*	*4.4*
Gimbal Drive Electronics	*3.0*	*10%*	*3.3*
Command & Data Handling	16.0	30%	20.8
PPC 750 w/L2 Cache	*1.1*	*30%*	*1.4*
NVM: 256 MB	*1.3*	*30%*	*1.7*
FPGA SIO	*1.0*	*30%*	*1.3*
GIF	*0.7*	*30%*	*0.9*
ULDL	*1.0*	*30%*	*1.3*
DTCI	*1.0*	*30%*	*1.3*
CPS	*2.7*	*30%*	*3.5*
Backplane (cPCI)	*1.7*	*30%*	*2.2*
Chassis/Enclosure/Rear Cover	*5.6*	*30%*	*7.3*
Power	60.5	30%	78.6
Solar Array	*14.0*	*30%*	*18.2*
Ni-H2 (IPV) Battery	*35.3*	*30%*	*45.9*
Array Switching Boards	*0.8*	*30%*	*1.0*
Load Switching* Boards	*0.8*	*30%*	*1.0*
Thruster Drivers Boards	*2.4*	*30%*	*3.1*
Pyro Switching Boards	*0.8*	*30%*	*1.0*
Converters* Boards	*4.8*	*30%*	*6.2*
Battery Control* Boards	*0.8*	*30%*	*1.0*
Diodes Boards	*0.8*	*30%*	*1.0*
Propulsion	138.6	26%	174.3
Gas Service Valve	*0.9*	*2%*	*0.9*
HP Latch Valve	*0.7*	*2%*	*0.7*
Solenoid Valve	*1.4*	*0%*	*1.4*
HP Transducer	*0.5*	*2%*	*0.6*
Gas Filter	*0.2*	*2%*	*0.2*
NC Pyro Valve	*0.2*	*2%*	*0.2*
Temp. Sensor	*0.0*	*2%*	*0.0*
Liq. Service Valve	*0.6*	*2%*	*0.6*
Test Service Valve	*0.5*	*2%*	*0.5*
LP Transducer	*2.2*	*2%*	*2.2*
Liq. Filter	*0.8*	*2%*	*0.8*
LP Latch Valve	*1.8*	*2%*	*1.8*
NC Pyro Valve	*1.0*	*2%*	*1.0*

	Mass, CBE (kg)	Contingency	CBE + Contingency (kg)
Mass Flow Control	*0.1*	*2%*	*0.1*
Temp. Sensor	*0.2*	*2%*	*0.2*
Lines, Fittings, Misc.	*3.5*	*30%*	*4.6*
DM Monoprop Thrusters 1	*1.6*	*5%*	*1.7*
DM Monoprop Thrusters 2	*2.7*	*10%*	*3.0*
Biprop Main Engine	*17.3*	*20%*	*20.8*
Ox Pressurant Tank	*14.0*	*30%*	*18.2*
Fuel Pressurant Tank	*29.5*	*30%*	*38.3*
Fuel Tanks	*37.5*	*30%*	*48.8*
Oxidizer Tanks	*21.4*	*30%*	*27.8*
Structures & Mechanisms	220.1	30%	286.2
Primary Structure	*144.8*	*30%*	*188.2*
Secondary Structure	*24.8*	*30%*	*32.2*
Mid Separation Plane	*21.0*	*30%*	*27.3*
EEC Interface and Release	*6.4*	*30%*	*8.4*
Solar Array Actuator(s)+Latch/Release	*5.3*	*30%*	*6.9*
Antenna Articulation Mechanism	*5.7*	*30%*	*7.4*
Integration Hardware & MHSE	*5.6*	*30%*	*7.3*
Balance Mass	*6.5*	*30%*	*8.4*
Telecon	32.0	23%	39.4
X- LGA (8dB) Cassini	*0.6*	*25%*	*0.8*
X/X 1.0m diam High Gain Antenna(HGA)	*4.9*	*20%*	*5.8*
UHF-Quadrafilar Helix (Reconfigurable)	*1.5*	*20%*	*1.8*
SDST X-up/X down	*5.8*	*15%*	*6.7*
Electra (w/ X-band)	*11.3*	*30%*	*14.7*
X-band SSPA, RF=17W	*4.0*	*15%*	*4.6*
Coax Transfer Switch (CXS)	*0.2*	*30%*	*0.3*
X-band Diplexer, high isolation	*1.3*	*20%*	*1.6*
Filter, low power	*0.2*	*10%*	*0.2*
Hybrid Coupler	*0.0*	*30%*	*0.1*
X-band Rotary Joint	*0.3*	*30%*	*0.4*
Waveguide Transfer Switch (WGTS)	*1.1*	*30%*	*1.5*
WR-112 WG, rigid (Al)	*0.8*	*35%*	*1.1*
Thermal	27.7	29%	35.6
Multilayer Insulation	*11.7*	*30%*	*15.2*
Thermal Surfaces	*1.6*	*30%*	*2.0*
Thermal Conduction Control	*3.0*	*30%*	*3.9*
Heaters/Thermostats	*5.8*	*26%*	*7.3*
Temp Sensors	*0.6*	*10%*	*0.7*
Venus Shade	*5.0*	*30%*	*6.5*
Cabling Harness	38.0	30%	49.4
Launch Vehicle Adapter	0.0	30%	0.0
ERV Total (kg)	**678.5**	**28%**	**870.3**
System Contingency		2%	11.7
ERV Dry Total with Contingency (kg)			882
Propellant + Pressurant			2120
ERV Total Wet Mass (kg)			**3002**

Table 23: APPENDIX A - Master Equipment List - Propulsion Module

	Mass, CBE (kg)	Contingency	CBE + Contingency (kg)
Propulsion Stage	672.1	25%	837.0
Attitude Control	0.0		0.0
Command & Data Handling	0.0		0.0
Power	0.0		0.0
Propulsion	221.8	26%	280.2
Gas Service Valve	*0.9*	*2%*	*0.9*
HP Latch Valve	*0.7*	*2%*	*0.7*
Solenoid Valve	*1.4*	*0%*	*1.4*
HP Transducer	*0.5*	*2%*	*0.6*
Gas Filter	*0.2*	*2%*	*0.2*
NC Pyro Valve	*0.2*	*2%*	*0.2*
Temp. Sensor	*0.0*	*2%*	*0.0*
Liq. Service Valve	*0.6*	*2%*	*0.6*
Test Service Valve	*0.5*	*2%*	*0.5*
LP Transducer	*2.2*	*2%*	*2.2*
Liq. Filter	*0.8*	*2%*	*0.8*
LP Latch Valve	*1.4*	*2%*	*1.4*
NC Pyro Valve	*1.0*	*2%*	*1.0*
Mass Flow Control	*0.1*	*2%*	*0.1*
Temp. Sensor	*0.2*	*2%*	*0.2*
Lines, Fittings, Misc.	*2.5*	*0%*	*2.5*
DM Monoprop Thrusters 1	*1.6*	*2%*	*1.7*
DM Monoprop Thrusters 2	*2.7*	*10%*	*3.0*
Biprop Main Engine	*17.3*	*10%*	*19.0*
Ox Pressurant Tank	*28.6*	*30%*	*37.2*
Fuel Pressurant Tank	*56.9*	*30%*	*74.0*
Fuel Tanks	*59.9*	*30%*	*77.9*
Oxidizer Tanks	*41.6*	*30%*	*54.1*
Structures & Mechanisms	405.9	30%	527.7
Primary Structure	*169.2*	*30%*	*219.9*
Secondary Structure	*19.3*	*30%*	*25.1*
Aeroshell Ring Separation Plane/Devices	*16.8*	*30%*	*21.8*
Midplane to Aeroshell Plane Truss	*168.0*	*30%*	*218.4*
Mid Separation Plane / Devices	*15.8*	*30%*	*20.5*
Integration Hardware & MHSE	*11.3*	*30%*	*14.7*
Balance Mass	*5.6*	*30%*	*7.3*
Telecon			0.0
Thermal	22.6	29%	29.1
Multilayer Insulation	*14.9*	*30%*	*19.4*
Thermal Surfaces	*1.3*	*30%*	*1.7*
Thermal Conduction Control	*3.4*	*30%*	*4.4*
Heaters/Thermostats	*2.1*	*26%*	*2.6*
Temp Sensors	*0.8*	*10%*	*0.9*
Cabling Harness	21.7	30%	28.2
Launch Vehicle Adapter	0.0	30%	0.0
Propulsion Stage Total (kg)	**672.1**	**29%**	**865.2**
System Contingency		1%	8.5
Prop Stage Dry Total w/Contingency (kg)			**873.7**
Propellant + Pressurant			2950.0
Propulsion Stage Total Wet Mass (kg)			**3823.7**

Table 24: APPENDIX A - Master Equipment List – Mid-Truss Stage

	Mass, CBE (kg)	Contingency	CBE + Contingency (kg)
Truss Stage Total	200.6	30%	260.7
Attitude Control	0.0	10%	0.0
Command & Data Handling	0.0	30%	0.0
Power	0.0	30%	0.0
Propulsion	0.0	2%	0.0
Structures & Mechanisms	200.6	30%	260.7
Primary Structure	*0.0*	*19%*	*0.0*
Secondary Structure	*0.0*	*26%*	*0.0*
Mid Separation Plane	*15.8*	*30%*	*20.5*
Cruise to Mid Plane Truss	*168.0*	*30%*	*218.4*
Cruise Separation Plane	*16.8*	*30%*	*21.8*
Integration Hardware & MHSE	*0.0*	*30%*	*0.0*
Balance Mass	*0.0*	*30%*	*0.0*
Telecon	0.0	20%	0.0
Thermal	0.0	30%	0.0
Cabling Harness	0.0	30%	0.0
Launch Vehicle Adapter	0.0	30%	0.0
Mid-Truss Total (kg)	**200.6**	**30%**	**260.7**
System Contingency		0%	0.0
Mid-Truss Dry Total with Contingency (kg)			**261**
Propellant + Pressurant			0
Mid-Truss Total Wet Mass (kg)			**261**

Table 25: APPENDIX A - Master Equipment List - Aeroshell Stage

	Mass, CBE (kg)	% Contingency	CBE + Contingency (kg)
Aeroshell Stage Total	917.2	36%	1246.9
Forebody Primary Structure	*210.0*	*30%*	*273.0*
Forebody Secondary Structure	*14.7*	*30%*	*19.1*
Forebody TPS	*292.3*	*44%*	*420.0*
Forebody TCS/harness	*15.8*	*30%*	*20.5*
Backshell Primary Structure	*155.3*	*30%*	*201.9*
Backshell Secondary Structure	*10.9*	*30%*	*14.2*
Backshell TPS	*145.8*	*40%*	*204.1*
Backshell Separation Devices	*18.0*	*30%*	*23.4*
Backshell TCS/Harness	*14.5*	*30%*	*18.9*
Aeroshell Ring Separation Plane/Devices	*25.2*	*30%*	*32.8*
Payload Ring	*14.7*	*30%*	*19.1*
Aeroshell Stage Total (kg)	**917.2**	**36%**	**1246.9**
System Contingency		0%	0.0
Aeroshell Stage Total with Contingency (kg)			**1246.9**
Propellant + Pressurant			0.0
Aeroshell Stage Total Wet Mass (kg)			**1246.9**

Table 26: APPENDIX A - Master Equipment List - Cruise Stage

	Mass, CBE (kg)	% Contingency	CBE + Contingency (kg)
Cruise Stage Total	386.2	21%	466.0
Attitude Control	5.0	10%	5.5
Sun Sensors	*0.0*	*10%*	*0.0*
Star Trackers	*5.0*	*10%*	*5.5*
Command & Data Handling	0.0	30%	0.0
Power	16.3	30%	21.2
Solar Array	*13.9*	*30%*	*18.1*
Array Switching Boards	*0.8*	*30%*	*1.0*
Converters* Boards	*0.8*	*30%*	*1.0*
Diodes Boards	*0.8*	*30%*	*1.0*
Propulsion	25.8	23%	31.6
Gas Service Valve	*0.5*	*2%*	*0.5*
HP Latch Valve	*1.1*	*2%*	*1.1*
HP Transducer	*0.3*	*2%*	*0.3*
Gas Filter	*0.1*	*2%*	*0.1*
NC Pyro Valve	*0.1*	*2%*	*0.1*
NO Pyro Valve	*0.1*	*2%*	*0.1*
Temp. Sensor	*0.0*	*5%*	*0.0*
Liq. Service Valve	*0.3*	*2%*	*0.3*
Test Service Valve	*0.0*	*2%*	*0.0*
LP Transducer	*0.5*	*2%*	*0.6*
Liq. Filter	*0.4*	*2%*	*0.4*
LP Latch Valve	*0.7*	*2%*	*0.7*
Temp. Sensor	*0.1*	*2%*	*0.1*
Lines, Fittings, Misc.	*1.8*	*50%*	*2.7*
DM Monoprop Thrusters 1	*3.3*	*10%*	*3.6*
DM Monoprop Thrusters 2	*1.4*	*0%*	*1.4*
Fuel Pressurant Tank	*1.0*	*30%*	*1.3*
Fuel Tanks	*14.1*	*30%*	*18.4*
Structures & Mechanisms	290.2	27%	369.8
Primary Structure	*62.7*	*19%*	*74.6*
Secondary Structure	*15.4*	*26%*	*19.4*
Solar Array Structure	*16.1*	*30%*	*20.9*
Cruise Stage Adapter	*168.0*	*30%*	*218.4*
Cruise Separation Plane/ Devices	*25.2*	*30%*	*32.8*
Integration Hardware & MHSE	*2.8*	*30%*	*3.6*
Balance Mass	*0.0*	*30%*	*0.0*
Telecon	2.0	23%	2.5
X- Medium Gain Antenna (19dBi) MER	*1.6*	*25%*	*2.0*
Polarizer	*0.3*	*20%*	*0.4*
WR-28 EG, rigid	*0.1*	*0%*	*0.1*
Thermal	27.4	29%	35.4
Multilayer Insulation	*21.3*	*30%*	*27.7*
Thermal Surfaces	*0.7*	*30%*	*1.0*
Thermal Conduction Control	*2.1*	*30%*	*2.7*
Heaters/Thermostats	*2.7*	*26%*	*3.4*
Temp Sensors	*0.6*	*10%*	*0.7*
Cabling Harness	11.4	30%	14.8
Launch Vehicle Adapter	8.1	30%	10.5
Cruise Stage Total (kg)	**386.2**	**27%**	**491.3**
System Contingency		3%	10.8

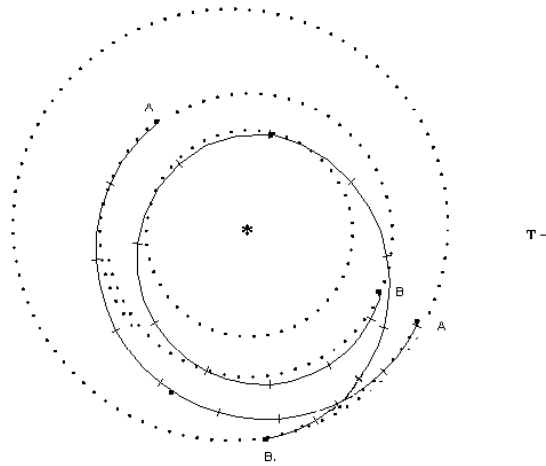|	Mass, CBE (kg)	% Contingency	CBE + Contingency (kg)
Cruise Stage Dry Total with Contingency (kg)			**502**
Propellant + Pressurant			260
Cruise Stage Total Wet Mass (kg)			**762**

Figure 46: APPENDIX B – Minimum energy Mars departure for 2016, 2018, 2021, 2022, 2024 (B) occurs before the spacecraft will arrive, and thus disallows the "fast" option from occurring.

Minimum energy type II outbound trajectory represented by (A). Minimum Mars departure energy (B) occurs before the spacecraft arrives, disallowing the "fast-return" option. Even if a type I transfer were used for the outbound leg, the Mars low energy departure occurs too late, with C_3's in excess of 100 km^2/s^2 needed to meet the stay time requirements. This is the basis for not selecting entries 3,5,8,10, and 12 in Table 5.
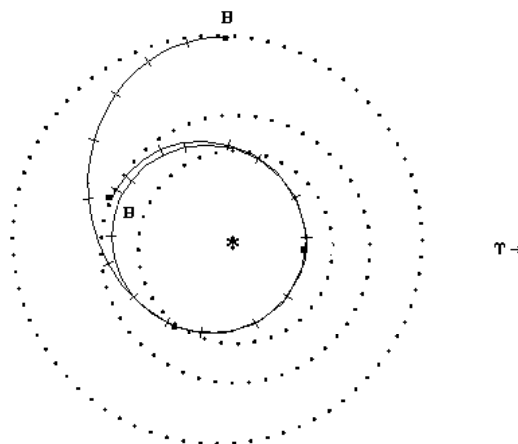

Figure 47: APPENDIX B – Alternative trajectory – fails due to excessive trip to Mars for 2015, 2017, 2019, 2020, 2021, 2023, and 2025 opportunities.

This figure does not include an outbound trajectory, as the return leg itself is responsible for the failure

in this alternative. Through the phasing that is available, this is the other form of Mars-Venus-Earth trajectory that presents itself, requiring an additional revolution about the sun before returning to Earth. The flight times typically exceed 600 days and therefore are not viable for the "fast-return" mission architecture. This is the basis for not selection entries 2,4,6,7,9,11, and 13 from Table 5.

Figure 48 — APPENDIX C - Mass/Maneuver Calculation Table for "Fast" Aerocapture Mars Sample Return Mission

Table 1 — From MEL / Calculated

Flight Element	Wet Mass (kg)	Inert Mass (Dry Mass + Residuals) (kg)	Usable Propellant (kg)	Prop Mass Fraction (reference)	Propellant Used (kg)	Error %	Prop Mass Fraction (calculated)
Cruise Stage	762	502.0	260.0	0.34	260	-0.1%	0.34
Aerocapture Stage	1246.9	1246.9	0.0	0.00	0	0.0%	0.00
Mid-Truss Stage	260.7	260.7	0.0	0.00	0	0.0%	0.00
ERV Sample Capture Jettisoned Hardware		79.3	0.0	0.00	0	0.0%	0.00
Propulsion Stage	3823.7	958.8	2864.9	0.75	2838	-0.9%	0.75
ERV (Bus + Retained Sample Capture)	2866.8	808.1	2058.7	0.72	2044	-0.7%	0.72
Earth Entry Vehicle (EEV)		55.9	0.0	0.00	0	0.0%	0.00
OS,A (Orbiting Sample Container Lander A)		4.1					
OS,B (Orbiting Sample Container Lander B)		4.1					
Sample A		0.5					
Sample B		0.5					

Legend: outputs indicated in Green; inputs indicated in Yellow; reference only values in Blue

Table 2 — Maneuver / Mass Calculation by Phase

Phase	LV Separation	TCMs in Cruise, ERV (OMS)	TCMs in Cruise, ERV (RCS)	Aerocapture (RCS)	Circularize, Clean up, and Rendezvous w/OS	Grab OS, Lander A OR B	Jettison Capture Hardware	Apocenter Raise	Apocenter Raise	Lower Pericenter	Attitude Control	Trans-Earth Injection + Cleanup	Deep Space Maneuver	Earth Entry Targeting	Attitude Control	EEV Separation	Deflection Maneuver
Delta-V (m/s)	--	60	--	--	420	--	--	664	635.4	10	--	2527.1	1200	30	--	--	30
Effective Isp (sec)	--	210	210	210	325	--	--	325.0	325.0	325.0	210.0	325	325	325	210	--	325
Element Performing Maneuver	--	Cruise Stage	Cruise Stage	Prop Stage	Prop Stage	ERV	ERV	Prop Stage	Prop Stage	Prop Stage	Prop Stage	ERV	ERV	ERV	ERV	ERV	ERV
Overall Maneuver Payload Mass Fraction	--	0.97	--	--	0.88	--	--	0.81	0.82	1.00	--	0.45	0.69	0.99	--	--	0.99
Element Mass (kg)																	
LV Upper Stage	762																
Cruise Stage	1247	502	502	1247													
Aerocapture Stage	261	1247	1247	261													
Mid-Truss Stage	79	261	261	79													
ERV Sample Capture Jettisoned Hardware	3797	79	79	3792	79	79											
Propulsion Stage	2852	3797	3797	2852	2955	2955	2955	1852	991	979	959	1258	844	836	816	816	808
ERV (Bus + Retained Sample Capture)	56	2852	2852	56	2852	2852	2852	2852	2852	2852	2852	56	56	56	56		
Earth Entry Vehicle (EEV)		56	56		56	56	56	56	56	56	56	4.1	4.1	4.1	4.1		
OS (Orbiting Sample Container A OR B)						4.1	4.1	4.1	4.1	4.1	4.1	0.5	0.5	0.5	0.5		
Sample (A or B)						0.5	0.5	0.5	0.5	0.5	0.5						
Total Post-Maneuver Mass	9053	8793	8793	8286	5942	5946	5867	4764	3903	3891	3871	1318	905	896	876	816	808
Propellant Used in Maneuver	259.9	0.0	0.0	5.0	836.6	0.0	0.0	1103.1	860.8	12.2	20.0	1594.0	413.5	8.5	20.0	0.0	7.6

Figure 48: APPENDIX C - Mass/Maneuver Calculation Table for "Fast" Aerocapture Mars Sample Return Mission

Notes: This table calculates propellant requirements based on the payload rather than mass capability based on the propellant. The launch vehicle separation mass calculated here is slightly lower than the launch vehicle separation mass shown in section 12.0. The difference in mass is excess propellant that is not needed to carry out the baseline mission, and therefore represents some additional margin in the overall vehicle capability. Calculation assumes 3% propellant residuals in the propulsion and ERV stages.

Input Values / Calculated Values

Flight Element	Primary Isp (sec)	Secondary Isp (sec)	Dry Mass (kg)	Residual Prop Mass (%)	Inert Mass (kg)	Wet Mass (kg)	Useable Prop Mass (kg)	Prop Mass Fraction
Cruise Stage	210	210	502.0	0.0%	502.0	1382.5	880.4	0.64
MoI Propulsion Stage	325	210	2842.6	3.0%	3411.1	22361.7	18950.6	0.85
ERV Sample Capture Jettisoned Hardware			79.3		79.3	79.3		
Propulsion Stage	325	210	958.8	3.0%	1045.7	3940.9	2895.2	0.73
ERV	325	210	808.1	3.0%	808.1	808.1	0.0	0.00
Earth Entry Vehicle (EEV)			55.9		55.9	55.9		
OS			4.1		4.1	4.1		
Sample			0.5		0.5	0.5		

Mass/Maneuver Calculation — by Mission Phase (transposed)

Mission Phase	Maneuver Type	Element Performing Maneuver	Delta-V (m/s)	Isp Type	Isp (sec)	Total Post-Mnvr Mass	Propellant used in Mnvr	Total Pre-Mnvr Mass
LV Separation	--		--			30671.9		
TCMs in Cruise, ERV (OMS)	Delta V	Cruise Stage		Primary	210	29791.5	880.4	30671.9
TCMs in Cruise, ERV (RCS)	RCS	Cruise Stage				29791.5	0.0	29791.5
Mars Orbit Injection (MOI)	RCS	MOI Propulsion Stage	3320	Primary	325	10338.8	18950.6	29289.4
Circularize, Clean up, and Rendezvous w/OS	Delta V	Propulsion Stage	420	Primary	325	6072.6	855.1	6927.7
Grab OS, Lander A OR B	Add Element					6077.2		6072.6
Jettison Before Return	Jettison Element					5997.9		6077.2
Apocenter Raise	Delta V	Propulsion Stage	664	Primary	325	4870.3	1127.7	5997.9
Apocenter Raise	Delta V	Propulsion Stage	635.4	Primary	325	3990.2	880.0	4870.3
Lower Pericenter	Delta V	Propulsion Stage	10	Primary	325	3977.8	12.5	3990.2
Attitude Control	RCS	Propulsion Stage				3957.8	20.0	3977.8
Trans-Earth Injection + Cleanup	Delta V	ERV (Bus + Retained Sample Capture)	2527.1	Primary	325	1318.2	1593.9	2912.1
Deep Space Maneuver	Delta V	ERV (Bus + Retained Sample Capture)	1200	Primary	325	904.7	413.5	1318.2
Earth Entry Targeting	Delta V	ERV (Bus + Retained Sample Capture)	30	Primary	325	896.2	8.5	904.7
Attitude Control	RCS	ERV (Bus + Retained Sample Capture)				876.2	20.0	896.2
EEV Separation	Jettison Element					0.0		815.7
Deflection Maneuver	Delta V	ERV (Bus + Retained Sample Capture)	30	Primary	325	808.1	8	816

Element Mass (kg) rows used in calculation: Cruise Stage, MoI Propulsion Stage, ERV Sample Capture Jettisoned Hardware, Propulsion Stage, ERV (Bus + Retained Sample Capture), Earth Entry Vehicle (EEV), OS, Sample.

Notes: This table calculates propellant requirements based on the payload rather than mass. The Mars orbit injection burn is carried out by a single propulsive stage with a stage massfraction of 0.15. Calculation assumes 3% propellant residuals in the MOI propulsion, propulsion and ERV stages.

Figure 49: APPENDIX C - Mass/Maneuver Calculation Table for "Fast" All-Propulsive (Chemical Propulsion Only) Mars Sample Return Mission
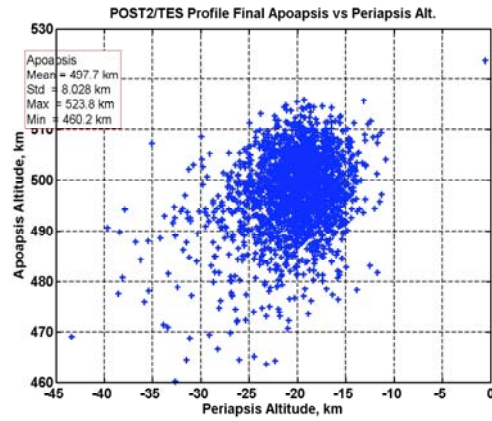
Figure 50: APPENDIX D - Apoapsis Altitude vs. Periapsis Altitude – Using TES profile vs normal MarsGRAM Profile
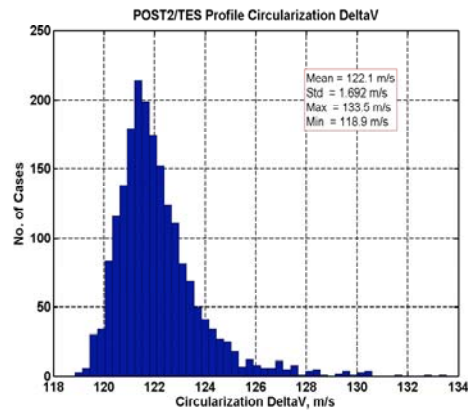

Figure 51: APPENDIX D - Circularization Delta-V – Using TES profile vs normal MarsGRAM Profile
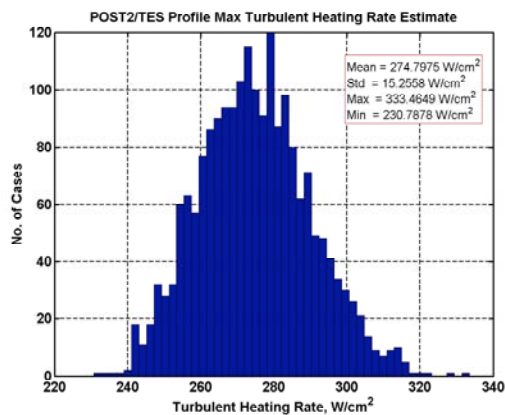

Figure 52: APPENDIX D - Maximum LAURA Turbulent Heating Rate Estimate – Using TES profile vs normal MarsGRAM Profile
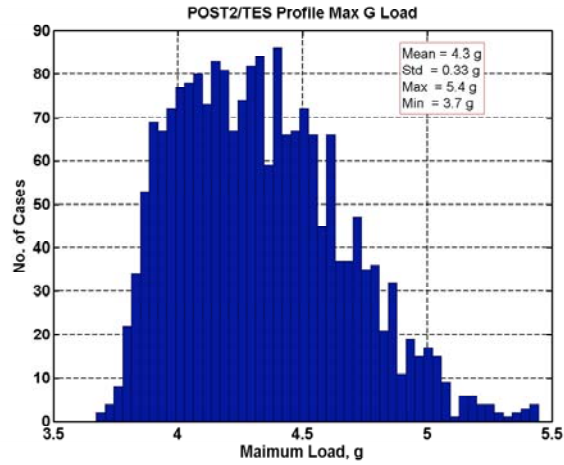
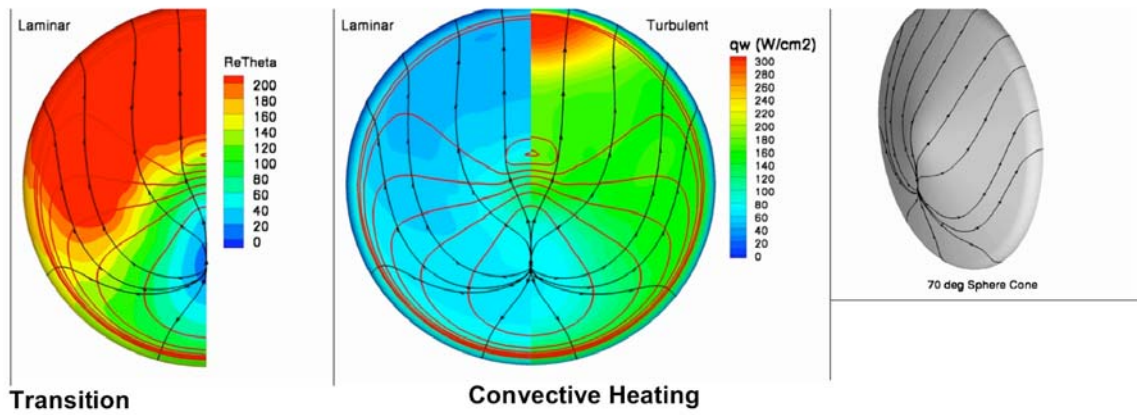**Figure 53: APPENDIX D - Maximum G-Loading - Using TES profile vs normal MarsGRAM Profile**

.

Figure 54: APPENDIX E - Convective heating results for 70° sphere cone heatshield; with uncertainties, DPLR.

(4.65 m dia, angle of attack=16°, L/D=0.24, peak heating trajectory point.)
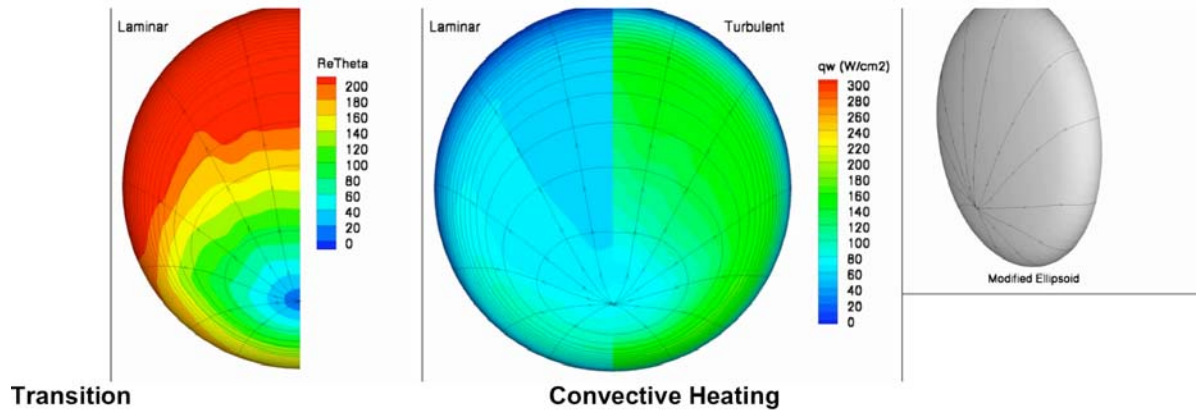
Figure 55: APPENDIX E - Convective Heating results for Ellipsoidal Heatshield

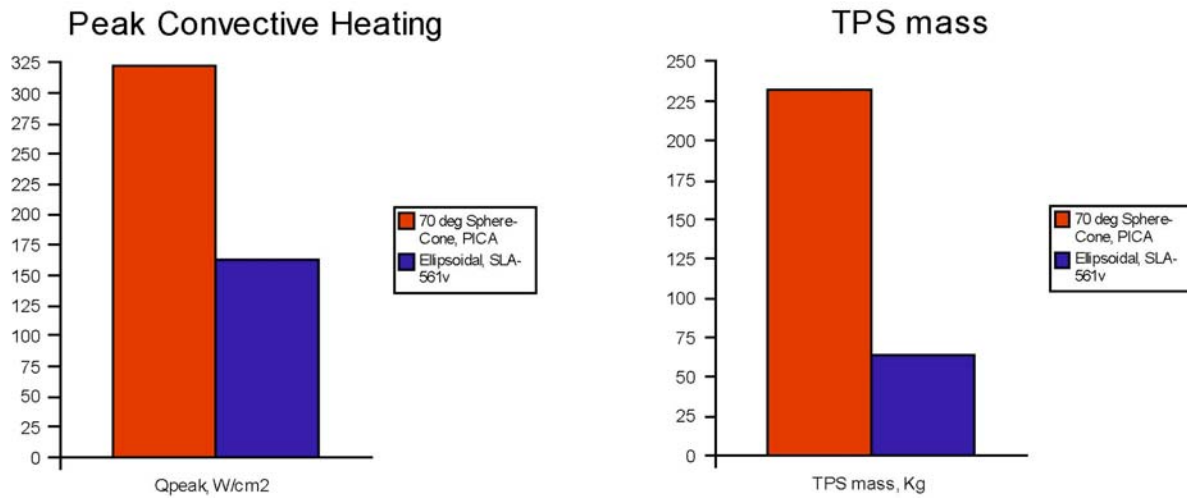(4.65 m dia, angle of attack=16°, L/D=0.24, peak heating trajectory point.)

Figure 56: APPENDIX E – TPS Sizing for Ellipsoidal Heatshield vs 70° Sphere Cone Heatshield, unmargined mass

REPORT DOCUMENTATION PAGE

Form Approved
OMB No. 0704-0188

1. REPORT DATE *(DD-MM-YYYY)*	2. REPORT TYPE	3. DATES COVERED *(From - To)*
01- 11 - 2006	Technical Memorandum	

4. TITLE AND SUBTITLE

Mars Aerocapture Systems Study

5a. CONTRACT NUMBER

5b. GRANT NUMBER

5c. PROGRAM ELEMENT NUMBER

6. AUTHOR(S)

Wright, Henry S.; Oh, David Y.; Westhelle, Carlos H.; Fisher, Jody L.; Dyke, R. Eric; Edquist, Karl T.; Brown, James L.; Justh, Hilary L.; and Munk, Michelle M.

5d. PROJECT NUMBER

5e. TASK NUMBER

5f. WORK UNIT NUMBER

346620.02.01.04.07.01

7. PERFORMING ORGANIZATION NAME(S) AND ADDRESS(ES)

NASA Langley Research Center
Hampton, VA 23681-2199

8. PERFORMING ORGANIZATION REPORT NUMBER

L-19290

9. SPONSORING/MONITORING AGENCY NAME(S) AND ADDRESS(ES)

National Aeronautics and Space Administration
Washington, DC 20546-0001

10. SPONSOR/MONITOR'S ACRONYM(S)

NASA

11. SPONSOR/MONITOR'S REPORT NUMBER(S)

NASA/TM-2006-214522

12. DISTRIBUTION/AVAILABILITY STATEMENT

Unclassified - Unlimited
Subject Category 18
Availability: NASA CASI (301) 621-0390

13. SUPPLEMENTARY NOTES

An electronic version can be found at http://ntrs.nasa.gov

14. ABSTRACT

Mars Aerocapture Systems Study (MASS) is a detailed study of the application of aerocapture to a large Mars robotic orbiter to assess and identify key technology gaps. This study addressed use of an Opposition class return segment for use in the Mars Sample Return architecture. Study addressed mission architecture issues as well as system design. Key trade studies focused on design of aerocapture aeroshell, spacecraft design and packaging, guidance, navigation and control with simulation, computational fluid dynamics, and thermal protection system sizing. Detailed master equipment lists are included as well as a cursory cost assessment.

15. SUBJECT TERMS

HYPAS; MSR; Mars; Aerocapture; Opposition; Orbiter; Sample

16. SECURITY CLASSIFICATION OF:			17. LIMITATION OF ABSTRACT	18. NUMBER OF PAGES	19a. NAME OF RESPONSIBLE PERSON
a. REPORT	b. ABSTRACT	c. THIS PAGE			STI Help Desk (email: help@sti.nasa.gov)
U	U	U	UU	87	19b. TELEPHONE NUMBER *(Include area code)* (301) 621-0390

Standard Form 298 (Rev. 8-98)
Prescribed by ANSI Std. Z39.18